FLORIDA STATE UNIVERSITY

COLLEGE OF ENGINEERING

PERFORMANCE LIMITS OF POWDER IN TUBE PROCESSED NB_3SN SUPERCONDUCTING WIRES

By

CHRISTOPHER B. SEGAL

A Dissertation submitted to the
Department of Mechanical Engineering
in partial fulfillment of the
requirements for the degree of
Doctor of Philosophy

2018

Christopher B. Segal defended this dissertation on April 16th, 2018.
The members of the supervisory committee were:

David C. Larbalestier
Professor Directing Thesis

Jennifer Proffitt
University Representative

Fumitake Kametani
Committee Member

Emmanuel Collins
Committee Member

Chiara Tarantini
Committee Member

Peter J. Lee
Committee Member

The Graduate School has verified and approved the above-named committee members, and certifies that the dissertation has been approved in accordance with university requirements.

This dissertation is dedicated to my father and his father for always believing in me

and to my wife Anna, a never ending source of love and support

ACKNOWLEDGMENTS

To say that completing this PhD was accomplished alone would be insincere, and far from the truth. It takes many people, both personally and professionally, to enable an environment in which a person can truly succeed. I was fortunate to have many incredible people intersect my life during the years I was at the ASC, and it would be difficult to convey the depth of impact each person has had on my life.

I am first forever indebted to my mentor and supervising professor David Larbalestier. When I was a fledgling scientist, unsure of what my future could hold, he offered me an opportunity and a chance of a lifetime to work at the Applied Superconductivity Center and pursue a PhD in mechanical engineering. More than that, in times of personal need David and other members of the ASC were always there to help in any way possible, and for all of this I am forever grateful.

I am secondly indebted to master image-analyzer Peter Lee, for whom this thesis owes part of its life. Without his wizardry and dedication to expanding FIJI with scientific tools for the entire superconductivity community, it's unclear if this dissertation would have been possible; or at most it would have been a shell of what is presented here.

Additionally, many of the novel experiments in this thesis would not have been possible without the regular discussions with Chiara Tarantini. Her attention to detail was also greatly appreciated in the writing and editing of this dissertation.

Working alongside the other graduate assistants at the ASC has been a great privilege during these past years, and I'm not sure that I would have gotten to the end without the friendship and guidance from every last one of you. During our time working together, and meeting so many incredible people, I discovered one thing... any one of you could have done this work. That is to say, it is not just about being "smart", it is about being tenacious. It is about asking the right questions and not relenting until you find an answer that satisfies your curiosity. If you want it bad enough, and try for long enough, you might just surprise yourself. If you let this curiosity drive your actions, I think success will always follow.

And of course, none of our work would be possible without the wonderful support staff at the ASC. Bob Goddard always working tirelessly to keep our SEM drift as low as possible. Bill Starch always keeping our polishing room fully stocked, and our furnaces always warm. At the same

time, Van Griffin was doing quite the opposite and keeping all of our magnets cold and ready for measurement at all hours of the day (and many thanks to Ashleigh Francis and Griffin Bradford for making many of those measurements). I am also certain my time would not have been as enjoyable without the always smiling faces of Connie Linville and Charlotte Hall, as well as our building custodian Deborah Ruffin (Miss Debbie), who was a constant source of unique perspective on any problem, life or otherwise.

Beyond the ASC, I was fortunate to have many great collaborators abroad. The fruitful discussions at CERN with Amalia Ballarino, Bernardo Bordini, Christian Scheuerlein, and Luca Bottura were invaluable, as were the conversations with the team at Bruker - Klaus Schlenga, Manfred Thöner, Bernd Sailer, and Matheus Wanior.

All of this work was only made possible by various funding sources over the course of my PhD. This work was supported by the US Department of Energy (DOE) Office of High Energy Physics under award numbers DE-FG02-07ER41451 and DE-SC0012083, and by CERN under grants KE1920/TE, RF02226, and KN2713. A portion of this work was performed at the National High Magnetic Field Laboratory, which is supported by the National Science Foundation Cooperative Agreement No. DMR-1157490 (-2017) DMR-1644779 (2018-) and the State of Florida. The 0.78 mm PIT wire was supplied to us by the US LHC Accelerator Research Program (LARP), which is a BNL, FNAL, LBNL, and SLAC collaboration with CERN for the High Luminosity LHC program: http://www.uslarp.org/

Outside the field of superconductivity, I found solidarity in the United Faculty of Florida Graduate Assistants United (UFF-FSU-GAU). What started in 2012 as a general curiosity of how unions could help improve grad assistant working conditions, quickly turned into activism and I found myself protesting at the capitol that “enough is enough” in rather short order. This realization was only made possible by President Kerr Ballenger steering the ship of the GAU in an extremely easy to follow direction. Further up the ladder, I am deeply grateful to our Service Unit Director, Tom Wazlavek, for teaching me the ins and outs of collective bargaining, as well as UFF President Jennifer Proffitt and Executive Director Marshall Ogletree for mentoring me in how to effectively engage legislators and even get bills sponsored and to the floor of various legislative committees.

And at last, none of this would have been possible without my incredible wife Anna. We met not long after I started at the ASC, and I think we both knew quickly that marriage was closer for

us than graduation. In only a short time you brought so much love and compassion into my life that it is hard to remember what it was like before. I guess I called it 'living,' but it was nothing as rich as the life we have built together, and I can not wait for what comes next.

Many thanks to all!

Cheers,
Chris.

TABLE OF CONTENTS

LIST OF TABLES

LIST OF FIGURES

LIST OF SYMBOLS

T_c	Critical temperature
I_c	Critical current
J_c	Critical current density in superconducting filaments
$J_{c-layer}$	J_c in superconducting transport layer
B_c	Thermodynamic critical field
B_{c1}	Lower critical field
B_{c2}	Upper critical field
B_{irr}	Irreversibility field
B_k	Kramer extrapolated irreversibility field
RRR	Residual Resistance Ratio
F_p	Pinning force
d_{eff}	Area equivalent filament diameter

LIST OF ABBREVIATIONS

SG A15	Small Grain A15
LG A15	Large Grain A15
DB	Diffusion Barrier
HT	Heat Treatment
LHC	Large Hadron Collider
CERN	European Organization for Nuclear Research
ASC	Applied Superconductivity Center
LUT	Look Up Table
FESEM	Field Emission Scanning Electron Microscope
BSE	Back Scattered Electron(s)
EDS	Energy Dispersive X-ray Spectroscopy
SE2	Secondary Electron
HRT	Highest Reaction Temperature
LRT	Low-Temperature Reaction
IMHT	Inverted Multistage Heat Treatment
LARP	LHC Accelerator Research Program
LTS	Low Temperature Superconductor
HTS	High Temperature Superconductor

ABSTRACT

For 10-15 years, the Powder-In-Tube (PIT) process has been one of the leading manufacturing methods for producing the highest critical current density (J_c) Nb_3Sn wires for at small effective filament diameter (d_{eff}), both required for future applications in high energy physics. Since Nb_3Sn first became commercially available in the 1960's, non-Cu J_c values have steadily climbed until a plateau was reached at about 3,000 A/mm^2 (12 T, 4.2 K) in the year 2000. Comprehensive analysis of recent wires suggests that both PIT and the other high J_c wire design, Rod Restack Process (RRP), have yet to achieve their maximum potential as high J_c conductors. Currently, PIT wires obtain a maximum J_c(12 T, 4.2 K) of about 2700 A/mm^2 and do so by converting up to 60% of the non-Cu cross section into superconducting Nb_3Sn. However, about a quarter of this Nb_3Sn is made of large grains which are too large or otherwise disconnected to carry current in transport, wasting both real estate, as well as Sn and Nb that would be better used to make the desired small grain A15. The most recent RRP wires typically achieve J_c(12 T, 4.2 K) values of around 3000 A/mm^2 by also converting about 60% of the non-Cu cross section into A15, however nearly all of that has the desired small grain morphology with high vortex pinning, ideal for current transport.

Studies at the Applied Superconductivity Center have shown that one route to improvement for both wires may be in controlling the formation of intermediate phases which form before Nb_3Sn. An intermetallic Nb-Cu-Sn, commonly referred to as Nausite, is considered responsible for the formation of the undesirable large grains. We studied the phase evolution in PIT Nb_3Sn from the starting powder mixture at room temperature up to 690 °C to better understand what role Nausite ($(Nb_{0.75}Cu_{0.25})Sn_2$) actually plays in forming large grain A15 with the goal of preventing its formation and making better use of the Sn available to form the desired small grain A15 morphology. After heat treatment, all wires were imaged in an SEM and then processed through digital image analysis software, extracting area fractions of each phase and their morphology. For heat treatments which showed interesting metallographic results, additional measurements were made by transport, resistivity, magnetization, and/or heat capacity to develop a complete picture of how the microstructure affects critical wire properties. Based on these results, novel heat treatments were developed and demonstrated our ability to reduce the undesired large grain A15 while

simultaneously producing more current-carrying small grain A15, increasing the ratio of small:large grain A15 from 3.0 to 3.8.

Another possible path to improvement is to reduce the non-uniform deformation incurred during wire fabrication. A PIT Nb_3Sn wire begins as a mono-filament consisting of a thick Nb7.5wt%Ta tube clad in high-purity Cu, inscribed with a Cu sleeve, and filled with a Sn-rich $NbSn_2$ powder. The external Cu cladding will later provide a low resistance normal conducting path around superconducting filaments, a necessity for magnet stability. The final wire diameter is between 0.7-1.0 mm with 156 or 192 filaments, whose diameters are 33-50 μm, organized into 6-7 concentric rings. Through advanced digital image analysis software, we can extract geometric information which describes how the wire and filaments deform from their nominally circular shape, becoming elliptical or otherwise having non-uniform deformation which can be detrimental to wire properties. We found that the non-uniform deformation incurred during wire fabrication can degrade the wire performance. The most severe effect is caused by the different deformation rates of the Nb-Ta tube compared to its powder core, which leads to the Sn-rich core drifting from the center of its tube, leading to an uneven A15 reaction front. This is referred to here as 'centroid drift'.

In PIT wires, the diffusion barrier must be consumed to form A15 while still leaving a thin, protective annulus behind to protect the Cu. Centroid drift then causes a large inefficiency as it creates a thick and thin side of diffusion barrier, the thin side limiting the reaction if Sn leaks are to be prevented, while the thick side becomes wasted Nb-Ta. Up to 30% of the final non-Cu cross-section remains as unused diffusion barrier. When Sn leaks out of the filaments it increases the resistivity of the Cu stabilizer, lowering the Residual Resistance Ratio (RRR). A high RRR is required for magnet stability, and such Sn leaks can be detrimental to magnet performance. In addition, we found that filaments farther from the center of the wire tend to be those with highest centroid drift, and they are also the most susceptible to leaking Sn. Moreover, we observed that in leaks severe enough to produce a Kirkendall void, the A15 volume is also reduced. By comparison, RRP wires manage a similar reaction with <10% residual barrier in the non-Cu cross section.

Recently, Bruker EAS, the manufacturer of PIT Nb_3Sn wires, developed a new wire design which added a bundle barrier around the filament pack to contain Sn leaks and maintain a high RRR, as well as increasing the Sn content in the powder core to produce more A15. We believe that

by improving deformation properties and optimizing new heat treatments to account for the higher Sn content, J_c can be substantially enhanced while maintaining RRR at small filament diameters.

CHAPTER 1

INTRODUCTION

1.1 A brief history of superconductivity

In 2011 the field of superconductivity celebrated its 100th anniversary, the centennial discovery marked by Kamerling Onnes finding that pure mercury was superconducting, showing zero resistance at a critical temperature (T_c) of 4.2 K [1]. He discovered this by measuring the sample's resistance in liquid helium which Onnes had successfully liquified three years prior, at 1 bar, 4.2 K [2]. This first discovery in mercury was quickly followed by finding superconductivity in other metals, including lead at 7.2 K in 1913 [3, 4], and niobium at 9.2 K in 1930 [5].

In 1931, the first A15 structure was observed in a layer of tungsten oxide (W_3O) [6], however this A_3B crystal structure was not found to be superconducting until the discovery of the intermetallic A15 phase vanadium silicide (V_3Si) in 1953 which showed superconductivity at 17 K [7]. Nb_3Sn was immediately investigated and found to be superconducting at 18 K [8]. There are some interesting historical footnotes related to the discovery of niobium based superconductors. John Hulm and Bernd Matthias were studying solid solution alloys of transition metals that fit into the framework of electron to atom ratio rules established by Matthias in 1955 [9], which included NbTi and NbZr. However, at that time the work was being done at University of Chicago where their vacuum system was quite poor for this type of work, resulting in many nitrides and oxidized samples, obscuring the properties of the pure alloys they sought to study [10]. Hulm then moved to Westinghouse where he had excellent facilities for melting alloys and, with the help of Richard Blaugher, he measured the T_c for all of the nearest-neighbor BCC binary solid-solution alloys [11].

Many times in history science is moved forward by external factors, including politics, or in the case of John Hulm, by love of country. Blaugher recalled an interesting anecdote regarding the discovery of NbTi at a memorial session celebrating the life of John Hulm at the 2004 Applied Superconductivity Conference [11]:

"One day I was sitting at my desk at Westinghouse R&D and John Hulm literally burst into the lab. "Blaugher" he says, "I have been thinking." John started to sketch out on the blackboard

the periodic chart for groups four, five and six. "We have studied V-Nb, Nb-Ta, V-Cr, V-Mo, Nb-Cr, Nb-Mo, Nb-W, Nb-Hf, and Nb-Zr" (which he emphasized by drawing straight lines linking the various binaries). "We MUST do Nb-Ti!" Why I asked? John replied, because, "God save the Queen, we'll have the Union Jack." Needless to say with this overwhelming logic I proceeded to make up some samples to study this binary. Were it not for John's English background we would have omitted the most important binary for our study."

Hulm and Blaugher published this comprehensive study of the binary alloys of transition metals in September 1961 [12]. Though the last to be studied in their work, NbTi would become the workhouse for the entire superconductivity community, and still today it is the most widely used superconductor [13].

Through the 1950s and 60s, A15 compounds were still considered "high T_c" superconductors [7, 8] as their T_c was in the tens of Kelvin compared to single digit values measured for many pure elemental metals. This classification lasted for quite some time until 1986 when Bednorz and Müller discovered the first truly high T_c superconductor Ba-La-Cu-O with T_c near 30 K [14]. This was the first in a new class of conductors called "rare earth barium copper oxides" (ReBCO), and was quickly followed by the discoveries of yttrium barium copper oxide (YBCO, T_c=93 K) [15], and bismuth-based, high T_c conductors without any rare earth element [16, 17] having T_c onset as high as 105 K [18]. At this point, superconductors clearly fell into two categories, LTS (T_c $<$ ~20 K), and HTS which has $T_c > 80$ K. In 2008 iron-based superconductors were discovered, some having T_c as high as 100 K [19]. While not detailed in this work, HTS materials have yet to substantially penetrate the superconducting magnet market, but nevertheless march optimistically towards development into fully mature conductors [20, 21, 22, 23].

1.2 What is a superconductor?

A superconductor is a material which exhibits two characteristic properties when cooled below T_c: zero electrical resistance and perfect diamagnetism [24]. It is interesting to note that despite superconductivity being discovered in 1911, its perfect diamagnetism wasn't understood until 1933, when Meissner and Ochsenfeld discovered that ideal materials in the superconducting state expel any externally applied magnetic fields when cooled below T_c, now referred to as the Meissner effect. This means theoretically B=0 everywhere in the sample. In reality, a surface screening current is

established and both the current and B field decay exponentially from the surface over what's called the London penetration depth *(λ_L)*, with the bulk of the sample having B→0 [25].

Two types of superconductors exist, for type 1 superconductors there is a total flux expulsion at low fields but, when the applied field exceeds a critical field (B_c), the field is able to fully penetrate the superconductor and it enters the normal state. However, some superconductors will only partially exclude flux in a higher magnetic field, preventing perfect diamagnetism and creating a mixed state, these are called type 2 superconductors. Type 2 superconductors are perfectly diamagnetic below a critical field (B_{c1}), and when the external magnetic field exceeds B_{c1}, magnetic flux can penetrate in quantized units forming what are frequently referred to as *vortices*. Vortices consists of cores in the normal state, where B has a maxima, surrounded by superconducting regions with decaying field and circulating current. For higher applied fields, the vortices start overlapping, increasing the average field inside the superconductor. As the applied field increases, an upper critical field (B_{c2}) is reached and the material becomes normal everywhere. As shown in Figure 1.1, all critical fields are temperature dependent.

Type 2 superconductors can be further described as alloys and compounds which exhibit a mixed-state above B_{c1}. All superconductors which have a practical application are type 2. The magnetic behavior of type 2 superconductors described above is reversible but can only be seen in extremely clean and homogeneous materials, which are actually not useful for high field applications.

For example, consider applying a transport current to a type 2 superconducting slab in an applied magnetic field as shown in Figure 1.2. A force is exerted on each vortex by the interaction of its magnetic field with the transport current, causing them to move from one side of the slab to the other (-x to +x in this image). The movement of these vortices across the slab generates an electric field in the superconductor which has a component in the same direction as J, giving rise to ohmic losses. This dissipation can ultimately drive the material into the normal state. The onset of this ohmic behavior defines a new critical parameter, where at a given temperature and field, there exists a critical current density *(J_c)* that can be carried by the superconductor without dissipation. While this dissipation readily occurs in pure, homogeneous samples ($J_c = 0$), defects within a superconductor are able to pin the vortices and prevent flux flow, resulting in no voltage or resistance. This pinning force (F_p) is a short-range force that holds the core of a vortex in place at

interfaces such as grain boundaries, vacancies, dislocations, interstitial defects, secondary phases, etc. [24].

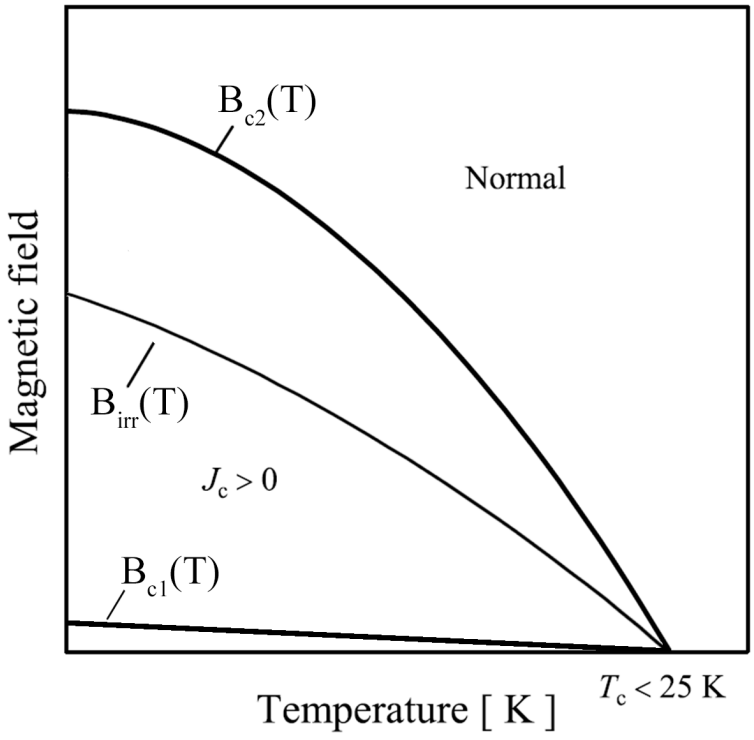

Figure 1.1: Magnetic phase diagram for type 2 LTS superconductors. Below B_{irr} the vortices are mostly pinned and $J_c>0$. Above B_{irr} many vortices become unpinned and can move reversibly but with dissipation, resulting in loss of current flow ($J_c=0$). Above B_{c2}, the applied field has fully penetrated the material, and it transitions into the normal state.

The result of increasing the pinning strength is that a higher J_c can flow in the superconductor. Thus, it is of high interest to study the most favorable distribution of pinning centers for a material. Since J_c is field dependent a new magnetic phase boundary called the irreversibility field (B_{irr}) can be identified. The phase below B_{irr} can be considered a flux solid, with vortices pinned and $J_c>0$. Above B_{irr}, many vortices become unpinned and can move reversibly but with dissipation as a flux liquid, resulting in loss of super current ($J_c=0$) as shown in Figure 1.1. Above B_{c2}, the applied field has fully penetrated the slab, and it transitions into the normal state.

Since the high field magnets needed to measure B_{irr} are not always available, it is commonly estimated by making measurements of J_c vs applied magnetic field in the 10-15 T range and extrap-

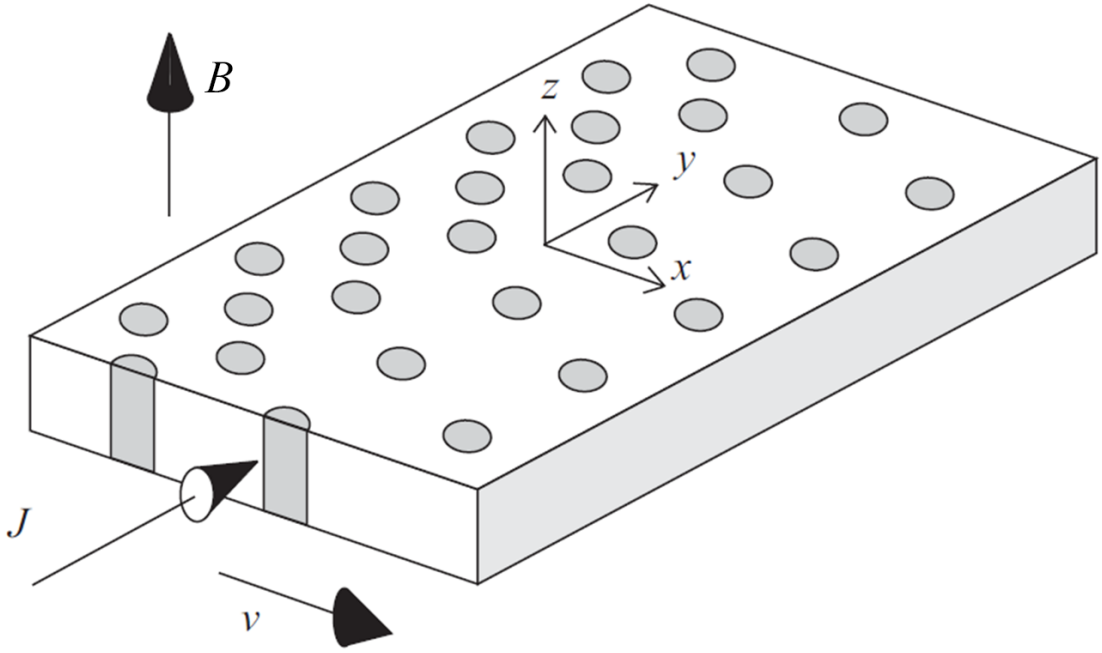

Figure 1.2: A slab of type two superconductor in an applied magnetic field carrying current (J) in transport. The gray cylinders represent vortices, and B is the applied magnetic field. The vector ν points in the direction of flux line movement. Reproduced from [26]

olating the field to when J_c=*0*. Perhaps the most common extrapolation comes from the Kramer universal scaling law [27], which has the form shown in Equation 1.1. B_{irr} is then approximated at the field where $B_K = 0$.

$$B_K = J_c^{0.5} * B^{0.25} \tag{1.1}$$

All three superconducting parameters, T_c, B_{irr}, and J_c vary with the superconducting material, and the fabrication processes. Since B_{irr} is temperature dependent and J_c is both temperature and field dependent, a "critical surface" that describes a superconductors performance limits can be drawn for each superconducting material (Figure 1.3). The left plot shows the two main low temperature superconductors (LTS), with Nb_3Sn substantially increasing the critical surface compared to NbTi. For example, B_{c2} increases from about 12 T in NbTi to 23-26 T in binary Nb_3Sn. On the right, the introduction of high temperature superconductors (HTS) further expands the sur-

face, most notably the field range has increased to an estimated 250 T in the case of $YBa_2Cu_3O_7$, potentially allowing the production of very high field magnets.

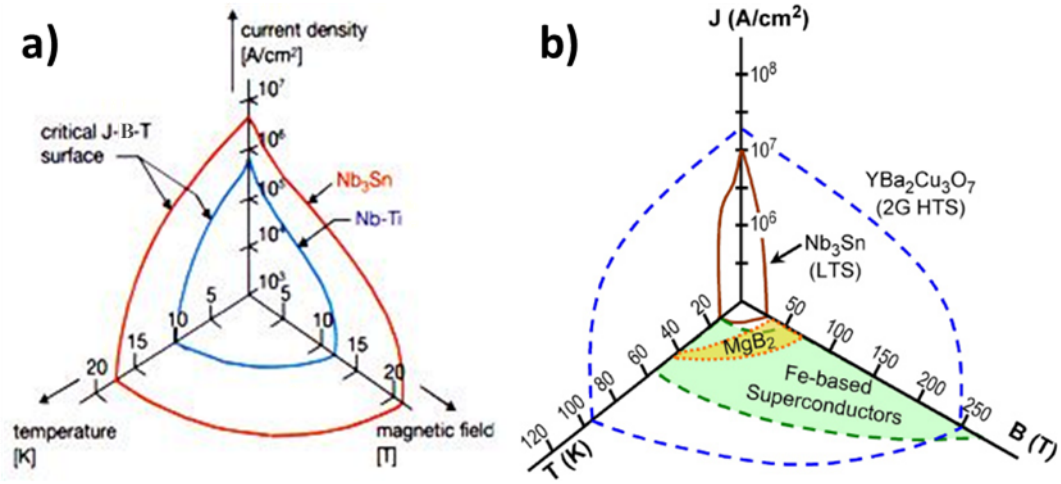

Figure 1.3: (a) The critical surface of both LTS conductors NbTi and Nb_3Sn reproduced from [28]. (b) With the addition of HTS conductors, the critical volume expands substantially [29].

The most useful way to compare materials and fabrication methods is to collapse the critical surface by setting the temperature at a constant 4.2 K, and then plot the critical current vs applied magnetic field as shown in Figure 1.4 ([30]). Here it becomes much more apparent which superconductors are suited for different applications. For example, in the low field regime below about 10 T NbTi is the most practical choice, whereas above this field Nb_3Sn becomes the next preferred choice in most cases. While the high J_c and weak field dependence of the HTS conductors look promising, they are still not mature enough to support the needs of the commercial magnet industry, and the LTS conductors NbTi and Nb_3Sn remain the primary choice for nearly all commercial superconducting magnets which have been made to date.

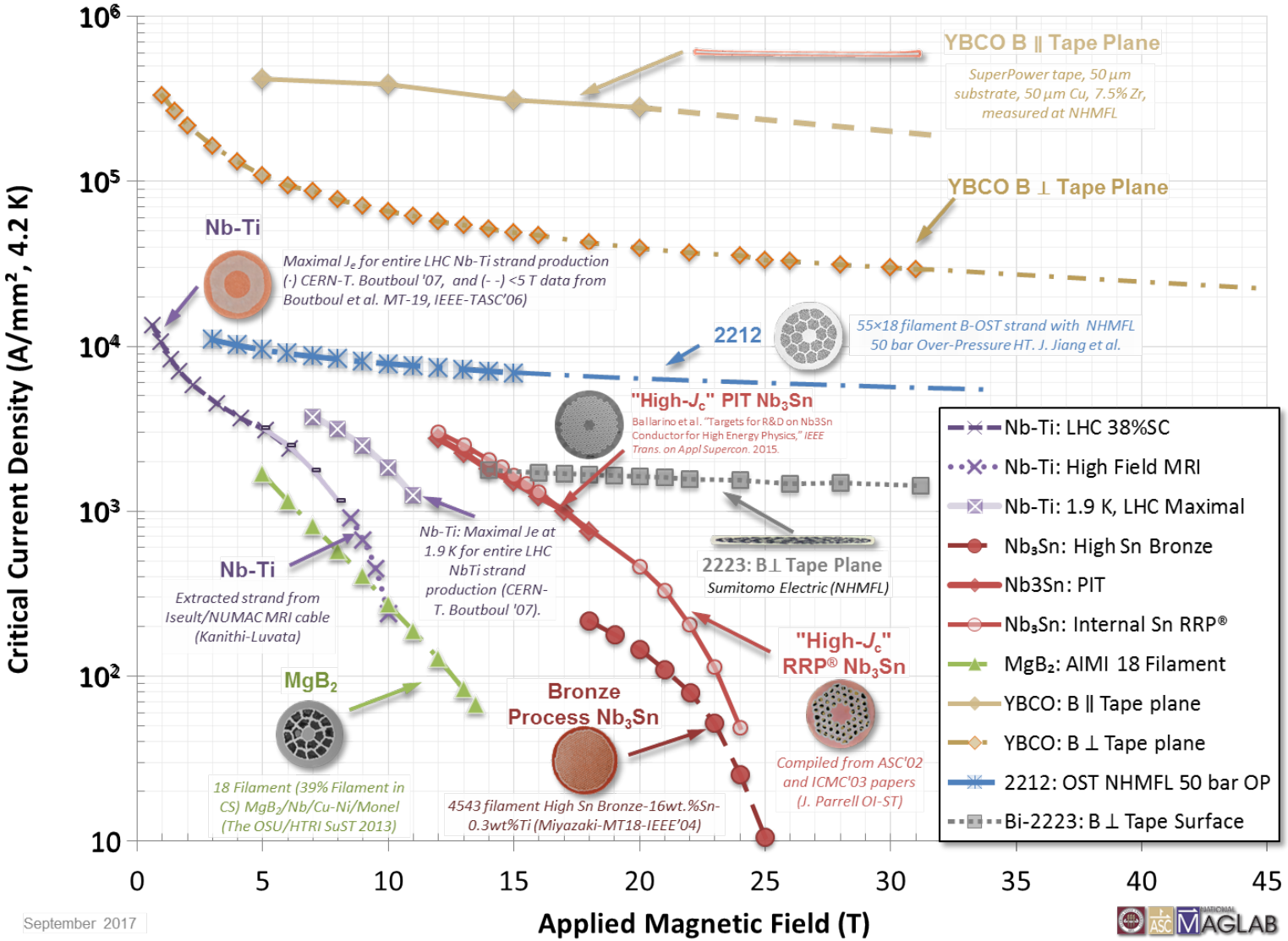

Figure 1.4: A semi-logarithmic plot showing various practical superconductors and the behavior of critical current density as a function of applied magnetic field at 4.2 K. LTS conductors tend to have a rapid drop off with field while HTS conductors have a weaker field dependence, allowing use at higher fields and higher operating currents.

1.3 What is Nb_3Sn?

Nb_3Sn is an intermetallic compound that has an A_3B (A15) phase structure, and its T_c is strongly dependent on Sn content which ranges from 18-27at%Sn (though wires typically have a maximum of 25at%Sn). This range of possible Sn content allows T_c to vary from 18.3 K [31] at stoichiometry (Nb25at%Sn) to a low value of about 6 K (Figure 1.5) [32]. This T_c distribution gives rise to a range of superconducting properties and causes both B_{c2} and J_c to vary. Additionally, the presence of dopants in the A15 phase can effect B_{c2}, with generally 1-2at%Ti and/or Ta increasing B_{c2} from about 26 T to 29 T [33].

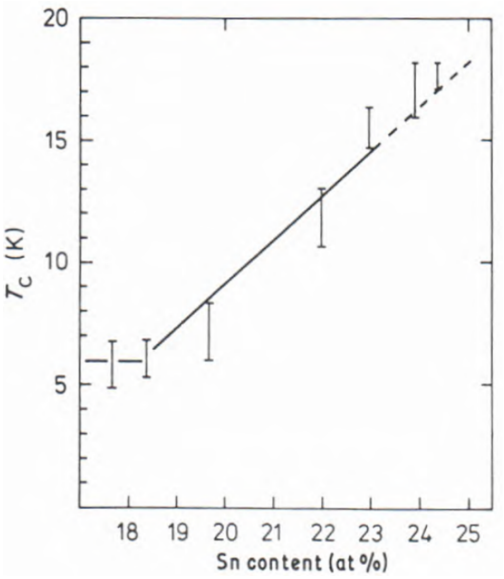

Figure 1.5: The T_c of Nb_3Sn has a strong dependence on Sn. The max T_c at stoichiometry is 18.3 K, while the lowest T_c is at 6 K. Image reproduced from [32]

1.3.1 How are Nb_3Sn wires fabricated?

All modern Nb_3Sn superconducting wires are multifilamentary and can be essentially separated into two components: the filaments containing materials to form the superconducting Nb_3Sn A15 phase, and the non-superconductor area, which is typically a pure Cu stabilizer in which the filaments are embedded, required for magnet stability. With this composite wire, it is common to define J_c as a non-Cu J_c, considering only the area of the filaments. In this dissertation J_c

will always calculated with respect to the unreacted filament area. The pure stabilizer Cu acts as an auxiliary pathway for current when a superconducting filament is locally compromised and cannot transport the full current. This Cu stabilizer matrix then needs to be pure to have very low resistivity. The quality of the Cu is determined by its residual resistance ratio (RRR), calculated by dividing the resistivity at room temperature by the resistivity just above T_c (Equation 1.2). Since the Cu resistivity rapidly increases with even very small amounts of Sn, filament integrity is essential to maintain the high purity of the Cu.

$$RRR = \rho(300\ K)/\rho(19\ K) \tag{1.2}$$

Unlike its constituent elements, Nb_3Sn is brittle, and the A15 phase must be formed in-situ, with typical reactions in the 620-690 °C range for time up to hundreds of hours. Historically, Nb_3Sn has used several techniques of converting ductile Nb and Sn into the superconducting Nb_3Sn A15 phase. This included sintering [34], diffusion [35, 36], vapor deposition [31, 37, 38, 39], sputtering [40, 41, 42], a Nb tape dipped in molten Sn by GE [43], and even by shockwave [44]. The three current methods of conductor fabrication are bronze route [45], internal Sn as Rod Restack Process (RRP) [46] or Modified Jelly Roll (MJR) [47, 48], and Powder-In-Tube [49, 50].

The most simple and practical Nb_3Sn wire is made by the bronze route [51] where Nb rods are embedded in a Cu-Sn matrix and then drawn to final size. However, the Cu-Sn bronze solid solution which is ductile can only dissolve ∼9at%Sn, thus defining a limit to the amount of Sn, and therefore superconducting volume of A15 that can be formed, limiting the J_c(12 T, 4.2 K) to ∼1200 A/mm^2 [52].

In the internal Sn RRP method, the core of each superconducting filament is solid Sn which can be lightly alloyed with Cu [53] in order to strengthen mechanical properties. This solid Sn core is then surrounded by a Cu matrix embedded with many Nb rods as described in [54]. In this configuration, distributed diffusion barriers prevent the Sn from diffusing into the Cu stabilizer, and the Nb rods provide the Nb to form the A15 phase. RRP wires have J_c(12 T, 4.2 K) as high as ∼2,900 A/mm^2 with filament sizes in the 40-70 μm range [55]. Notably, the J_c of todays RRP conductors degrades when the filament diameter goes below about 50 μm [54]. Maintaining J_c at small d_{eff} is important for high field accelerator magnets.

In the PIT process, conductors are made by essentially filling a Nb tube with a Sn-rich $NbSn_2$ powder, cutting, and restacking to develop a multifilamentary wire. The historical development of this conductor and more technical details are discussed in the following section.

1.3.2 Development of Powder In Tube (PIT) Nb_3Sn wires

The PIT method of producing high J_c superconducting wires was first proposed at the Netherlands Energy Research Foundation (ECN) in 1975 by Van Beijnen and Elen who manufactured wires from vanadium tubes filled with powders of V_2Ga_5 or VSi_2 mixed with Cu, where Cu was added to lower the A15 formation temperature in the subsequent reaction to form superconducting V_3Ga or V_3Si [56]. The process was soon applied to Nb_3Sn using Nb tubes with $NbSn_2$ and Cu powders [57], ECN then produced wires with up to 180 filaments and an A15 $J_{c-layer}$ (12 T,4.2 K) of 2200 A/mm^2 [58], a value 2-3 times the best bronze route conductor at the time. Here the $J_{c-layer}$ is calculated by considering only the A15 area rather than the entire non-Cu.

By 1990 a 192 filament Nb_3Sn PIT wire was a standard configuration being manufactured in pre-production quantities with a non-Cu J_c(12 T, 4.2 K) of 1700 A/mm^2 [59]. Shape Metal Innovations (SMI) in the Netherlands then took over the process, focusing on two wire architectures: a 36 filament for very high field applications, and a 192 filament for high energy physics (HEP) magnets [60]. Continued optimization of filament size, powder quality, and manufacturing techniques led to a ternary A15 phase wire. In this case the wires were made with 192 Nb7.5wt%Ta tubes (Ta improves the high field performance [61]) typically containing $NbSn_2$ and Cu powders.

In 2002, PIT wires from SMI were thoroughly characterized [61] and, after heat treatment (HT), produced volume fractions of: 50% A15, 25% residual tube acting as a diffusion barrier (DB), and 25% residual core originally filled with $NbSn_2$ and Cu (Figure 1.6) [61]. This wire had a non-Cu J_c (12 T, 4.2 K) of ~2300 A/mm^2, a 40% increase since 1990, with the $J_{c-layer}$ nearly doubling to 4280 A/mm^2 in just over 20 years. These improvements were thoroughly characterized by digital micrograph analysis [62], magnetization [63], and strain dependence [64] among other techniques summarized in [65].

In 2006 European Advanced Superconductor (now: Bruker EAS) acquired the PIT technology from SMI. In addition to increasing production to the industrial scale, they also improved the design in two significant ways: one by switching from hexagonal to round filaments (allowing the radial A15 reaction to use the Nb-Ta tube more efficiently), and two by reducing the filament

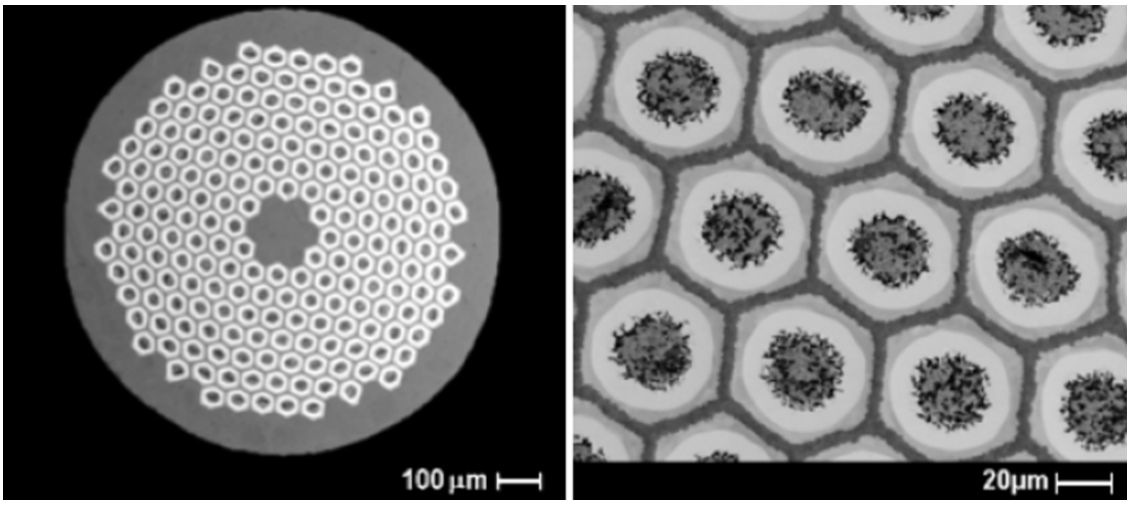

Figure 1.6: Image reproduced from [61]. FESEM-BSE images of polished, transverse cross-sections of a 192 filament PIT binary composite wire from ShapeMetal Innovation, Holland. The filament diameter is approximately 52 μm. In the right image, the dark circular regions are the filament cores, the light annuli are the reacted Nb_3Sn layers, the outer regions of the filaments contain unreacted Nb and the matrix is Cu. Both images depict a 675 °C 47 hour heat treatment.

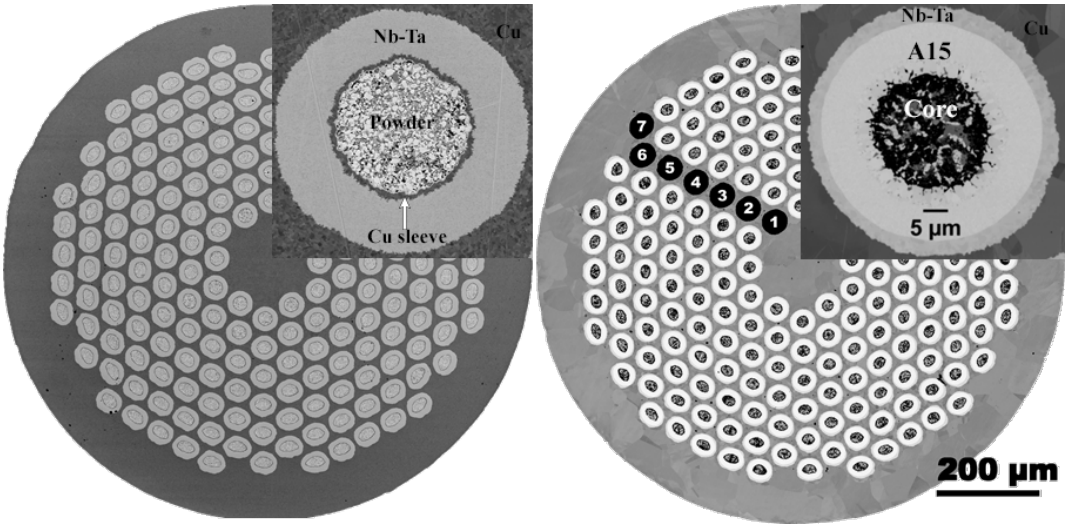

Figure 1.7: FESEM-BSE images of polished, transverse cross-sections of an unreacted (left) and reacted (right) Bruker PIT wire 1 mm in diameter with 192 superconducting filaments organized into seven rings within a matrix of stabilizing Cu. Inset image is of a typical filament from inner ring 1. Black is void, the next darkest phase is Cu, then the Nb-Ta barrier, with the thick annulus of Nb_3Sn appearing brightest.

diameter. PIT wires also see a degradation in J_c as filament size is reduced, however in PIT J_c begins degrading below ~40 μm [66] rather than at 50 μm for RRP. These redesigned PIT wires resulted in an increase of J_c (12 T, 4.2 K) to 2500 A/mm^2 by 2010 (described in this dissertation).

The PIT wires analyzed in this thesis were manufactured by Bruker European Advanced Superconductor and, once brought to final size, consist of 192 filaments (or 156 in one wire). Each monofilament is made of a Cu-clad Nb7.5wt%Ta tube inscribed by a thin Cu sleeve, containing mostly $NbSn_2$ and Cu powders as shown in the left side of Figure 1.7. The outermost Cu is for electrical stabilization.

1.4 Two main competing conductors: PIT and RRP

For future Nb_3Sn accelerator applications which demand much higher J_c, the only viable conductors currently available are internal-Sn (as RRP) and PIT, both processes currently dominated by Bruker as either Oxford Superconducting Technology (B-OST) or European Advanced Superconductors (B-EAS) respectively, both with J_c at or above 2500 A/mm^2 [49, 67].

Geometric distortion of the filaments during fabrication of the PIT strand leads to variation in the residual thickness of the diffusion barrier (DB), opening up the possibility of Sn leaking into the Cu if the A15 front locally reacts through the DB, reducing *RRR*. The quality of the Cu is directly correlated to high RRR, and maintaining its purity is essential for electromagnetic protection of the magnet. After a full reaction, the non-Cu area is composed of a residual Nb-7.5wt%Ta DB (20-24%), an annulus of superconducting A15 (50-60%), and a remnant core (19-24%) which contains: alpha (α) and epsilon (ϵ) Cu-Sn phases, disconnected A15 grains, and voids (Figure 1.7). The connected, superconducting A15 layer is further broken down into two morphologies: the desired small grain (SG) A15 which is 70-75% of the A15, and 25-30% of large grain (LG) A15 which does not carry any current [68]. This is because the large grains of A15 are largely disconnected from each other, or otherwise have Cu in the grain boundaries which creates a superconducting-normal-superconducting pathway, preventing current flow (Figure 1.8). Additionally, the grain boundary density is too low to provide effective vortex pinning. As only the SG A15 layer carries current, we can further consider the quality of the A15 by defining a $J_{c-layer}$ that is normalized over only the A15 area which carries current in transport. For both PIT and RRP we normalize this J_c over the SG A15 layer, for PIT this is 40-45% of the non-Cu cross-section, while for RRP the SG

A15 is about 60% of the non-Cu area (Figure 1.9). Typical $J_{c-layer}$ values for PIT range from 5500-6500 A/mm^2, while RRP is slightly lower, varying from 4500-5300 A/mm^2 [69].

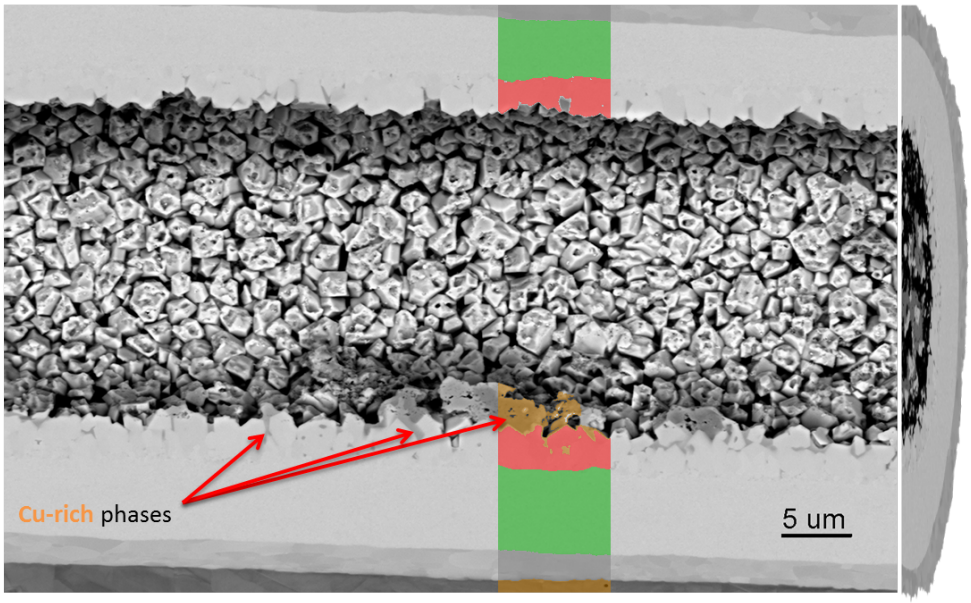

Figure 1.8: FESEM-BSE image of a polished, longitudinal cross-section of a filament in a reacted Bruker PIT wire. The cross-section is partially colored to distinguish between phases and morphologies. Nb is colored in gray, SG A15 in green, LG A15 in red, and Cu in orange. In this longitudinal cross-section the large, poorly connected grains of A15 are clearly seen, as well as the penetrating Cu-rich phases.

In a recent detailed evaluation of a 54 filament Nb7.5wt%Ta RRP conductor by Tarantini et al., a J_c(12 T, 4.2 K) of 3,000 A/mm^2 was obtained in a wire whose sub-elements are made of ~60% A15, and a protective residual DB of only ~7%, [69], substantially less than PIT wires. RRP designs, however, have recently evolved to a greater number of sub-elements (108 to 169) and with the finer filament size, the DB fraction increases to ~10% and the J_c drops to ~ 2750 A/mm^2, diminishing the difference between PIT and RRP. Nonetheless, for RRP wires most of the A15 phase is well connected SG A15, and the amount of disconnected or LG A15 is small enough that it is difficult to even measure [70].

T_c variation with Sn content. In Nb_3Sn PIT conductors there tends to be a substantial T_c gradient within the superconducting layer, dictated by the Sn content in the A15 phase (Figure 1.5) [32]. The effect of such a gradient has been thoroughly investigated in [68] and is most

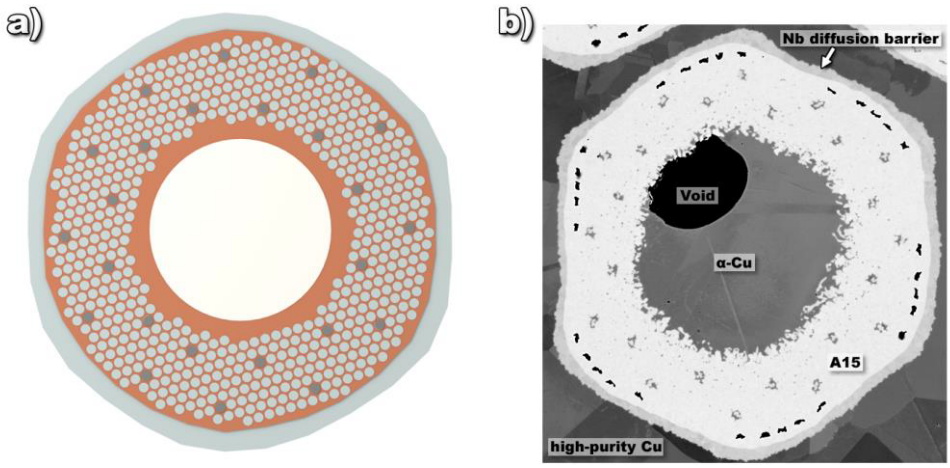

Figure 1.9: Reproduced from [54]. (a) A sketch of a standard sub-element cross-section before reaction. (b) a fully reacted RRP sub-element showing the monolithic Nb_3Sn ring that is formed after reaction.

easily characterized by correlating the results from various measurement techniques, including heat capacity, magnetization, and microstructure from SEM image analysis (Figure 1.10). The results show a clear distribution of Sn related directly to the different A15 morphologies present in the wire. Considering the position of the Sn source at the filament center, and the outward radial diffusion, the morphology with the highest Sn content, and therefore T_c, is the disconnected A15 grains in the filament cores with T_c above 18 K. Continuing to move radially outward from the Sn source, the LG A15 has T_c from 17.5-18 K, immediately followed by the equiaxed SG A15 which spans 17-17.5 K. The morphology of A15 furthest from the Sn source is a layer of columnar grains at the Nb-Ta diffusion barrier which generates a low T_c tail extending down to 6 K. As T_c decreases with reduced Sn content, optimized reactions should diffuse as much Sn as possible into the A15 layer to homogenize the Sn content near stoichiometry.

Grain boundary pinning. Since grain boundaries in the SG A15 act to pin vortices, keeping the A15 grains as small as possible is integral for a successful A15 reaction. Typically the grain size should not exceed 200 nm for a practical conductor (Figure 1.11), and more recent results have shown the SG A15 in PIT conductors to be in 90-110 nm range (chapter 3).

The two requirements for an optimized HT that we focus on here are that RRR should not degrade below 150 and that J_c (12 T, 4.2 K) should exceed 2450 A/mm^2. Throughout this disser-

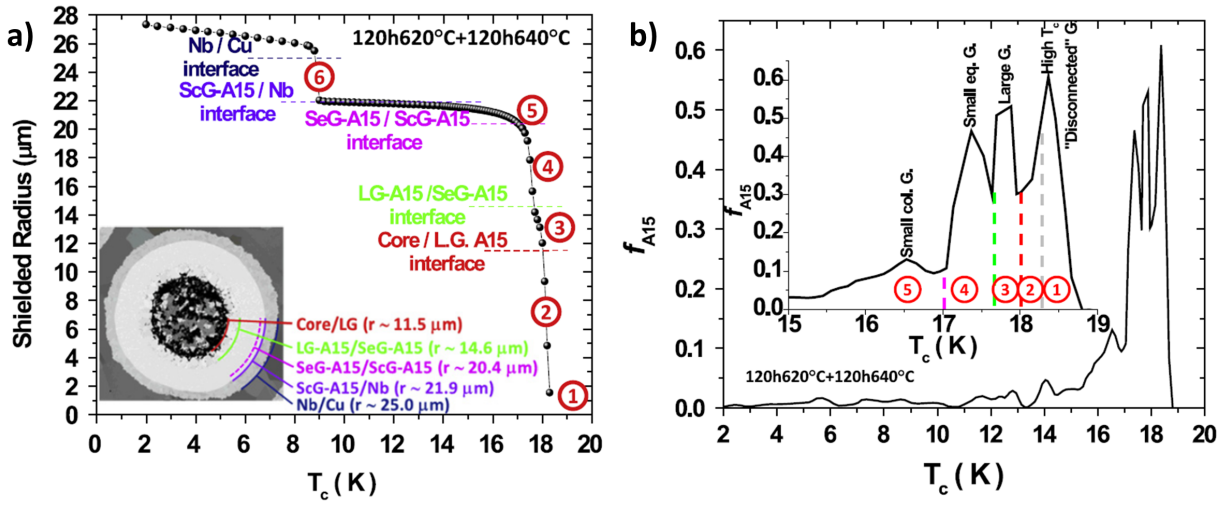

Figure 1.10: T_c distribution of the A15 phase for a Nb_3Sn PIT wire reproduced from [68]. (a) The shielded radius versus temperature estimated from the magnetization measurement. (b) T_c distribution of the A15 phase for the PIT wire. The inset magnification shows the high temperature region. The vertical lines correspond to the T_c of the different interfaces in the filament as determined by (a)

tation samples may be identified by their final HT temperature and time (e.g. 625 °C for 280 h is 625/280) and their wire diameter. The tight constraints on high J_c and high RRR meant that optimized heat treatments varied only from 620 °C to 670 °C for 50-240 h.

1.5 Bundle barrier PIT wires

A new architecture of Nb_3Sn PIT wire was designed in order to address the limitation of A15 volume formed, while also maintaining a high RRR. The 'bundle barrier' PIT design has increased Sn in the core compared to previous designs, allowing for longer reaction times to form more superconducting A15. However, since longer reactions tend to degrade *RRR*, the addition of a bundle barrier was made which surrounds the filament bundle, the purpose being to maintain a high purity annulus of Cu on the outside of the bundle barrier for electrical stability (Figure 1.12). BEAS sent nine wires to the ASC for analysis of microstructure and electrical properties, both to be discussed in section 5.2. The bundle barrier samples received had variations in Sn content, and while BEAS did not want to disclose the exact at%Sn in the core, they advised the wires were either medium, high, or very high Sn. The implication is that the previous, non-bundle barrier wires have

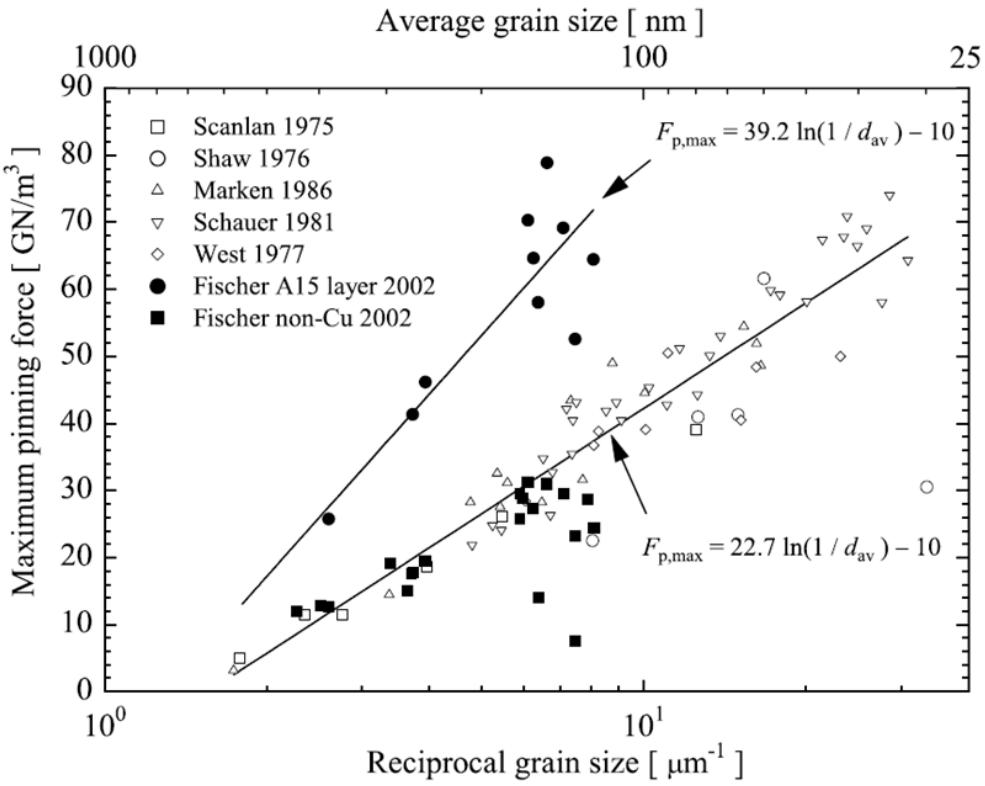

Figure 1.11: A semi-logarithmic plot showing the maximum pinning force as a function of reciprocal grain size, average grain size is included at the top for reference. The lower data points are normalized over the non-Cu area, while the upper, closed circle data points (Fisher A15 layer 2002) were normalized only over the A15 layer, providing a higher pinning force.

a comparatively 'low' Sn core. Other factors that were changed were the Cu:non-cu ratio, filament size, bundle barrier thickness, and ratio of Cu inside and outside of the bundle barrier. The best bundle barrier wire showed a marked increase in J_c(12 T, 4.2 K) up to 2658 A/mm^2, with another wire showing $J_{c-layer}$>7000 A/mm^2.

1.6 Motivation for this work

The most widely used process for manufacturing Nb_3Sn to date has been the bronze route [51], however this process can only achieve J_c (12 T, 4.2 K) on the order of 1200 A/mm^2 [52], much too low for accelerator magnets [66, 73]. This leaves PIT and RRP wires as the primary candidates for

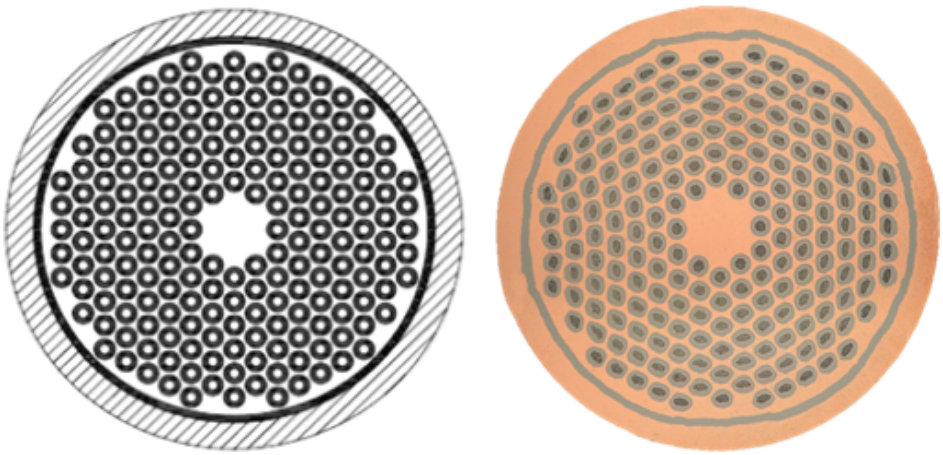

Figure 1.12: On the left is a schematic overview of the bundle barrier wire [71], on the right is a 0.85 mm diameter, unreacted bundle barrier wire fabricated by Bruker EAS [72].

such magnets, to date reaching a maximum J_c(12 T, 4.2 K) of ~2700 A/mm^2 and 3000 A/mm^2 respectively [74, 75]. While RRP surpasses PIT in maximum J_c(12 T, 4.2 K), PIT develops a higher $J_{c-layer}$ of now ~7000 A/mm^2, RRP achieving ~5200 A/mm^2 [69], in both cases $RRR >$ 150. However, these J_c values have remained rather stagnant for nearly 15 years.

The development of Nb_3Sn as an accelerator conductor is currently being driven by the prospect of upgrading magnet systems, such as the Large Hadron Collider (LHC) at CERN where the High-Luminosity Upgrade will rely on Nb_3Sn for generating higher magnetic fields in both dipoles and quadrupoles, in addition to the cable test magnet FRESCA2 [74]. Future R&D on Nb_3Sn might be at an end except for the Future Circular Collider (FCC) [66], which enumerates three main goals in developing the conductor further: develop fine filament size (<20 μm), maximize J_c (>1500 A/mm^2 at 16 T, 4.2 K), and maintain electromagnetic stability by keeping the RRR of the stabilizing Cu >150 before cabling [66, 76]. While RRR, J_c, and d_{eff} requirements may be satisfied independently, a wire which satisfies all three is still challenging.

To determine if the powder-in-tube process could be improved and satisfy the FCC requirements we thoroughly characterized the present wire by observing phase evolution, microstructure, and filament deformation, correlating all three to draw comprehensive conclusions. This suggested multiple routes for improvement, resulting in the fabrication of a bundle barrier PIT wire. We additionally explored heat treatment variation as a possible method to improve the conductor.

CHAPTER 2

EXPERIMENTAL TECHNIQUES

There are many tools and techniques available to study applied superconductivity, and in this chapter I will discuss some more common techniques employed in this dissertation, and how novel techniques were designed to improve both the accuracy and the speed of the analysis. The majority of our work depended on heat treating wires in a reaction furnace and then imaging the reacted wires in a Field Emission Scanning Electron Microscope (FESEM) to observe the microstructure and the morphologies of A15 which form. Just as important as the SEM images is our suite of digital imaging analysis tools to measure areas and shapes of specific components of wire cross-sections, correlating them with RRR and J_c. We also made many of the J_c and RRR measurements at the ASC using a 15 T solenoid magnet and Physical Property Measurement System. We additionally used a Differential Thermal Analysis (DTA) technique which provides more data on the phase evolution than by microstructural analysis alone.

I additionally designed a few novel analysis techniques. This included a progressive etch-and-measure technique to deconstruct RRR or J_c profiles by each filament ring within a wire, and what I call "metallographic tomography", whereby detailed features can be measured along a length of wire by SEM imaging rather than X-rays. To further extend the power of our digital imaging, Peter Lee at the ASC has created many macros and other imaging tools which allow the comprehensive analysis to be done with high accuracy and statistics in a practical time scale. The results of these experiments will be presented and discussed in the following chapters.

2.1 Digital imaging

2.1.1 Sample preparation

For any digital imaging, proper sample preparation is important for getting reliable data. The two biggest considerations are that the sample must be as flat as possible, and there must be a conductive path for electrons to leave the sample and avoid over charging during SEM use. If there is no conductive path, electrons will continue to build up, and the area becomes more saturated

and appears brighter. This build up continues until there is a high enough potential to discharge across the sample as bright horizontal lines. These discharge lines make the images unusable for analysis as the discharge line shifts the boundary between phases. This effect is clearly seen at the wire edge in the inset image of Figure 2.1.

To provide a conductive path, the wires are mounted for imaging in a puck made from a powdered conductive filler, which upon heating and increased pressure, sinters into a solid conductive puck. Holes can then be drilled in the puck and small lengths of wire (∼1 cm) are inserted into each hole and then covered with powdered filler, again pressed and heated into a solid puck, but now with embedded wires. The temperatures and pressures reached in the mounting press are not high enough to react the wires; however, in some cases where we try to observe small compositional gradients early in the reaction, we chose to use a conductive epoxy. This is simply made by adding a very fine conductive powder to an epoxy before curing.

After preparing a conductive puck, it must be polished to ensure a flat surface. A flat surface is required because rough surfaces create a poorly defined measurement condition whereby geometric effects cause changes in how the electrons scatter and are absorbed in the SEM [77]. Buehler Ecomet 250 auto-polishing machines were used for most of the polishing, allowing for great control over how much force is applied and the rotation speed of the head and base. The polishing procedure begins by removing about 1 mm from the top of the puck with a coarse silicon carbide (SiC) polishing pad to remove any damage from cutting the wire prior to mounting. We then increase the grit size from 320, 400, 600, to 800, consistently decreasing surface roughness by removing the previous pads damage. These grit sizes are based on the average SiC particle size after passing through various sieves, and are shown in Table 2.1 [78]. For example, after the 800 grit polishing step, we should be able to separate any features that are larger than 13 μm. At this polishing resolution, we switch from SiC pads to a nylon pad that is used in combination with a diamond suspension containing particle sizes of either 6, 3, or 1 μm. After serial polishing with diamond suspensions of decreasing particle size, the conductive pucks are put into a Buehler Vibromet vibratory polisher, using a 50 nm colloidal silica solution to reach the surface smoothness required for the SEM.

After some hours in a vibratory polisher, the sample surface is cleaned with a nylon pad and metallographic soap to remove any stains from the surface that would affect the quality of the image. At this point, it is not uncommon to further increase the conductivity of the puck by

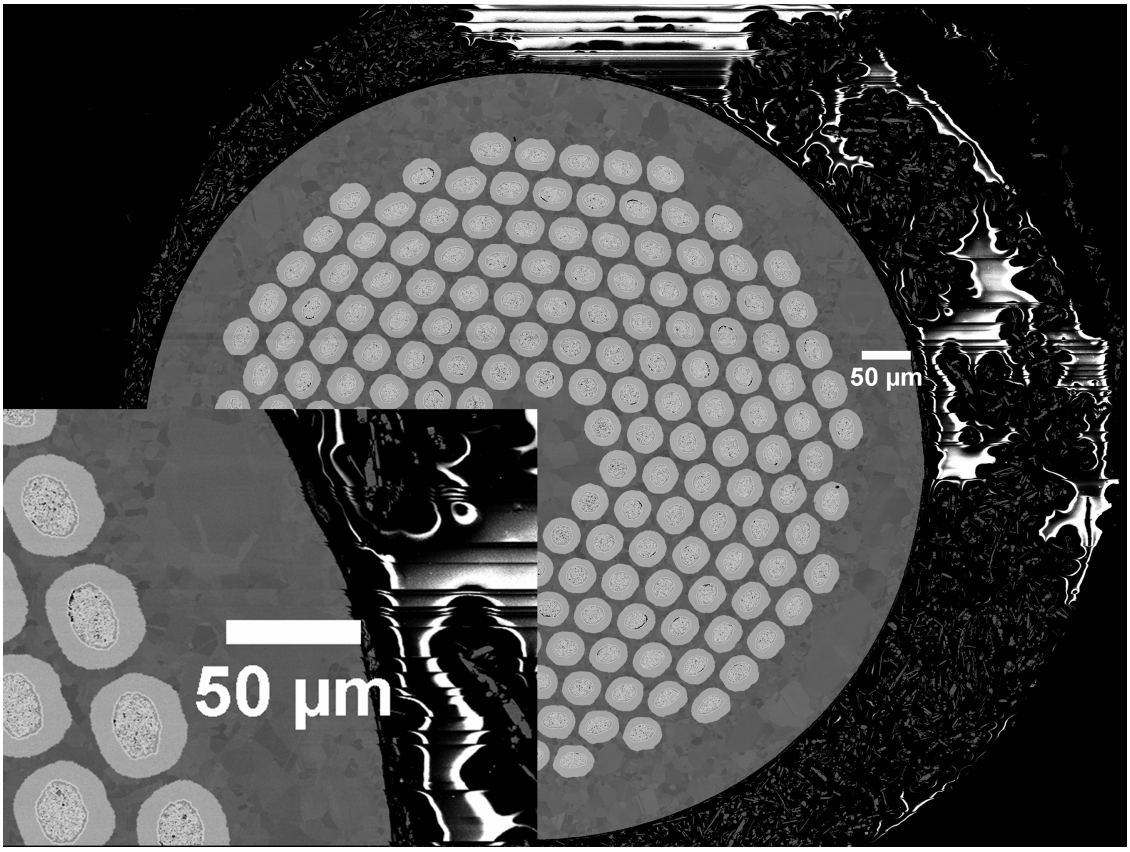

Figure 2.1: FESEM-BSE image of a polished cross-section showing the effects from overcharging. Areas on the right side of the image are white from a build up of electrons in the conductive filler. This build up will discharge, causing horizontal lines across the entire image as shown in the inset, shifting the boundary between phases. This effect is clearly seen at the wire edge of the inset image.

coating the surface with carbon, or using silver paint to draw conductive paths around the wires. However, we found this was unnecessary and rarely encountered overcharging issues as as shown in Figure 2.1.

2.1.2 Microscopy and the Scanning Electron Microscope (SEM)

All digital imaging was performed on a Zeiss 1540 Crossbeam®(XB) or Energy Selective Backscatter (EsB) Field Emission Scanning Electron Microscope (FESEM), nominally identical for our use. Nb_3Sn wires are predominately imaged by using a back-scattered electron (BSE) detector, whose intensity in the FESEM is sensitive to atomic number (Z), with phases of a higher effective Z appearing brighter in the BSE image as shown in Figure 1.7. In this figure, the brightest phase

Table 2.1: Grit size of SiC pads and their corresponding average particle size in μm. After the 800 grit step, features larger than 7.8 μm can be distinguished.

ANSI grit	average particle size (μm)
320	29.5
400	18.3
600	10.6
800	7.8

Table 2.2: Elements and phases of interest for Nb_3Sn PIT wires and their corresponding atomic weight. In the case of compounds, an atomic average of constituent elements is used as an effective atomic weight. The larger the atomic weight, the brighter the phase will appear in the SEM

Element or Phase	atomic weight (amu)
Cu	63.5
Epsilon (Cu_3Sn)	77.3
Eta (Cu_6Sn_5)	88.6
Nb	92.9
Nb4at%Ta	96.4
Nb_6Sn_5	104.6
$NbSn_2$	110.1
Nb_3Sn	112.3
Sn	118.7
Ta	180.9

is the Nb_3Sn A15 phase, while the darkest phase is Cu, and voids are in black. The elements and phases of interest to this work are provided with their atomic mass in table Table 2.2.

After a full reaction, the phases of interest are the Cu stabilizer, the remaining Nb4at%Ta diffusion barrier, the superconducting Nb_3Sn A15 phase, and remnant Cu and Sn phases in the core. Fortunately, these phases are sufficiently different in atomic weight to allow for quick identification. On the other hand, there are multiple points during the phase evolution before the A15 formation is complete where some phases can be quite difficult to distinguish. Under 200 °C, for example, it can be challenging to distinguish between the η phase (Cu_6Sn_5) in contact with the Nb4at%Ta diffusion barrier. Additionally, it is difficult to distinguish between all of the Nb-Sn phases above 630 °C: $NbSn_2$, Nb_6Sn_5, and Nb_3Sn. Fortunately, only two of the three Nb-Sn phases exist simultaneously;

first $NbSn_2$ + Nb_6Sn_5 around 630 °C, and a short time later the Nb_6Sn_5 + Nb_3Sn. To better distinguish between these phases and the boundary between them, we apply image enhancements via ImageJ [79] or Photoshop, as discussed in the following section, subsection 2.1.3.

When imaging any samples, the penetration depth of the primary electron beam should be considered to ensure a representative volume is being sampled. Figure 2.2(a) shows the relative penetration depth between different signals, and in (b) the clear dependence of penetration depth on accelerating voltage is shown in a simulation, where blue tracks are primary electrons that terminate in the sample, and the red tracks are primary electrons which ultimately escape as BSE.

In addition to separating phases by back-scatter contrast, we frequently use Energy Dispersive X-ray Spectroscopy (EDS) to more accurately identify chemical compositions. This is useful if specific compositional information is needed. For example, the A15 phase can easily be separated in the filaments by contrast alone; however, this provides no information on the Sn composition within the A15 phase, which can be measured by EDS. One limitation to the EDS is that the sampling volume required to get a reliable signal is substantially higher than other microscope techniques such as BSE or secondary electron imaging as shown in (Figure 2.2) [80]. For EDS, we measure X-rays that are generated deep within the interaction volume which must be uniform for accurate compositional data. Since the interaction volume may be as large as a 1 μm^3, features that are smaller can be difficult to measure without sampling the surrounding area and introducing signal from undesired phases. Additionally, to excite peaks of a desired energy, the accelerating voltage needs to be at least 1.5x the peak energy [81] (though 2x is best if possible), and the sampling volume increases with the accelerating voltage. This means for higher energy peaks of interest, such as Ta and Cu whose α-lines are around 8 keV, we need to ensure a large, uniform volume so that the signal is only generated from the phases and elements of interest. These constraints limit the spatial resolution of EDS to the micron range in many cases rather than nanometer range as we see for BSE. This mostly limits our ability to detect small amounts of Ta and Cu in the different Nb-Sn phases during the phase evolution under 400 °C.

2.1.3 Digital analysis of SEM images in FIJI

After imaging in the SEM, we can use image analysis software to quantitatively measure the area fractions of each phase, the thicknesses of the remaining Nb(Ta) barrier, and geometric features such as aspect ratio. This analysis is made possible by the widely used open-source software package,

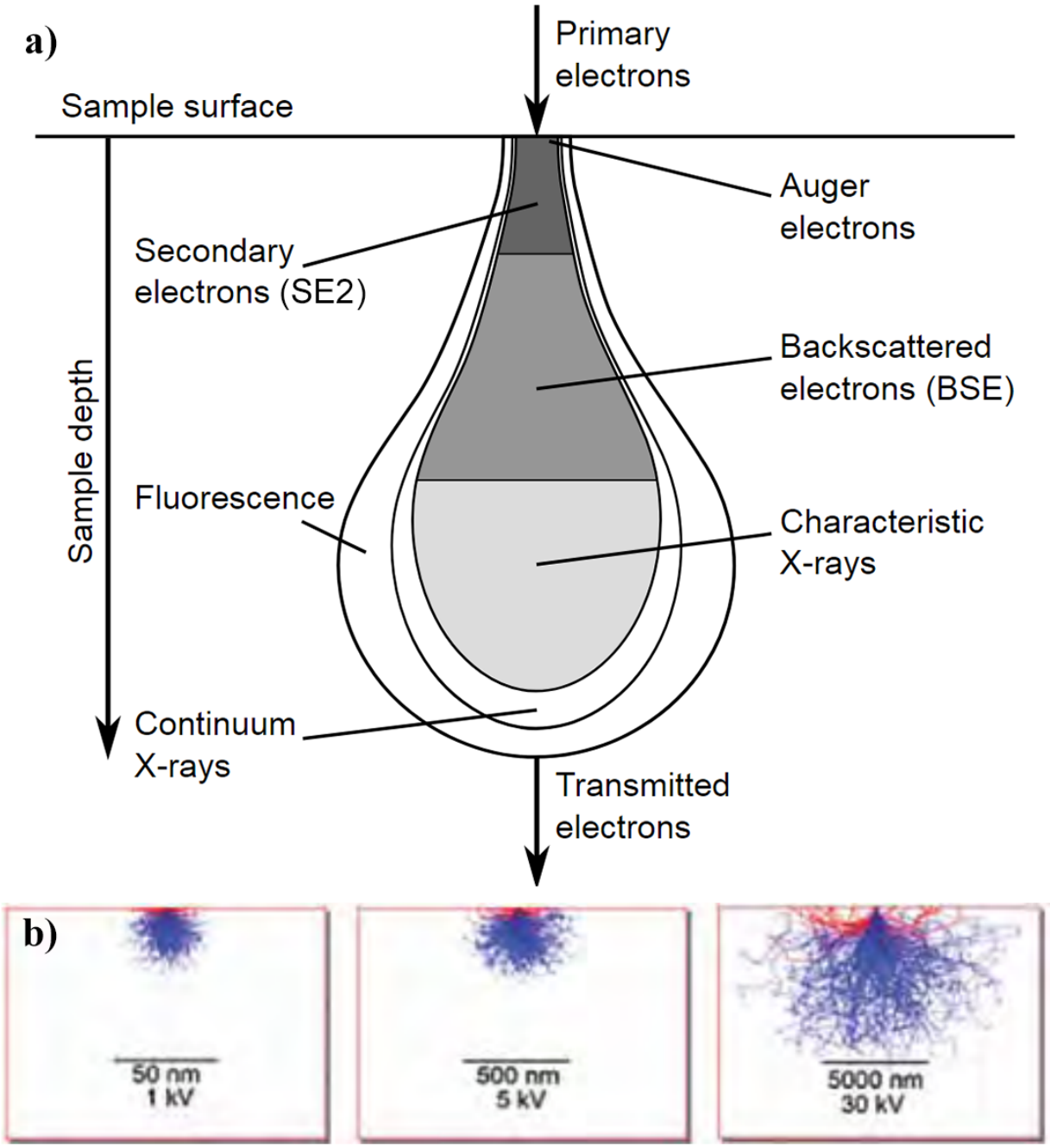

Figure 2.2: Different detectors make use of different sampling depths. While secondary electrons (SE2) is very shallow, back scattered electrons (BSE) come from a larger and deeper volume, closer to the depth of X-rays generated in EDS (a). In (b), a simulation of interaction volume vs accelerating voltage is shown, where blue tracks are primary electrons that terminate in the sample, and the red tracks are primary electrons which ultimately escape as BSE. Image adapted from [80].

FIJI [82] (based on ImageJ [79]), allowing us to make high precision comparisons between samples. In addition, Photoshop is occasionally used to supplement missing features in FIJI. Beyond standard tool-sets native to FIJI, Peter Lee at the ASC has enormously expanded its capabilities by creating macros and other image analysis programs that allow rapid characterization of many images on a practical time scale, including options for labeling and preparing images for publication.

Since the contrast in the BSE images is provided by the variation in atomic weight, each phase can be associated with particular gray values that range from 0 (black) and 255 (white). However, there is no standard calibration to the gray value of a phase in a histogram, and the mean gray value for a phase will vary depending on many factors in the microscope, such as accelerating voltage, back-scatter detector voltage, and working distance. There are additional influences from within the sample, most notably grain orientation. While grains with different orientations are not far apart in gray value, it is enough to cause each phase to form a Gaussian distribution around a average gray value (Figure 2.3). The important consideration is to make sure no part of the image is saturated as either white or black, and if possible to ensure a clear minimum between phases on the histogram.

The main mechanism for accurate image analysis is to "threshold" the image so that the 255 gray channels collapse into a binary distribution of only black and white. This is done by selecting a gray value in the histogram such that every pixel with a gray value beyond the threshold value will become white, while those below the threshold value become black. After thresholding, groups of black and white pixels can be measured for area or shape.

This works well for samples that are extremely clean and flat because nearly all of the image contrast is provided by the atomic weight of the phase. However, if there are any stains, dust, or scratches on the sample, erroneous features can arise during the threshold that do not match the surrounding area (i.e. a dark speck of dust in the light A15 phase). This software allows us to isolate the Cu area from the filaments regardless of such features, allowing an accurate analysis even with polishing artifacts present. Consider the histogram in Figure 2.3, I chose a threshold value of about 200, which converts all of the pixels below 200 (this includes the Cu and void area) into black pixels, while those pixels beyond the threshold value (the Nb-Ta DB and A15 phases) will become white (Figure 2.4b). Now we can select the continuous black area in Figure 2.4b, which corresponds to the stabilizer Cu, and then use the software to select the opposite area (the

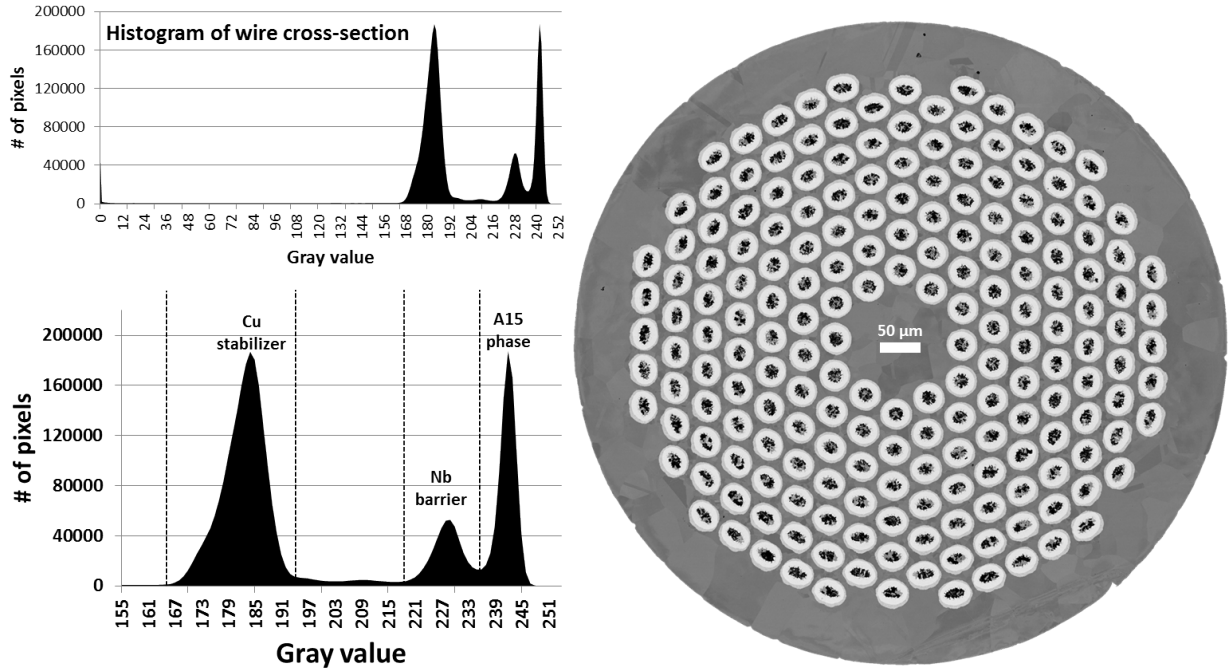

Figure 2.3: A histogram showing the gray value distribution of the wire cross-section shown to the right. The top histogram is a full overview of all 255 gray values, with the bottom histogram a magnification of the range 155-255.

filaments) and then fill them as white Figure 2.4c. We can then invert the colors in (c), to produce (d). To move to the next step in the image analysis, we select all black pixels in Figure 2.4d, and then copy the area out of the original image (Figure 2.4a), to separate the Cu (Figure 2.4e), and produce an image with only filaments (Figure 2.4f) .

The process shown in Figure 2.4 gets us through the first step in our image analysis, which is to determine the Cu:non-Cu ratio. This is done at a relatively low magnification of 90-100x, corresponding to a resolution of ∼373 nm per pixel. For the next stage of the image analysis, we could carry forward only the filaments from (Figure 2.4f), however we need higher resolution to accurately measure the different A15 morphologies. For the remaining image analysis I took images at a higher magnification of 300-700x where the resolution improves to 123-52 nm per pixel respectively. The process of thresholding is now repeated to separate the Nb-Ta barrier from the A15 layer (Figure 2.5), This Nb-Ta layer can be used to determine the occurrence of barrier breakthrough, where the residual Nb-Ta layer thickness goes to zero and the A15 phase is in direct

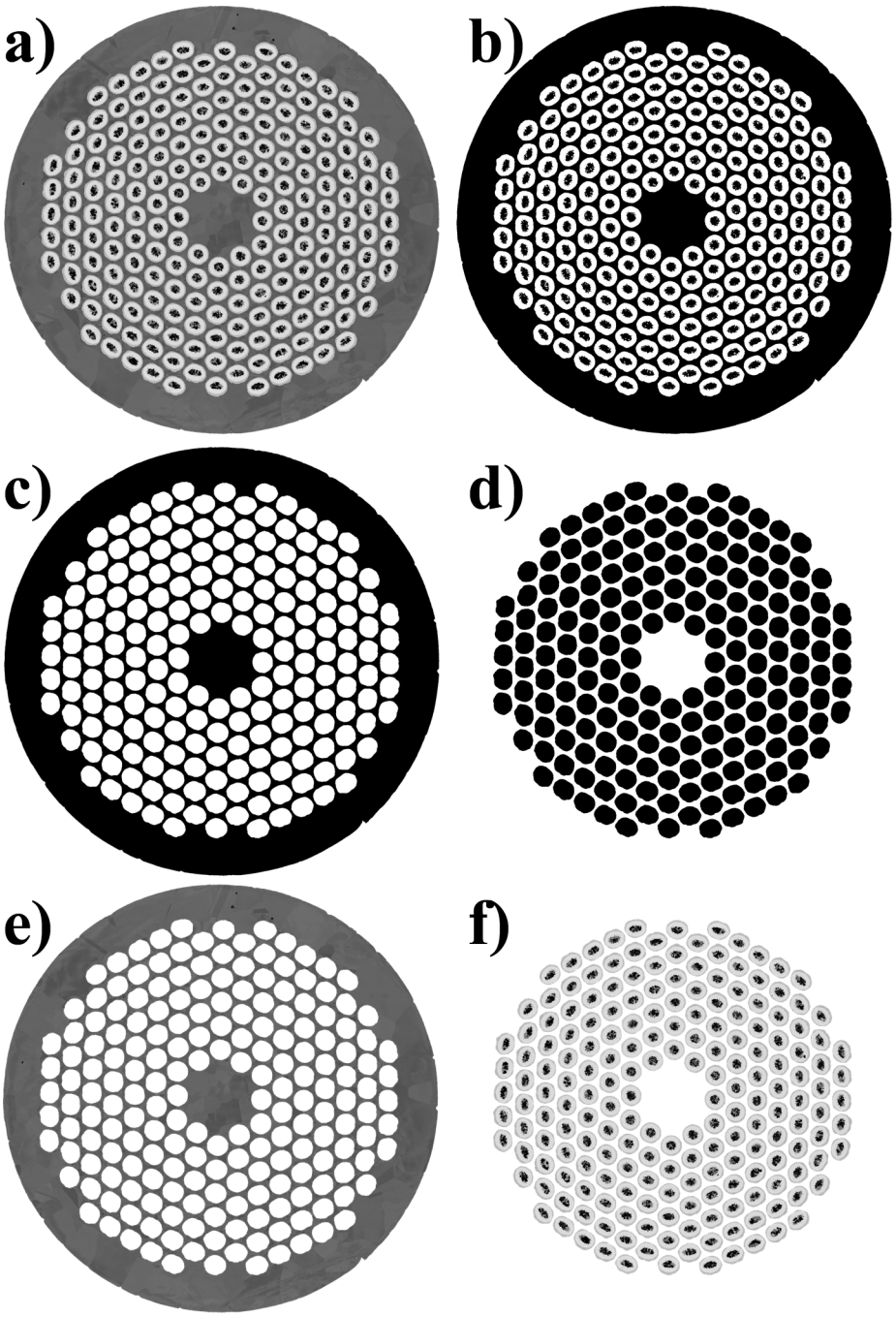

Figure 2.4: The top row contains an FESEM-BSE image of a polished cross-section (a) and its binary image from thresholding to separate the Cu and non-Cu areas (b). In the center row, the Cu stabilizer is shown on the left (c), and the filament areas are shown on the right (d). In the bottom row, we used the black areas from the middle row as selection areas in the original image, allowing us to separate the Cu (e) and non-Cu (f) areas.

contact with the Cu stabilizer. We can continue in this fashion, carrying forward everything within the barrier, and then separate the A15 layer from the remnant core (Figure 2.6). The remnant core can then be easily separated into A15, Cu, and void that arises from the porous initial powder (Figure 2.7). We show each image with its histogram, the dashed lines labeling the approximate phase boundaries to compare as different layers are removed from the image cross-sections.

All of these steps are readily reproducible, and in many cases macros can be made in FIJI that can process a folder containing many images automatically. The one exception to this is the separation of the small and large grain A15 morphologies as they have the same atomic weight, and therefore the same contrast, which is indistinguishable in terms of gray value. The LG and SG A15 layers must then be manually traced and separated. While this is not exactly reproducible compared to choosing a single gray value to threshold, steps can be taken to ensure nominally identical values when the same measurement is made independently over multiple trials.

For example, in Photoshop we can use the 'magnetic lasso' tool, magnetic in the sense that it is attracted towards pixels within a selection area of particular contrast set by the user. As an example, we might set the selection tool diameter to 10 pixels, and the contrast to 10%. Then, within the selection circle, Photoshop will try and find the pixel closest to a 10% contrast difference with its surroundings (Figure 2.8). This is helpful in the case of separating A15 morphologies because of the Cu precipitates that tend to form between the LG and SG A15 layers. While not continuous enough to allow for automatic separation via thresholding, these small Cu islands still provide anchors of contrast that allow the magnetic lasso to grab on to a reasonable perimeter, and, because these are real features in the wire, it is closely reproducible.

Additionally, the magnetic lasso tool can be made more effective by applying the "levels" option in Photoshop. This allows a small range of gray values to be stretched over all 255 channels which increases the overall contrast (Figure 2.9). This is particularly helpful to further improve the magnetic lasso tool that depends on the contrast within the selection circle. However, this method should only be used to increase contrast in a narrow range of values (just the A15 layer for example), as this method pushes all of the pixels outside of the chosen range into either black or white values. In Figure 2.9 the Cu gets shifted into the black and the filament cores all appear very dark except for the bright spots of A15.

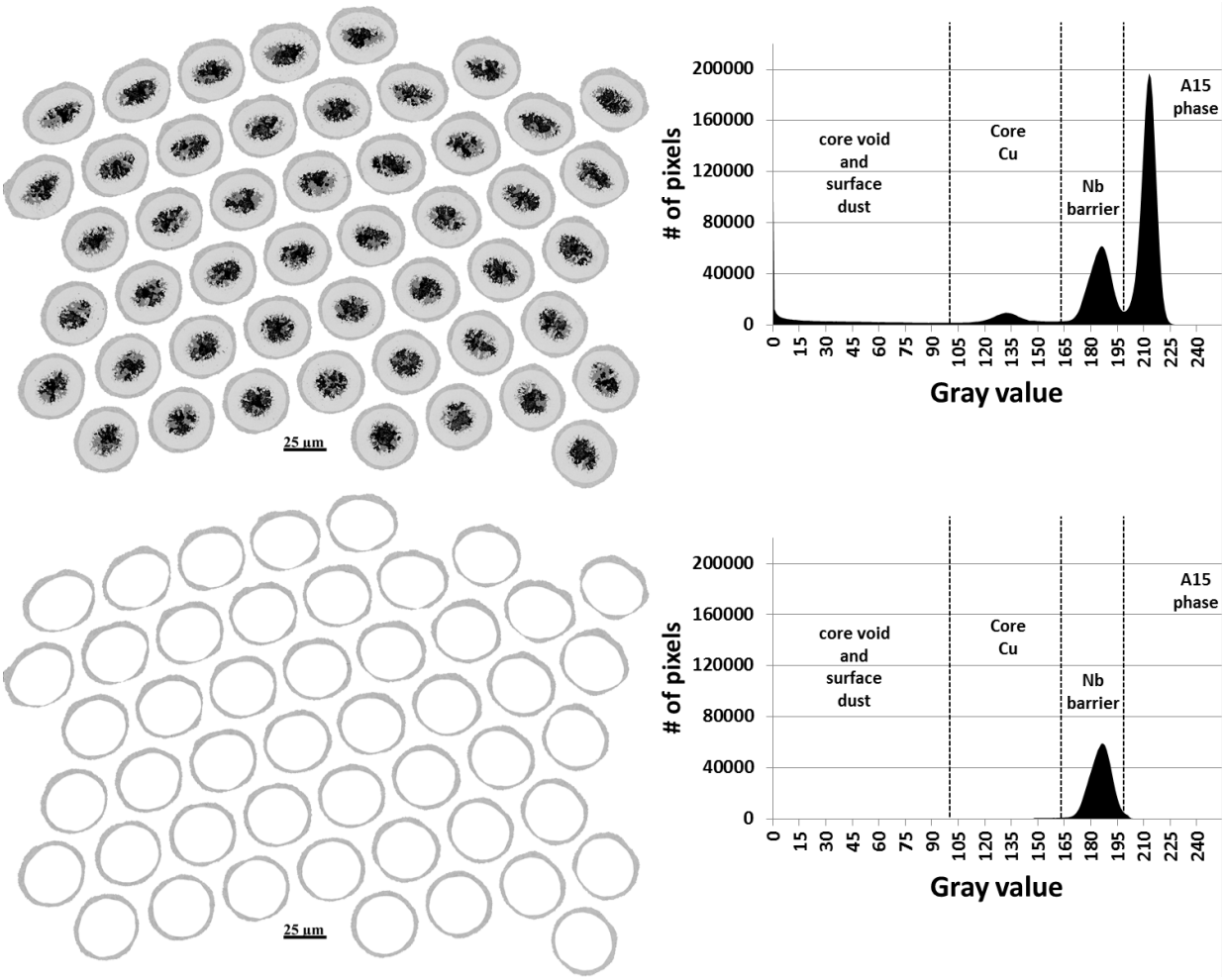

Figure 2.5: FESEM-BSE image of a polished cross-section (left) which has been thresholded to separate the Nb-Ta diffusion barrier from each filament. On the right is the histogram showing the distribution of gray values in each image, and where the phases were separated.

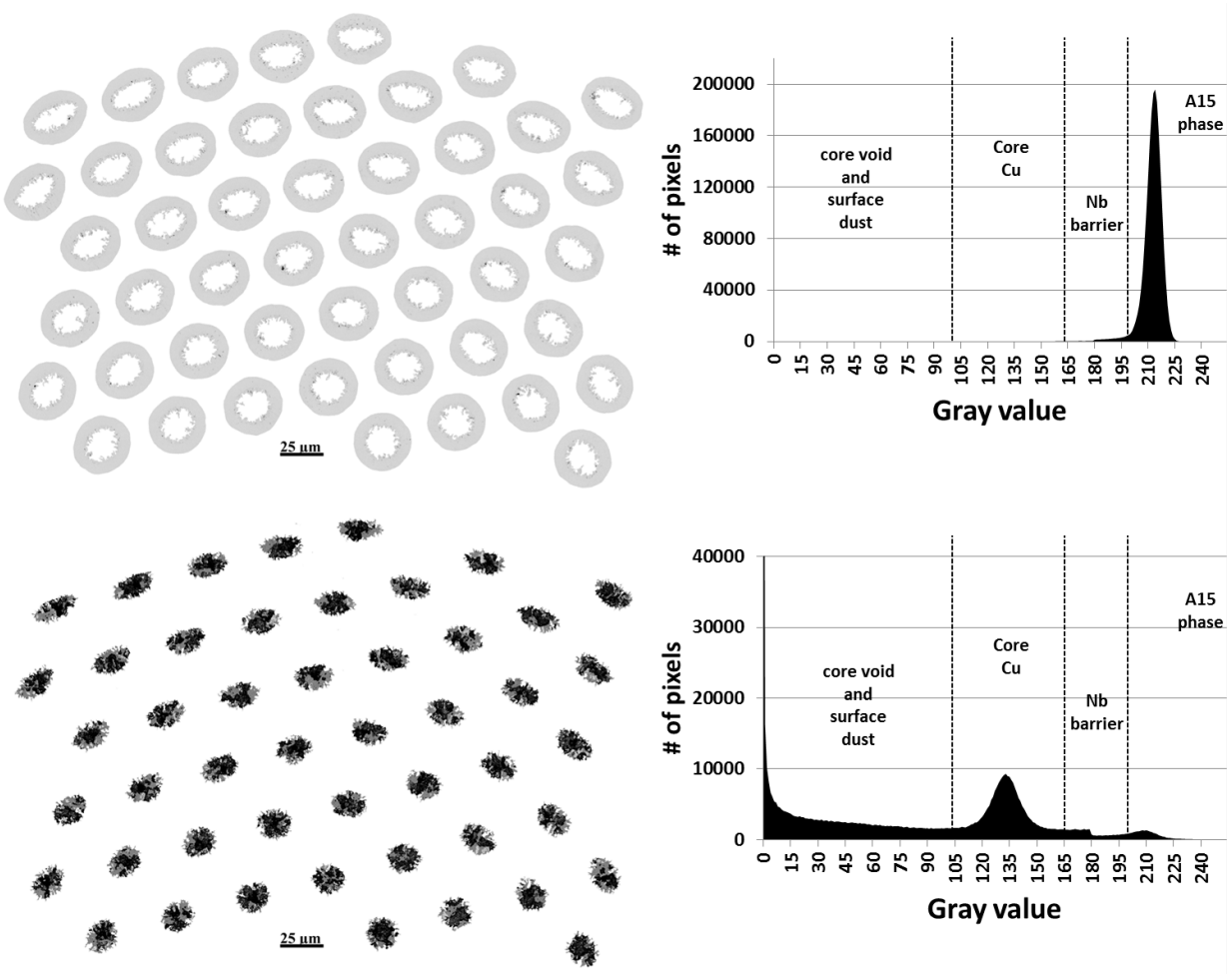

Figure 2.6: FESEM-BSE image of a polished cross-section (left) which has been thresholded to separate the A15 layer (top) and the remnant core (bottom). On the right is the histogram showing the distribution of gray values from each image, and where the phases were separated. While we see some dark spots in the A15 layer at the top, there are only $\sim$1600 dark pixels spread out over about 150 channels, and so it appears as 0 pixels on this scale

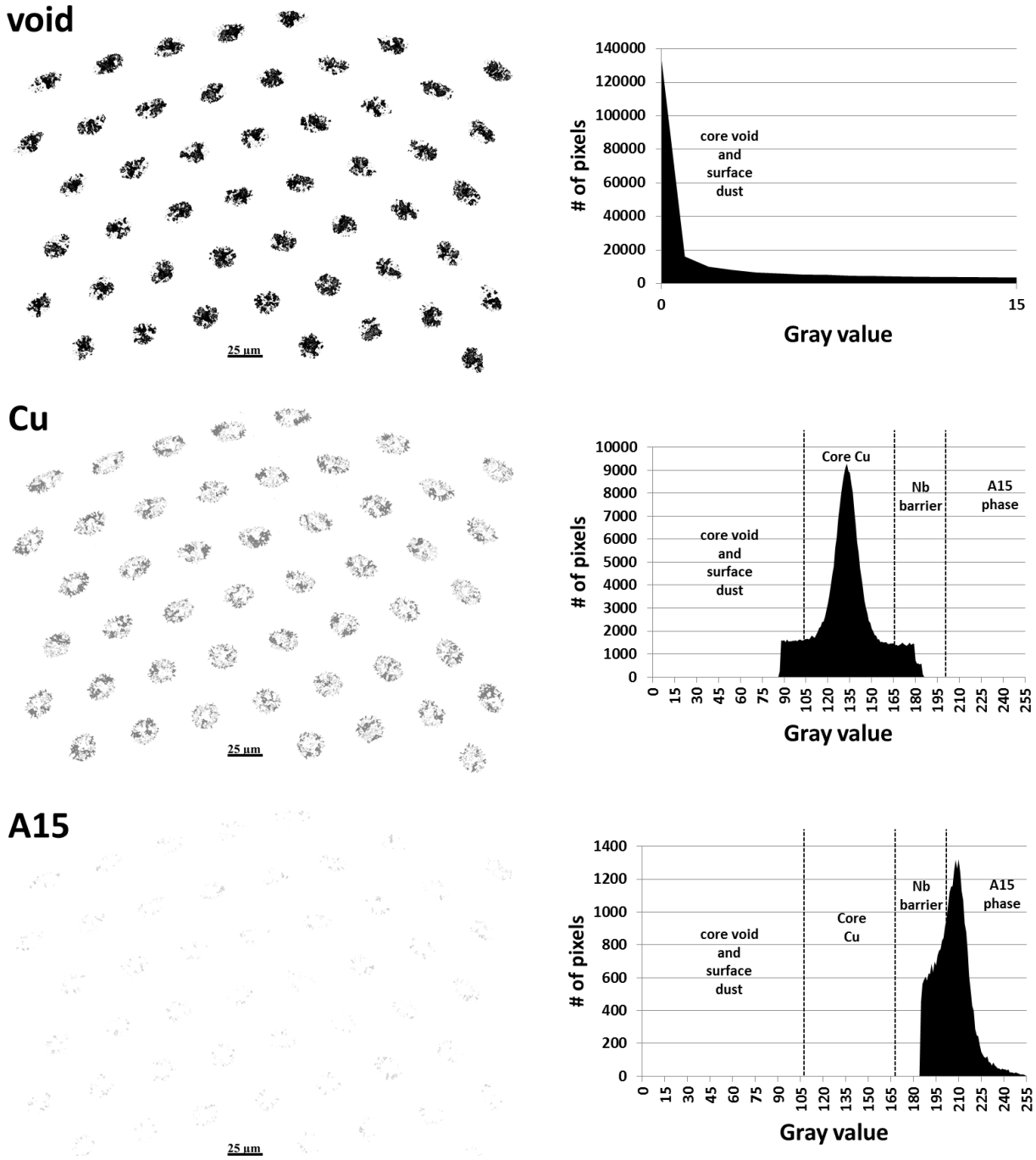

Figure 2.7: FESEM-BSE image of a polished cross-section (left) which has been thresholded to separate the core into A15, Cu, and void areas. On the right is the histogram showing the distribution of gray values from each image, and where the phases were separated.

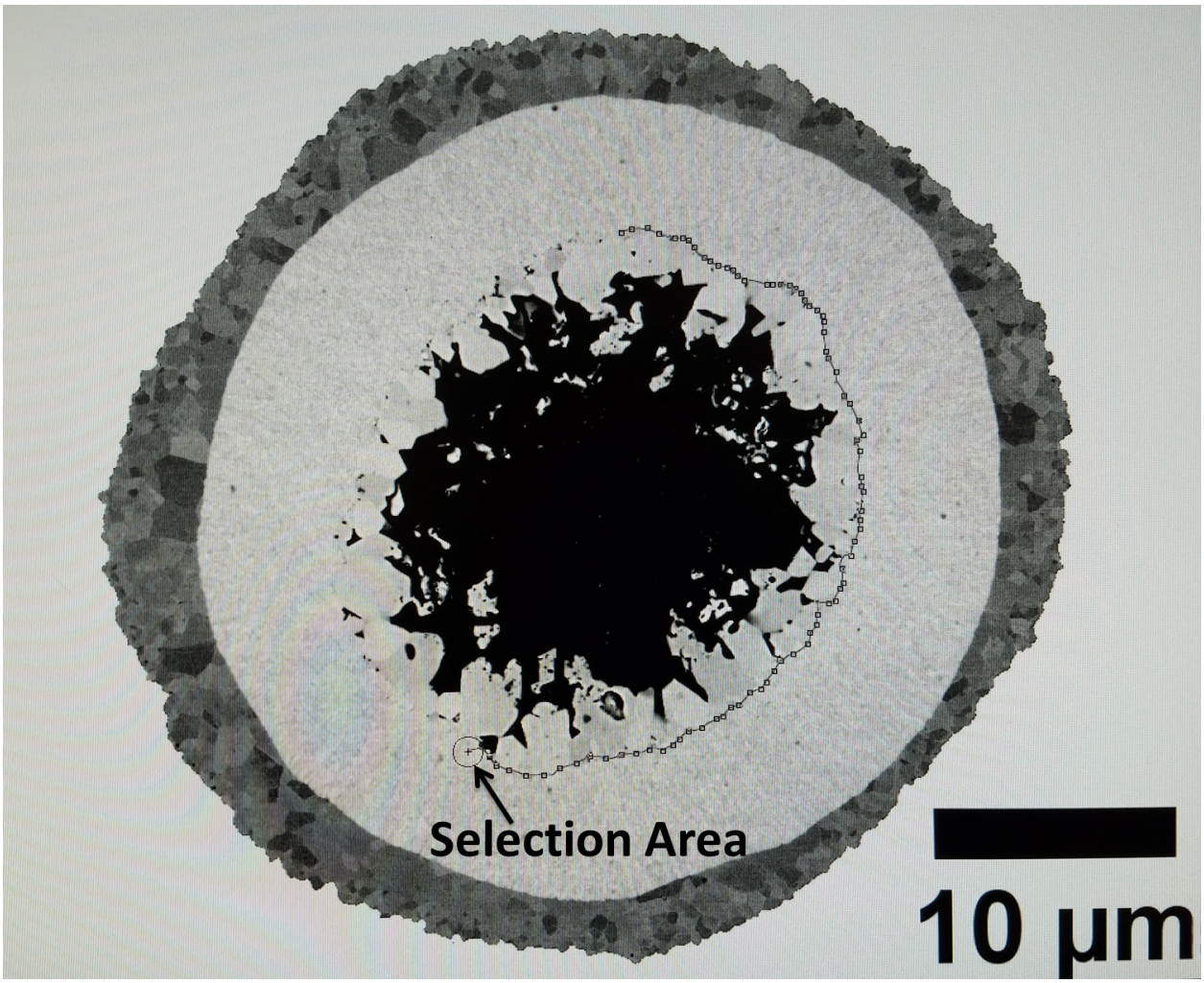

Figure 2.8: FESEM-BSE image of a polished cross-section with "levels" applied showing how the magnetic lasso tool in Photoshop can be used.

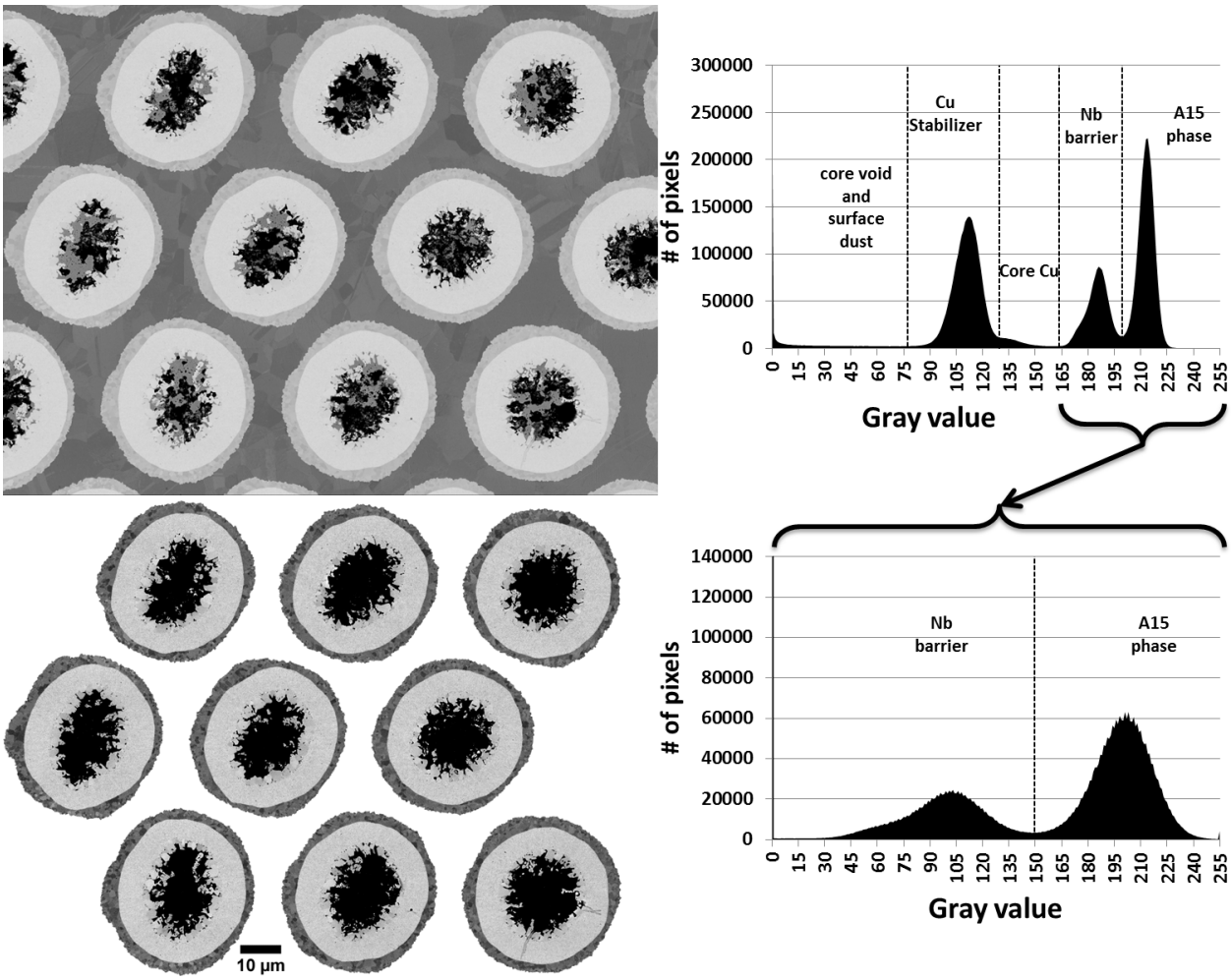

Figure 2.9: FESEM-BSE image of a polished cross-section (top left) and its histogram (top right). After removing the Cu layer, we take the remaining filaments (whose gray values span $\sim$ 165-230) and redistribute them over all 255 channels by using the levels function (shown in lower left). This provides more contrast to aide in the manual separation of the SG and LG A15 layers.

2.1.4 Color mapping images by a chosen variable

A useful tool for visual analysis of images is a color map which can represent data in a 3D color-space where the dimensions are lightness (L), green-red (a), and blue-yellow (b). These 3 variables allow for a mathematical model which can describe all perceivable colors. Here I will try to pull out the key points needed to understand why we have chosen a particular colormap. There are many additional resources available to expand on this abbreviated lesson, and they can be as specific as colormaps for scientific visualization [83], or more broadly for digital image processing [84].

Each unique colormap will have preselected values set in a look up table (LUT) which is used to map the variable of interest. Two popular colormaps are "jet" and "rainbow", jet is shown in the top of Figure 2.10 which is a wire cross-section colored by filament aspect ratio (the major diameter divided by the minor diameter). Jet is a type of colormap often described as hot-cold, or thermal maps where the sequence of colors runs from hot (red) to cold (blue). Jet was the default option for many years in common software suites such as Mathworks, Matlab, COMSOL, and ANSYS. However, Jet has numerous drawbacks compared to other colormaps. The most notable is that the lightness is about the same at either extreme of the colormap as shown in Figure 2.11 [85], so when jet is printed in grayscale as shown in the top right image of Figure 2.10, the highest and lowest values will both be dark. This can also create an artificially high contrast between values in the middle region, as shown between two filaments in the left side of the wire, circled in black. Jet is also not ideal for people who suffer from color blindness, and it may be difficult to distinguish the color gradient. In one study of cardiologists [86], it was found that while a bright color scheme like jet is preferred in their imaging software, doctors had less accurate diagnoses compared to other colormaps.

In the bottom of Figure 2.10, we have applied what we believe is the best choice of color scheme, called "viridis". Viridis is a perceptually uniform sequential colormap which means that the color and lightness is linear and has a monotonic gradient as shown in Figure 2.11. One benefit to this is that in grayscale the color range simply goes from light to dark over the entire range, rather than both ends appearing dark as in jet, making it easy to determine which are the highest or lowest values. This also reduces the artificial contrast in the mid-range, and the same two circled filaments

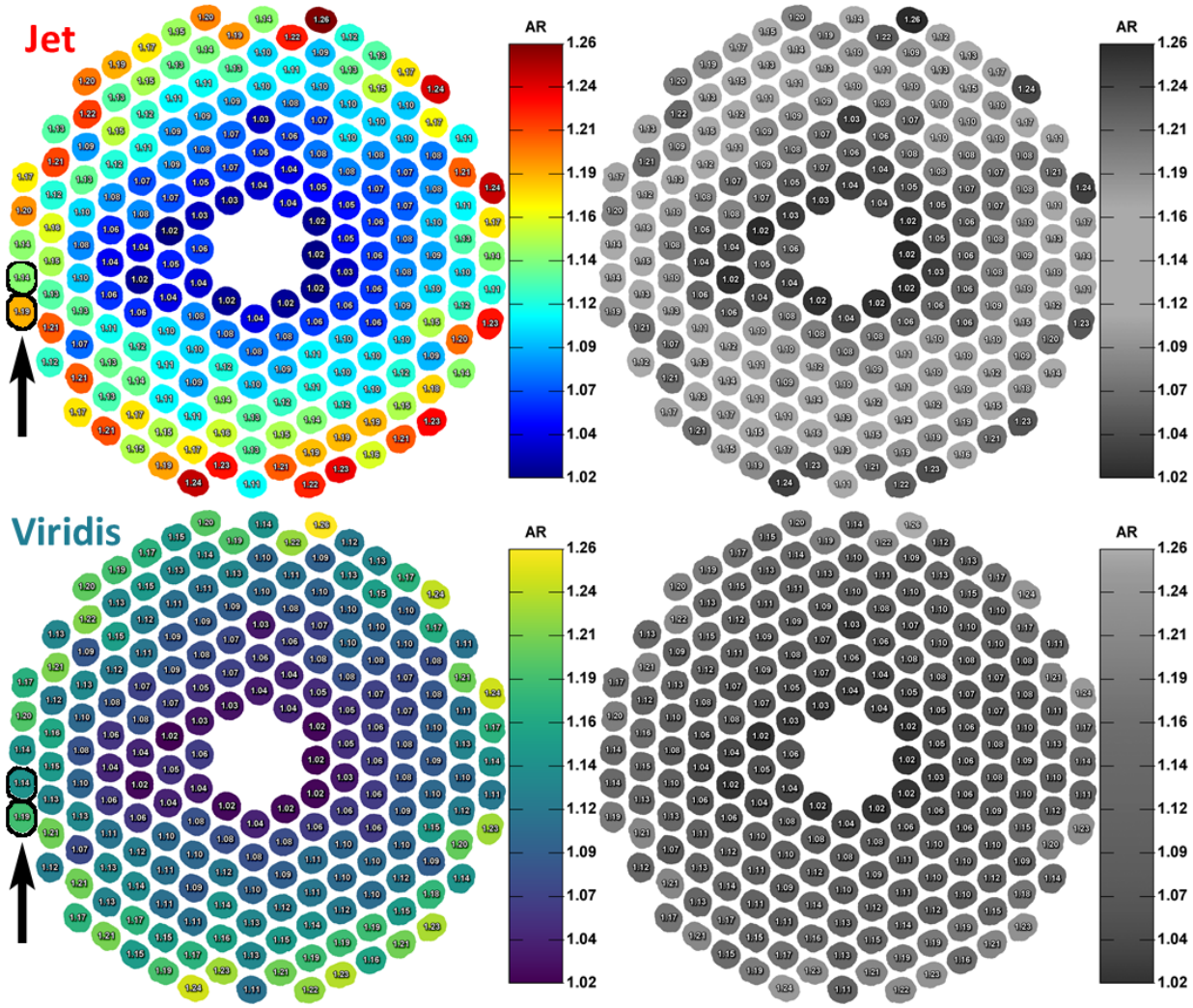

Figure 2.10: A comparison of the popular hot-cold colormap jet (top) and our preferred color map, viridis (bottom). Each cross-section was colored by aspect ratio of the filament on the left, and the gray-scale representation is shown on the right. While jet appears more colorful, it does not have a perceptually uniform gradient which is why its gray-scale image is dark on both ends of the distribution, rather than a continuous gradient as seen in viridis. This can also can give the appearance of more contrast than is appropriate in the mid-range, as demonstrated by the two circled filaments in the left side of both colormaps. Such a powerful method of data representation immediately reveals that the filaments in the outer rings are more aspected than those at the wire center.

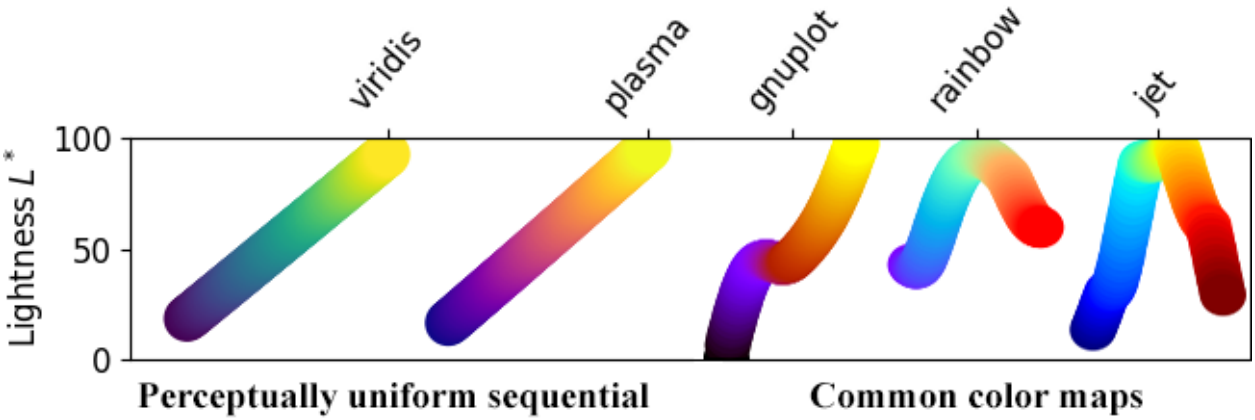

Figure 2.11: One of the three variables determined when making colormaps is the lightness, shown here for a handful of common colormaps. Viridis and plasma are both perceptually uniform and sequential, which allows gray-scale conversions to retain all of the information provided by the color contrast. Gnuplot has a small kink in the middle, making it a non-sequential profile which will lose information when converted to grayscale. The last two colormaps, jet and rainbow are divergent and also have different L values at the ends, reducing the effectiveness when printed in black and white, or comparing similar values in the mid-range. This graphic was reproduced from [85].

appear closer in color, as one might expect given their close aspect ratios. Additionally, viridis maps values from blue to yellow, with no red, making it more suitable for people with color-blindness.

In the original, un-altered image (Figure 2.3) it is noticeable that the inner ring filaments are quite circular while the outer ring filaments are more elliptical, however, the gradient between them is not that apparent until a color map is applied as in Figure 2.10. The FIJI software can rapidly measure the aspect ratio of each filament, and after assigning colors to each value, a radial dependence is clear. The raw data which generates the color map is discussed in chapter 4. The benefit of color maps over raw data is the effectiveness and speed of the impact when conveying the information to an audience. There is an excellent presentation on the practical difference between color schemes and why viridis is superior, available for free on YouTube [87].

2.2 Electrical property measurement techniques

The main consideration for this work is to drive critical current density (J_c) as high as possible, with the FCC goal at 1500 A/mm^2 at 16 T, 4.2 K [66]. This must be done while maintaining a residual resistance ratio (RRR) above 100 in the final cabled form, or above 150 in the pre-cabled

wire. The experimental configurations for measuring RRR and J_c are fundamentally the same, but the preparation is slightly different and is described in this section.

2.2.1 Residual resistivity ratio (RRR)

For RRR measurements, a Physical Property Measurement System (PPMS) by Quantum Design was used allowing for control of the cryostat to maintain desired temperature. The magnet system is a 9 T superconducting solenoid, however, the measurements were made in zero field. The native instruments in the PPMS are typically used on small samples and is current-limited to about 5 mA, but our short samples of superconducting wires may need up to 500 mA for a good signal to noise ratio. A set of external instruments and custom software were then used with a current-limit in the single amp range. The sample holder for the probe allows for approximately 1 cm sample length, with current taps on the ends, and voltage taps evenly spaced along the sample ~3 mm apart (Figure 2.12). The current and voltage taps were attached to the sample by a silver conducting epoxy.

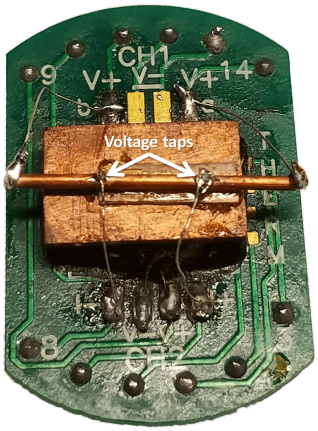

Figure 2.12: An example of how samples are prepared for RRR measurements using a standard 4-point technique.

Above T_c, the resistivity is mostly determined by the Cu resistivity, and the temperature dependence is linear at high temperatures as shown in the left side of Figure 2.13, typical for metals. At very low temperatures the resistivity follows the Bloch T^5 law (Equation 2.2.1) before dropping to zero in the case of superconductors, shown in the right side of Figure 2.13.

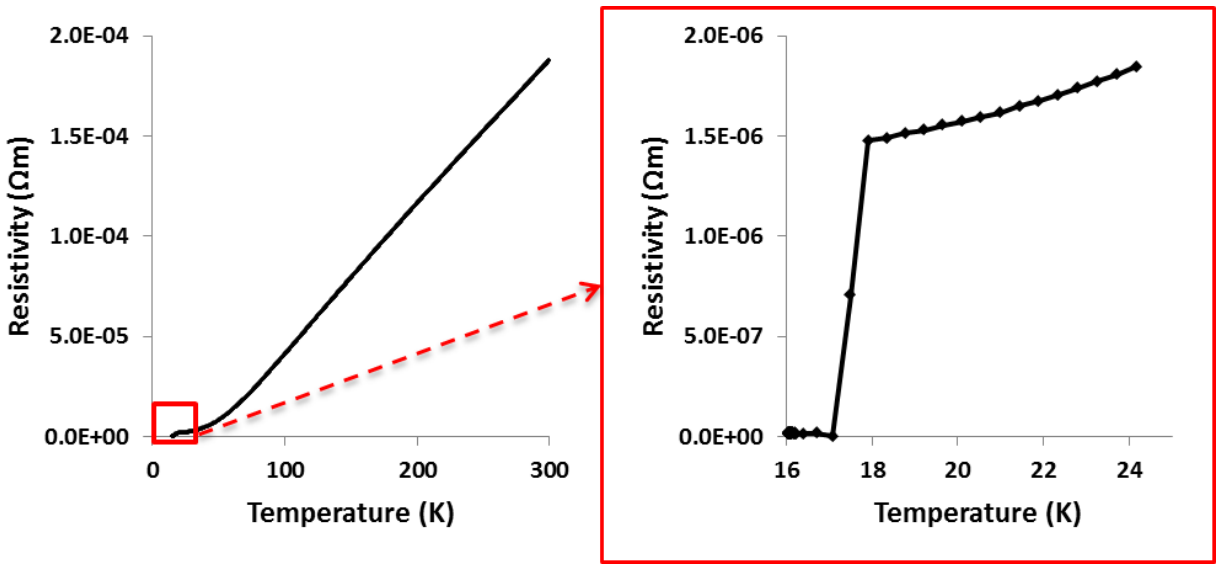

Figure 2.13: A plot of resistivity as a function of temperature. The behavior is linear until near T_c where the profile follows the Bloch T^5 law before dropping multiple orders of magnitude, signifying the superconducting transition. The T_c appears slightly lower than expected due to the fast cooling rate allowing the heater and temperature recorder to become slightly offset

$$\rho(T) = \rho_0 + AT^5 \tag{2.1}$$

Data was taken every 0.5 s from 300 K to 16 K (just below the T_c of Nb_3Sn). Since was not performing the measurement to determine T_c, a fast ramp rate was used which creates a slight delay between the temperature recorder and the heater, causing an apparent shift to the T_c.

$$RRR = \rho(300\ K)/\rho(19\ K)$$

2.2.2 Critical current (J_c)

For critical current measurements, we used a superconducting solenoid from Oxford instruments with a maximum field of 15 T, capable of providing transport currents up to 2,100 A, though the wires studied here typically have $I_c < 700$ A at 12 T. The preferred sample holder requires a sample length of 4-4.5 cm with about 0.5 cm of each end covered in solder to ensure good current transfer,

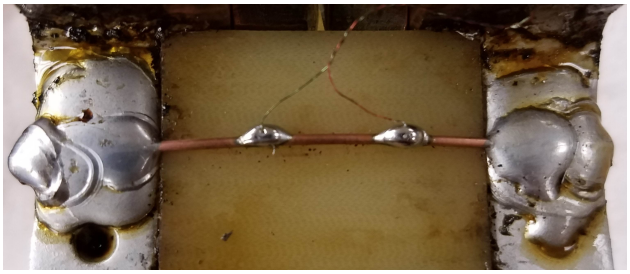

Figure 2.14: An example of how samples are prepared for I_c measurements using a standard 4-point technique.

and the voltage taps are spaced 1 cm apart in the center of the sample (Figure 2.14). Custom Labview software was used to control the magnet, current source, and record voltage response across the sample. This software has many useful features for both the measurements and for data processing.

For these relatively short samples, not all current is transferred to the superconducting filaments, and even very small currents running through the Cu will produce a small, but measurable offset (Figure 2.15). This provokes a background resistance and heating as a consequence. Once I_c is exceeded, even more heating occurs.

Our software can account for this offset in two ways, first by offering different measurement techniques, and then by applying a linear correction to the final data. The two different measurement options are a continuous measurement and a pulsed measurement. In both methods the user must set a maximum electric field criterion beyond which the current will shut off, and also the size of the current step as the current is increased. The smallest step possible of 0.5 A was used for all measurements, the electric field criterion varied from sample to sample but could be as high as 10 μV/cm in some cases where the sample has high resistivity. In the continuous measurement mode, the software applies an initial current, measures the electric field, then increments the current based on the step size chosen by the user (1 A for example). The current is increased in this step-wise manner until the electric field criterion is exceeded either due to a high resistance, or a superconducting transition occurs and I_c is exceeded.

The second measurement type is a pulsed mode, where the software applies a minimum current set by the user near I_c (i.e. 500 A), measures the voltage, and then turns the current off, allowing

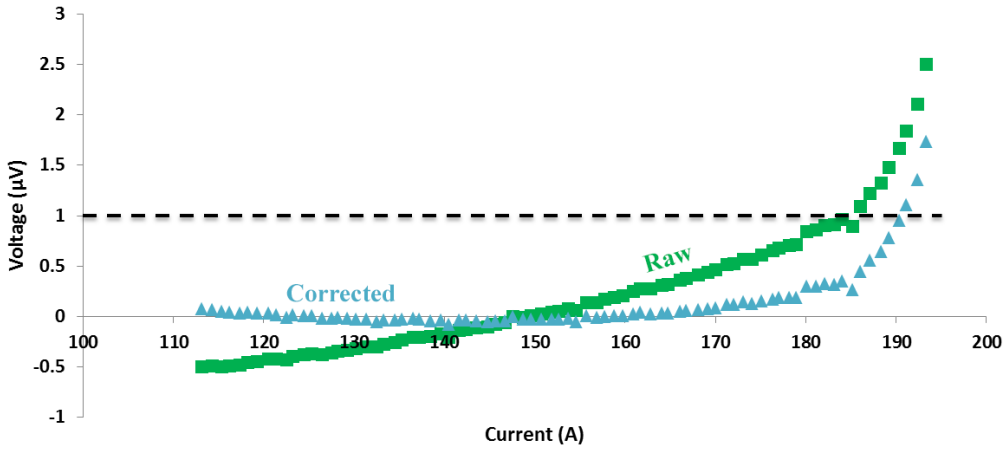

Figure 2.15: A typical I_c measurement taken at 15 T. The green squares are raw data which show some resistance in the wire, while the blue triangles are after a linear correction is made. I_c is determined with a 1 μV/cm criterion. The I_c is estimated to be 190 A in this data.

heat to dissipate. The measurement is then repeated with increased current based on the chosen step size until the voltage criterion is exceeded. This is useful for samples generating too much heat and producing a large background voltage. In either case, the software corrects the data for the resistive part of the curve so that a standard 1 μV/cm criterion can be utilized at the transition (Figure 2.15).

2.2.3 Local *RRR* and J_c measurements

In later sections we discuss the nature of Sn leaking out of filaments and reducing both local *RRR* of the Cu, and in some cases the J_c of leaking filaments. To determine the local impact of barrier breakthrough on *RRR*, a experiment to progressively etch the Cu was developed, measuring the *RRR* at each interval. After each *RRR* measurement, the silver epoxy used to make the voltage and current taps was removed and the sample immersed in a dilute nitric acid (HNO_3) bath for 5-10 minutes, partially removing the Cu matrix. The *RRR* was then measured again, repeating this etch and measurement process until only 4-5 inner rings of filaments remained; the results are shown in chapter 3.

The etch experiments to measure J_c variation between the inner ring filaments and the entire wire was a bit more complex, and only allowed for an initial measurement and one post-etch

measurement. For this experiment, the initial I_c is measured, and then the Cu matrix is etched away between the voltage taps from the original measurement until the filament pack is exposed as shown in Figure 2.16. The outer ring of filaments (ring seven) is then carefully removed, exposing filaments from ring six, and its surrounding Cu. I then etch away the interfilamentary Cu around the ring six filaments, repeating this until I have removed three to four rings of filaments, and finally measuring the critical current of the wire with the remaining inner ring filaments. Due to the hexagonal shape of the filament pack and the small size of the filaments, it is difficult to remove an exact, complete ring of filaments, and I instead aim to remove about half, leaving the inner rings 1-4 intact. To do this by only removing the Cu between the voltage taps requires either carefully etching with a dropper to slowly dissolve the small volume, or protecting the sample by a wax technique, allowing the wire to be fully immersed in the acid.

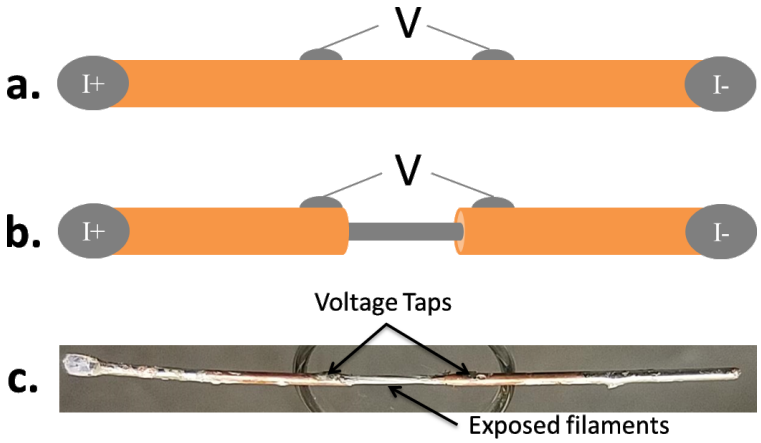

Figure 2.16: A schematic of how samples are prepared for I_c measurements before (a) and after (b) etching. In (c) the remaining center filaments are shown between the voltage taps.

The presence of the bundle barrier added more complexity to this type of experiment, and hydrofluoric acid needs to be used to etch the Nb bundle barrier away. This means we have to first dissolve the outermost Cu with HNO_3, then use HF on the bundle barrier, then switch back to HNO_3.

After I_c is measured, we destructively analyzed the wire to determine which filaments were intact for the transport measurement. To do this, the wire is cut just outside of the voltage taps and mounted in a puck for imaging. We serially polish the puck, taking images every 0.5-1 mm to see

which filaments were continuous along the whole length of wire during the transport measurement, and are also supported by Cu since I_c is affected by strain state [88].

2.3 Differential thermal analysis

To measure differences in phase evolution between different wires and/or HT's, we utilized Differential Thermal Analysis (DTA) alongside our microstructural analysis. The major benefits to the DTA are that data points are closer together in temperature, and the sample preparation time is substantially less compared to microstructural analysis in an SEM. The DTA machine features two arms, each holding a crucible as shown in the right most image of Figure 2.17. One of the crucibles will hold alumina powder as a reference, while the other will contain our sample of interest. Since the DTA has a weight limit, we maximize the signal by etching away the stabilizing Cu as shown in the left side of Figure 2.17, as it has no role in the A15 reaction. With both our sample and the reference in place, the heat treatment begins and the temperature of both the reference and the sample will increase. When a phase transformation occurs in our sample, the heating rate is perturbed as heat is absorbed or remitted in the transformation. The reference Al_2O_3 has no reactions in the temperature range of interest, allowing the temperature differential (ΔT) to signal the reactions occurring within the PIT filaments.

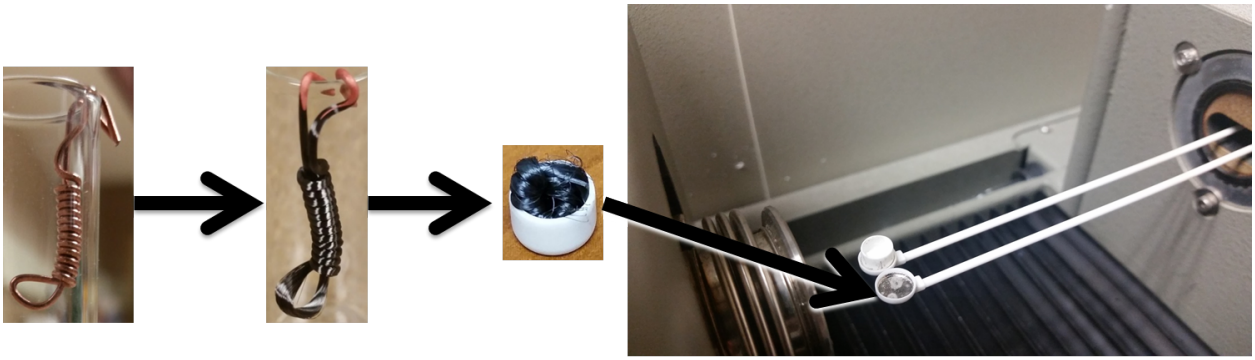

Figure 2.17: To prepare samples for the DTA, 15 cm of wire is first wound into a small coil. The stabilizing Cu is etched off in nitric acid with the wire ends kept out of the acid to ensure that the Cu sleeves within the core are not affected. The coil is then placed into a crucible inside the DTA furnace.

CHAPTER 3

REACTION PATHWAYS AND THEIR INFLUENCE ON THE MICROSTRUCTURE AND SUPERCONDUCTING PROPERTIES OF STANDARD NB_3SN PIT WIRES

Nb_3Sn PIT wires typically have an A15 reaction window from ~620-670 °C for up to 250 h. The effects of heat treatment temperature and time on the grain size, and therefore J_c, have been well known for some time. However, extensive studies on this reaction window have not been performed with the modern form of the PIT conductor since BEAS bought the PIT technology from SMI in 2006. We thoroughly explored the boundaries of this reaction box and beyond to determine if there were any relevant changes to the previous SMI PIT variant, and if we can control or suppress a Nb-Cu-Sn ternary phase called Nausite that appears to be detrimental to the SG A15 formation. During these studies we found that heat treatments as high as 690 °C could benefit some aspects of the microstructure, most notably a drastic improvement to the SG/LG A15 ratio. While I was successful in designing new heat treatments that formed more SG A15 and reduced the LG A15 volume, an increase in J_c did not materialize as the high temperature portion of the HT caused grain growth in the SG A15 layer, reducing grain boundary vortex pinning.

3.1 Phase evolution prior to A15 reaction

To study the phase evolution prior to the A15 reaction around 630 °C, a series of quench experiments were performed in which short samples of wire were removed from a reaction furnace at key times to better understand the temporal and thermal evolution of the microstructure. Wires were prepared by cutting 7 cm lengths, crimping the ends shut, and sealing in an evacuated quartz tube, in which a small amount of argon ($\sim$ 0.3 atm) was introduced to promote heat transfer. Multiple such samples were stacked in the furnace (Figure 3.1) and individually pulled out into an ice bath to freeze the microstructure at different points in the heat treatment. The wires were then mounted in a conductive puck and polished for imaging in an SEM.

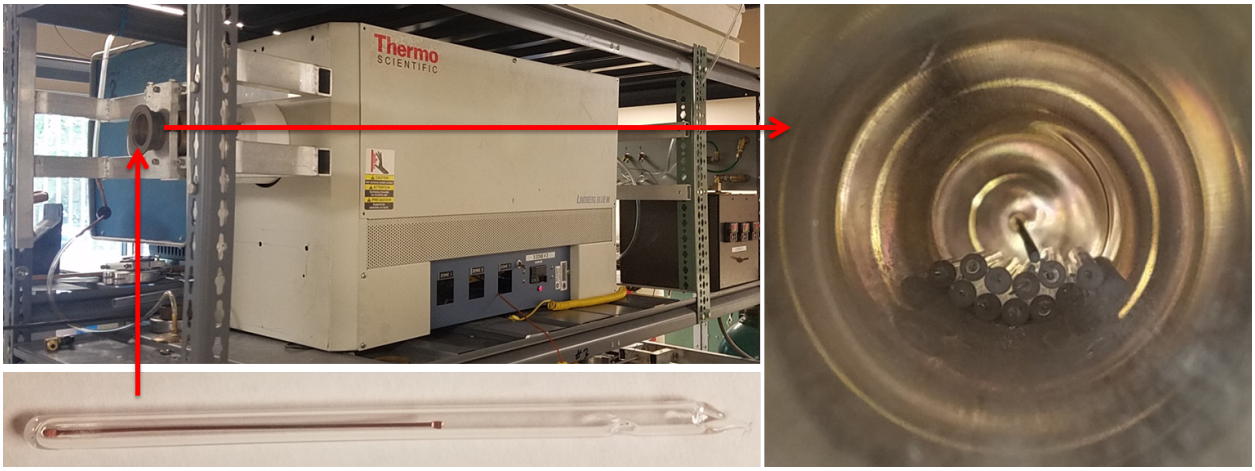

Figure 3.1: The bottom left image is of a wire with the ends crimped shut, and sealed in a quartz tube. Above is the three-zone reaction furnace where the tubes are loaded into for the phase evolution quench experiments. On the right is an example of multiple samples stacked into the furnace, the thermocouple can be seen just above the stack.

Digital imaging and analysis of the area fractions of each phase were performed as discussed in subsection 2.1.2. These data combined with knowledge of the phase diagrams shown in the following section, and the previous studies of the Nb-Cu-Sn system in these wires [70] allow quick identification of the Cu, Nb-7.5wt%Ta, the intermetallic phase known as Nausite ($(Nb_{0.75}Cu_{0.25})Sn_2$) and the various Nb-Sn phases: $Nb(Ta)_3Sn$, Nb_6Sn_5, and $NbSn_2$. The ternary Nb-Cu-Sn phase diagram in [89] was also considered, however it should be noted that the isothermal phase diagram is at 675 °C, well above the temperatures we are studying Nausite in these wires. In addition, we used a Differential Thermal Analysis (DTA) technique to more accurately define the temperatures where phase transitions occur as described in section 2.3).

My main focus was to fully characterize how the Sn-rich core supplied Sn to the Nb-Ta tube, and to determine how intermediate phases formed and decomposed from room temperature through the final isothermal A15 reaction above ~600 °C. In subsection 3.1.3 I will show that the detrimental LG A15 forms as a final decomposition of Nb_6Sn_5 which has the Nb-Cu-Sn intermetallic precursor of Nausite ($(Nb_{0.75}Cu_{0.25})Sn_2$).

3.1.1 Phase analysis by SEM

In the unreacted state each filament consists of a Cu-clad Nb7.5wt%Ta tube which acts both as the Nb source for A15 formation and as a diffusion barrier at the end of the reaction to prevent Sn from leaking out into the pure Cu (Figure 1.7). Though many different wires were investigated in this work, the majority of heat treatment experiments used a 0.78 mm diameter wire whose filaments are ~39 μm in diameter after reaction. These filaments are made of a round Nb7.5wt%Ta tube whose wall thickness is about 8.5 μm in the unreacted state. On the inner surface of the tube is a thin Cu sleeve (<1 μm thick), with the remaining central volume filled by a Sn-rich powder mixture, largely consisting of $NbSn_2$. This composite is then clad in a hex-shaped Cu can with a round central hole that forms most of the Cu stabilizer matrix, the rest of the Cu stabilizer being added by placing the entire multi-filament bundle in a surrounding Cu tube. According to the manufacturer, the preferred Sn content of the powder is 85-90 mass% [90]. As $NbSn_2$ is only ~72wt%Sn, roughly 71% of the powder mixture needs to be pure elemental Sn to reach 85 mass%. Our EDS results also show up to 3at% Cu in the powder, as well as some solid Nb pieces which are likely the remnant of incomplete $NbSn_2$ formation when the powder was formed. A benefit of the PIT process is that the core contents can be easily changed by altering the ratios of the powders without significant redesign of the wire [71]. While $NbSn_2$ powders have typically been the preferred Sn source [90, 91], other Sn sources may be used such as Cu_5Sn_4 powder [92, 93], MnSn2 [50], or Nb_6Sn_5 [94].

As the wires are reacted, we turn to the phase diagrams for Cu-Sn [95] and Nb-Sn [96] in Figure 3.2 to determine which phases are thermodynamically stable upon heating. For these HT's we used a ramp rate of 100 °C/h. As the heat treatment begins, Sn is rapidly absorbed into the Cu sleeve and for a short time, three Cu-Sn phases can be seen together (Figure 3.3), following the phase diagram in order of Sn content: alpha (α) Cu sleeve next to the Nb-Ta tube wall, some small pockets of epsilon (ϵ) just inside the α layer, and then the most Sn rich eta (η) phase closest to the Sn-core. The Cu sleeve transforms into mostly η phase at about 260 °C. As heating continues, the η converts to ϵ by 408 °C with any remaining η phase potentially melting. As no evidence of melting has been observed, I assume the $\eta \rightarrow \epsilon$ transformation is a solid state transformation in PIT wires. In addition to the described Cu-Sn phase formation, there is a ternary Sn-Nb-Cu phase which forms, commonly referred to as Nausite ($(Nb_{0.75}Cu_{0.25})Sn_2$) [97]. In a special heat treatment,

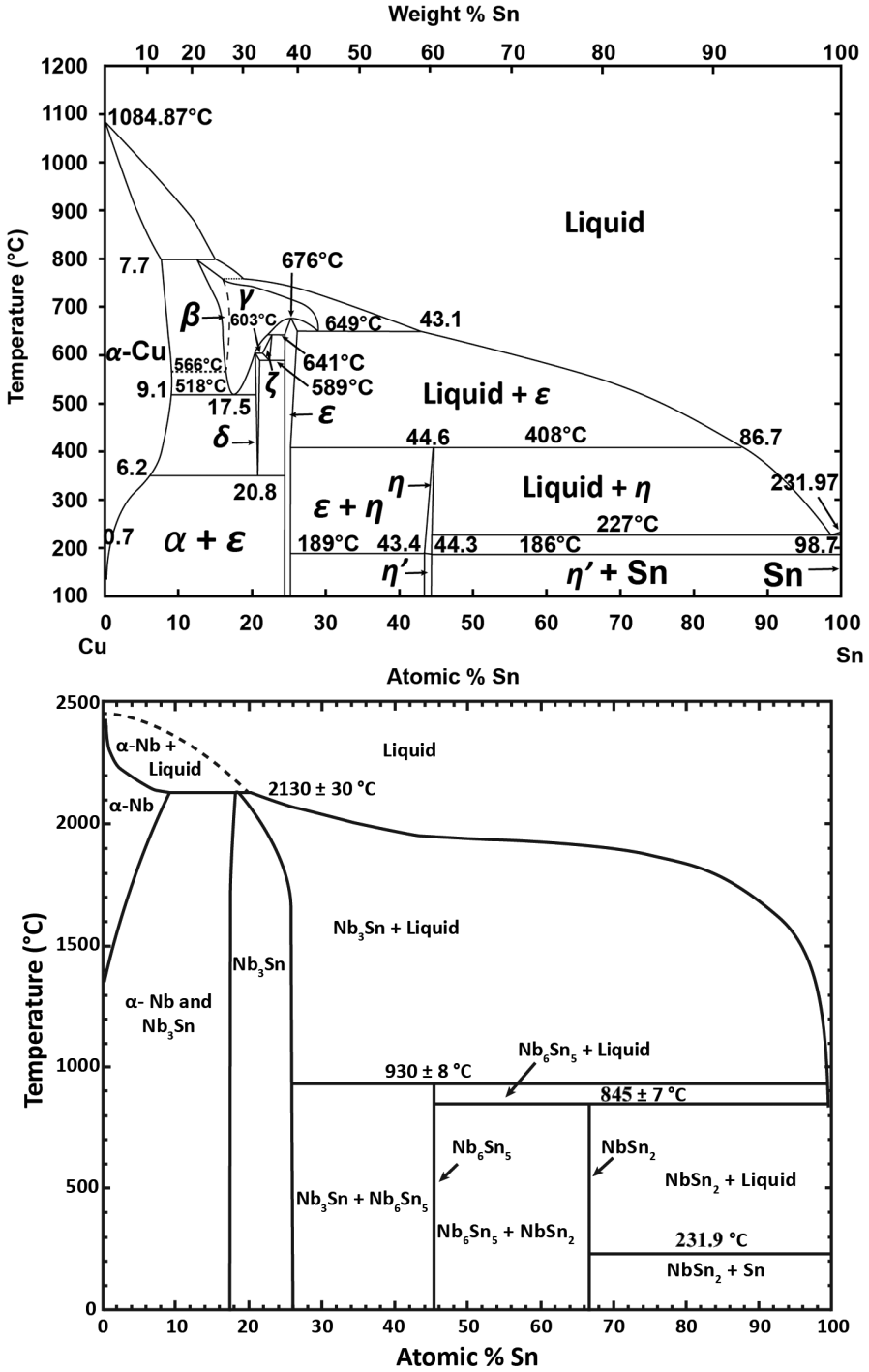

Figure 3.2: On the top is the Cu-Sn phase diagram, η decomposes at 408 °C, transforming to ϵ phase containing ∼25at%Sn. Below is the Nb-Sn phase diagram. Nb_3Sn has a range of composition from 18 to 27at%Sn, and the most Sn rich A15 produces the best wire properties.

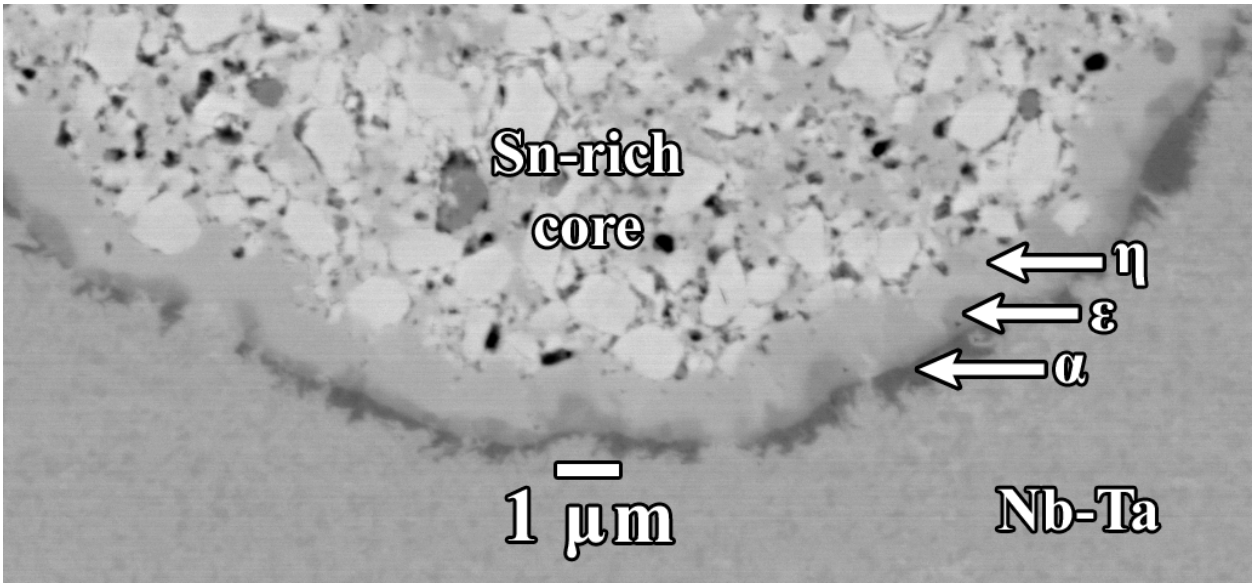

Figure 3.3: FESEM-BSE images of a polished, transverse cross-section in a sample quenched from the furnace at 225 °C. The decreasing Sn gradient from the core to the Nb-Ta tube is noticeable by the increasing quantity of Sn-rich Cu phases near the core.

we found Nausite could begin forming as low as 200 °C after a 48 h isothermal hold (Figure 3.4). While there have been previous studies which reported finding Nausite [98], this intermetallic has only recently received its own thorough examination [99], where they report finding a hexagonal $NiMg_2$ crystal structure with composition $(Nb_{0.75}Cu_{0.25})Sn_2$. They assume a partial substitution of Cu for the Nb in $NbSn_2$ which provokes a structural transformation from the $CuMg_2$ structure of $NbSn_2$, to the $NiMg_2$ for $(Nb_{0.75}Cu_{0.25})Sn_2$.

Above 408 °C, both the Nausite and ϵ phase grow in thickness until about 560 °C when the Nausite begins decomposing (Figure 3.5). Considering the chemical composition of Nausite, it is helpful to think of Nausite as $NbSn_2$ where 25% of the Nb has been replaced by Cu. Due to the low solubility of Cu in $NbSn_2$ (<0.4at%) [89], as Nausite decomposes back into $NbSn_2$, it rapidly ejects most of the Cu. The reappearance of the $NbSn_2$, originally present in the powder core, is rather short lived, and at ~630 °C it transforms to Nb_6Sn_5 in less than an hour, containing up to 5at%Cu as estimated by my EDS results (Figure 3.6).

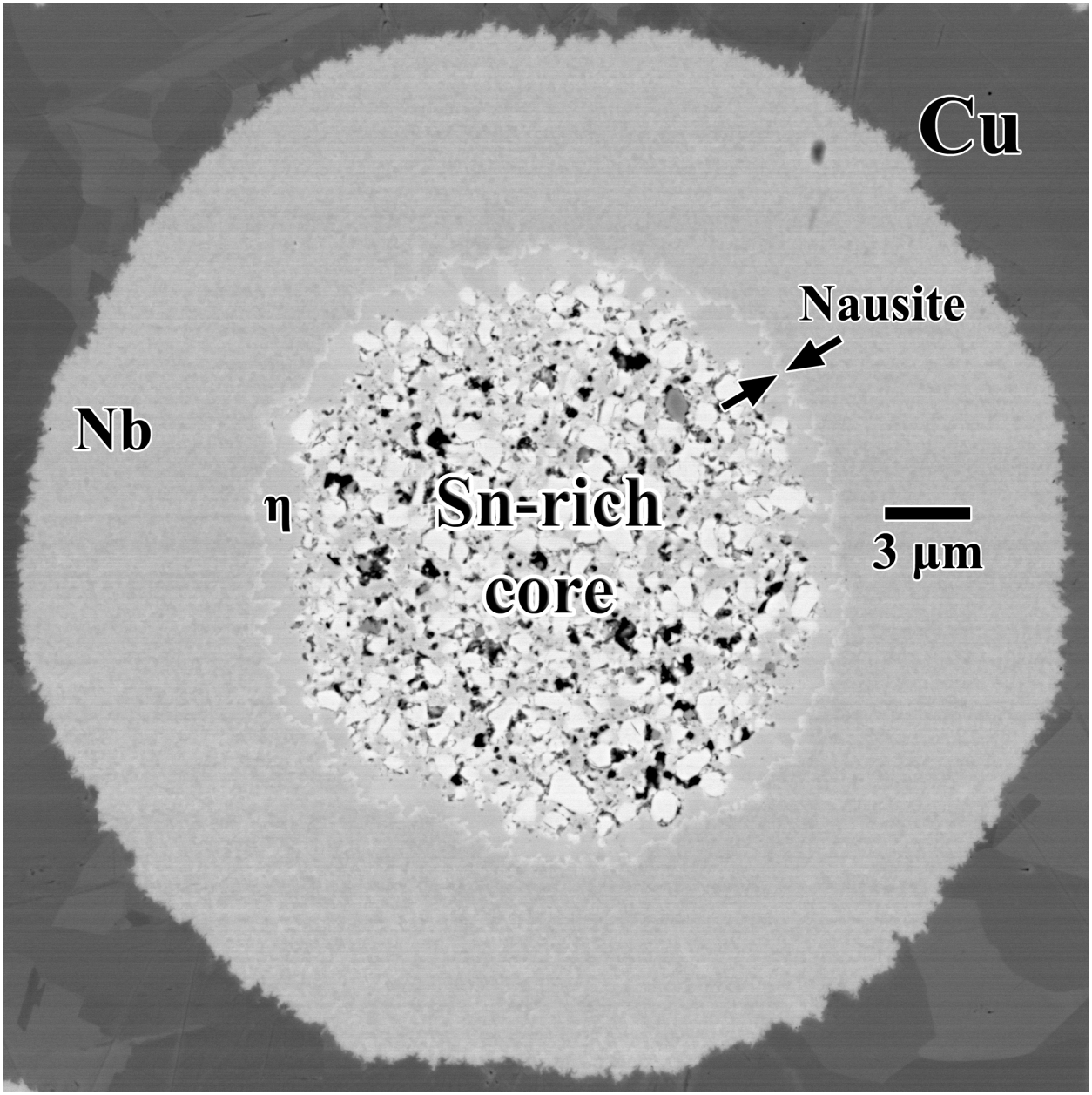

Figure 3.4: FESEM-BSE image of polished, transverse cross-section in a sample quenched from the furnace at 205 °C after an isothermal hold for 48 h. There is a light ring of Nausite separating the η phase at the edge of the core from the Nb-Ta tube.

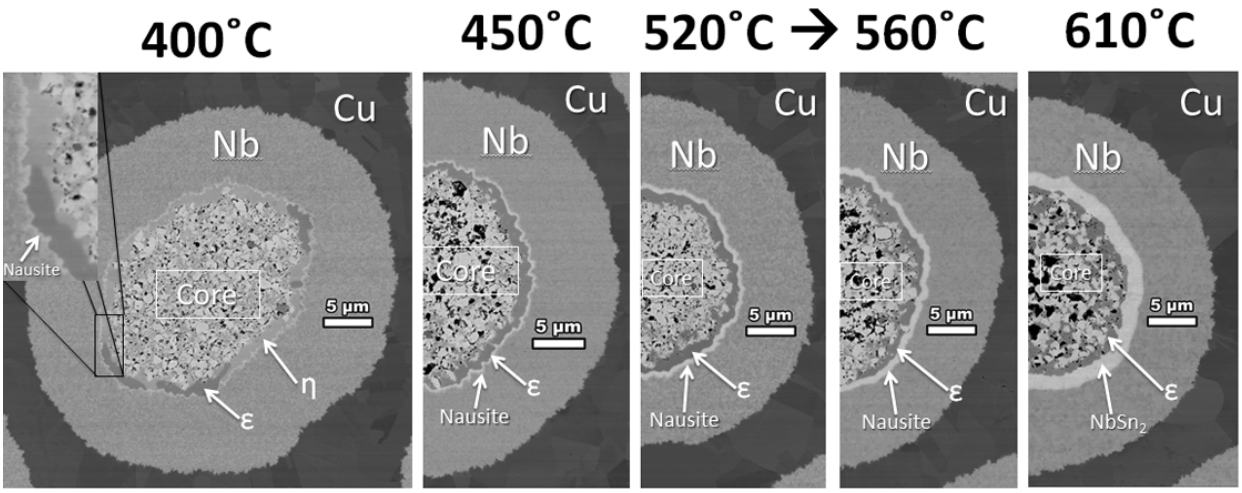

Figure 3.5: FESEM-BSE images of polished, transverse cross-sections of samples quenched from the furnace to show phase evolution up to 610 °C. A thin, light ring of Nausite has formed on heating to 400 °C which continues to grow until about 610 °C when it decomposes into $NbSn_2$. The Cu-Sn phases have a transformation from η to ϵ at 408 °C, after which we only see ϵ until the reaction is nearly complete.

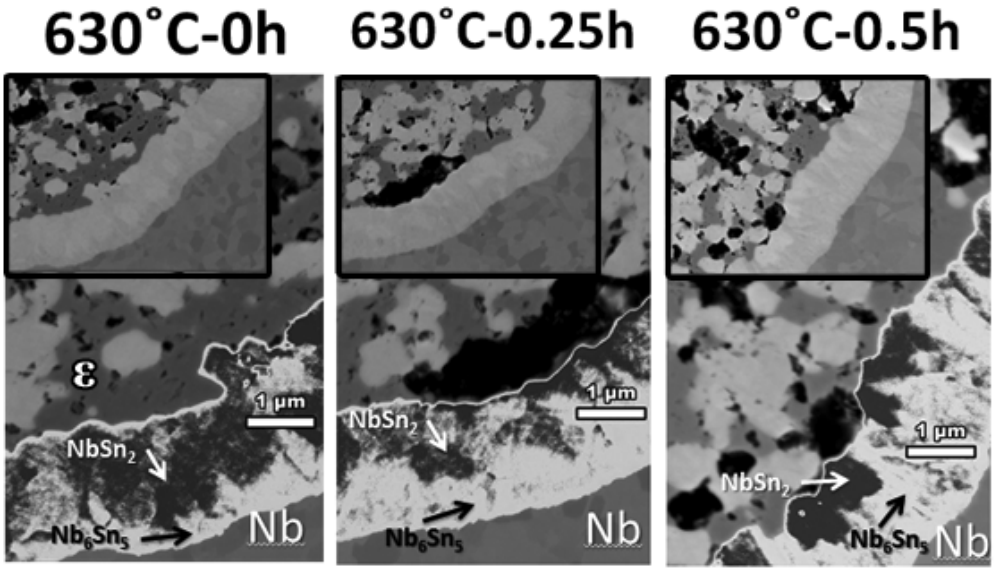

Figure 3.6: FESEM-BSE images of polished, transverse cross-sections of samples quenched from the furnace at 630 °C reacted for less than 1 h. The original images are inset while the principal image areas have been slightly magnified and contrast enhanced to better separate phases while the $NbSn_2$ rapidly decomposed into Nb_6Sn_5. The dark phase in the core is ϵ (Cu_3Sn).

3.1.2 Differential Thermal Analysis (DTA) of phase evolution on heating

The results of the DTA provide additional information to the microstructural analysis. For example, we know from the phase diagram that η phase transforms to ϵ at 408 °C, however, the DTA shows a two step transformation (Figure 3.7). To interpret the data, it should be noted that a negative ΔT is indicative of an endothermic reaction in which heat is absorbed (as in a melt), while a positive change indicates an exothermic reaction in which heat is released (as in a solidification). The changes in temperature given by the DTA are small enough that the raw data only reveals very fast transformations with a large volume. However, taking the derivative with respect to temperature can make transformations more apparent, as is shown on the secondary y-axis in Figure 3.7. The transformation of η to ϵ at 408 °C is clear, however, there is an additional transformation shortly after around 430 °C while the DTA shows no event in the 450-560 °C range, however, multiple events are seen between 560 °C and 610 °C as the Nausite decomposes into $NbSn_2$. The $NbSn_2$ is short lived and the entire layer rapidly transforms to Nb_6Sn_5 upon further heating (Figure 3.7).

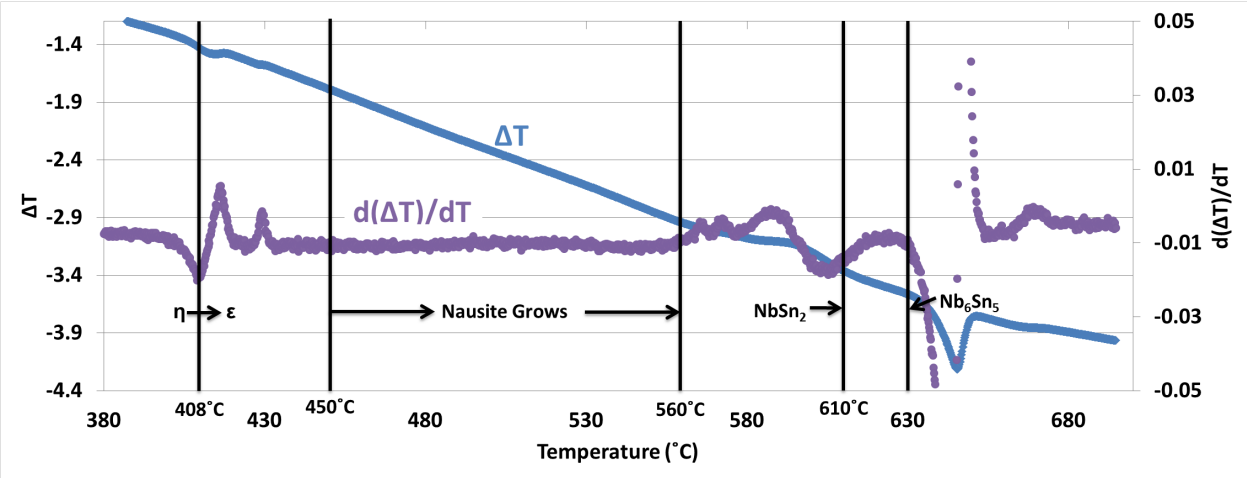

Figure 3.7: DTA data reveals additional details than by microstructure alone, specifically transformations with more than one decomposition step or those which occur quickly and may be difficult to observe by quenching wires from a furnace. For example, the furnace pull-outs showed Nausite at 560 °C and $NbSn_2$ by 610 °C, but the DTA shows that this transformation has multiple components. This data was obtained with a ramp rate of 100 °C/h to 690 °C. The top curve (blue) is the raw data (ΔT), while the lower curve (purple) is the derivative of the blue curve with respect to temperature (d(Δ)T/dT)

From a practical perspective, a major advantage of the DTA is that it takes much less time (∼2 work-hours) than microstructural analysis, which takes tens of work-hours to prepare samples for imaging and analysis. In addition, the microstructural analysis requires a sample to be heat treated and removed from the furnace at each point of interest, and then individually analyzed. The DTA, however, provides data on how phases are evolving every second, filling in the gaps between the samples examined by microstructure to ensure transformations were not missed. A good example is how the microstructural analysis shows Nausite at 560 °C and a complete transformation into $NbSn_2$ at 610 °C, but the type of transformation is not known. However, the DTA shows that the Nausite undergoes two small exothermic transformations just after 560 °C, followed by a large endothermic transformation into $NbSn_2$ at 610 °C. This feedback can guide future furnace pull-out experiments by revealing the appropriate temperatures to pull samples to show different stages of the microstructure.

Based on the results of this DTA experiment, Bruker EAS (BEAS) tried to suppress the multi-step decomposition of the Nausite into $NbSn_2$ by using isothermal holds below 550 °C, though it was not clear why this temperature was selected, or why the multi-step decompositions should be suppressed. They also used a slightly different technique called Differential Scanning Calorimetry (DSC) which measures the energy required to keep both the reference and the sample at the same temperature, whereas the DTA measures the difference in temperature between the sample and the reference when both are put under the same heating conditions.

Their first HT attempt performed by BEAS added an isothermal hold at 510 °C for 6 h (commonly written here as 510/6) as shown in Figure 3.8, with no effect on subsequent transformations. At the increased temperature of 550 °C for 1 h, the transformation around 630 °C was suppressed, showing no change to the Nb_6Sn_5 peak at 650 °C. Increasing this 550 °C isothermal hold to 6 h finally suppressed the rapid transformations leading up to the Nb_6Sn_5 signal, suppressing the reappearance of some $NbSn_2$. This 550/6 hold decreased the Nb_6Sn_5 signal by about 20%. However, Bruker reported that J_c(12 T, 4.2 K) remained unchanged when adding these additional isothermal holds. These 'shots in the dark' as they may be, suggests that suppressing the reappearance of the $NbSn_2$ may not be useful. Efforts may be better spent trying to reduce the volume of the precursor phase, Nausite as it was shown to beneficially help in RRP type conductors [54].

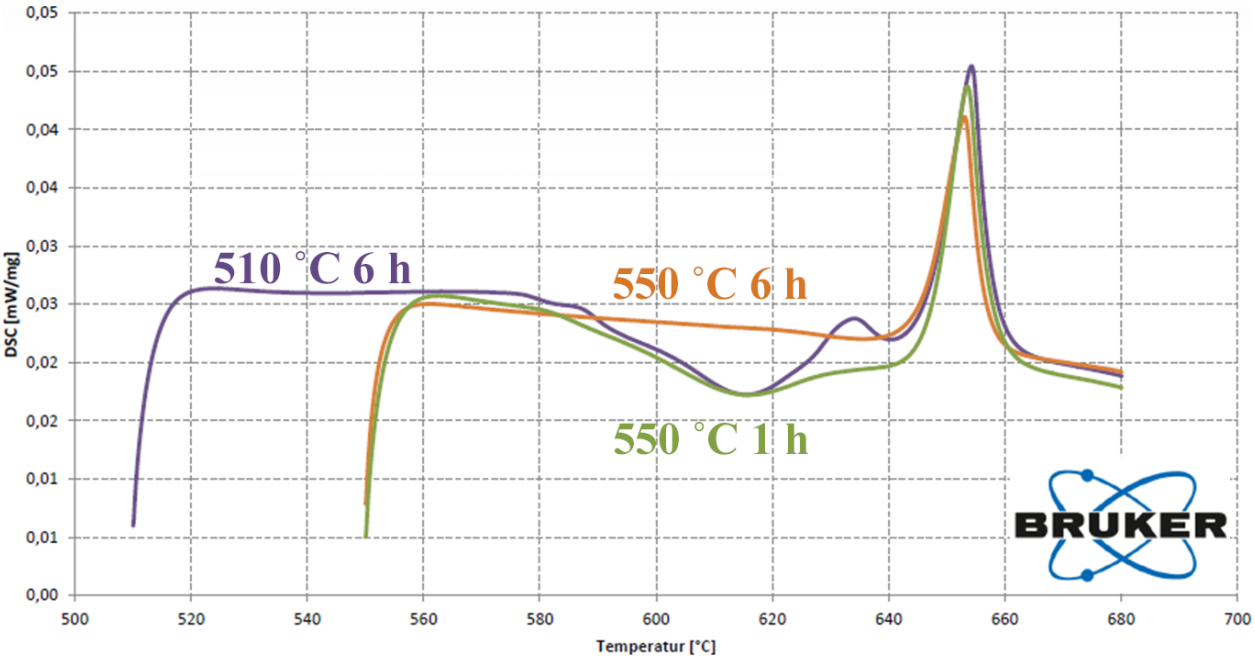

Figure 3.8: DSC results of Bruker EAS attempting to suppress the multi-step decomposition of Nausite into $NbSn_2$ above 560 °C. A ramp rate of 300 °C/h was used for this DSC measurement, this will shift the temperatures of the reaction slightly higher compared to our DTA measurement at 100 °C/h shown in Figure 3.7. The Nausite decomposed around 580 °C, the $NbSn_2$ formed by 610 °C, and the $NbSn_2$ rapidly transformed into Nb_6Sn_5 around 655 °C. The hold at 510 °C for 6 h showed an additional signal at 635 °C, however the specific transformation is difficult to know without additional microstructural image analysis. The 6 h hold at 550 °C did suppress all transformations between the Nausite decomposing and the Nb_6Sn_5 formation, skipping the $NbSn_2$ phase. However this was not found to have an effect on J_c.

3.1.3 Discussion of the phase transformations occurring before the desired A15 reaction

From our observations, the undesired LG A15 forms largely as a decomposition product of the Nb_6Sn_5 layer. However, this layer originates as a decomposition product of the $NbSn_2$ and the Nausite that precedes it.

To determine if a novel optimization in the low temperature range could help reduce the quantity of Nausite, we tried isothermal holds at 250 °C for 192 h, 350 °C for 168 h and 550 °C for 100 h, pulling samples out during each isothermal hold. We found that the 250 °C hold allowed for the η annulus in the core to transform to the less Sn-rich ϵ over 192 h (Figure 3.9). In this 250 °C

isothermal hold, the Nausite seems to stop growing once the η layer has transformed to ϵ. The 350/168 HT was an attempt to speed up this $\eta \rightarrow \epsilon$ conversion process, and while this did allow more η to convert to ϵ phase, the Nausite layer is about 300 nm thick everywhere, regardless of which phase it borders (Figure 3.10). Based on the DSC experiment performed at BEAS, we did a 550 °C hold too, however this served only to grow the Nausite layer.

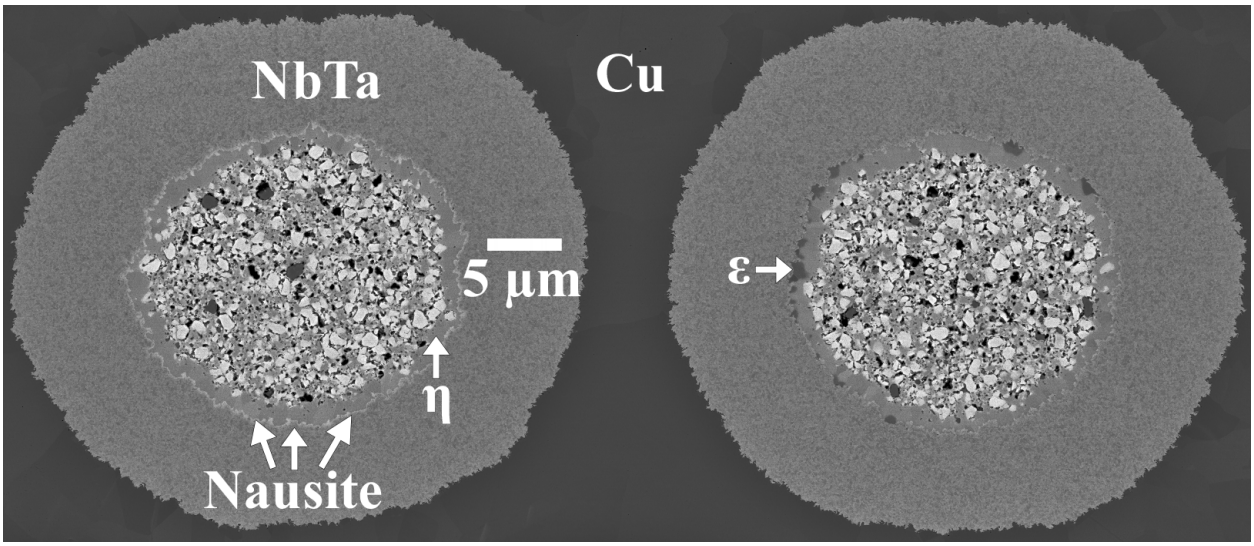

Figure 3.9: Contrast enhanced FESEM-BSE images of a sample quenched from the furnace showing phase formation after a 192 h hold at 250 °C in two neighboring filaments. On the left, the entire original α sleeve has transformed to η phase, and a thin ring of Nausite has formed between the η and the Nb-Ta tube along the entire perimeter. The right filament has regions where the η has transformed into ϵ phase, and there is very little Nausite bordering the ϵ phase.

Furthermore, we compared the Nb-Sn layer early in the A15 reaction between a two stage HT (350/168 + 630/4.5) and an isothermal HT (630/5). The Nb-Sn layer consists of Nb_6Sn_5 and Nb_3Sn, for both HT's. The layer areas are nearly identical after accounting for the 30 minute difference in A15 reaction time.

After these failed attempts to suppress formation of the Nausite, we concluded that Nausite will grow at any temperature above 200 °C, with isothermal holds appearing to have no effect other than to grow the layer slightly more compared to heat treatments with no isothermal hold ramp, ramping directly to the A15 isothermal reaction temperature. Provided the chemistry is unchanged in the core of these BEAS wires, there appears to be a thermodynamic end state which

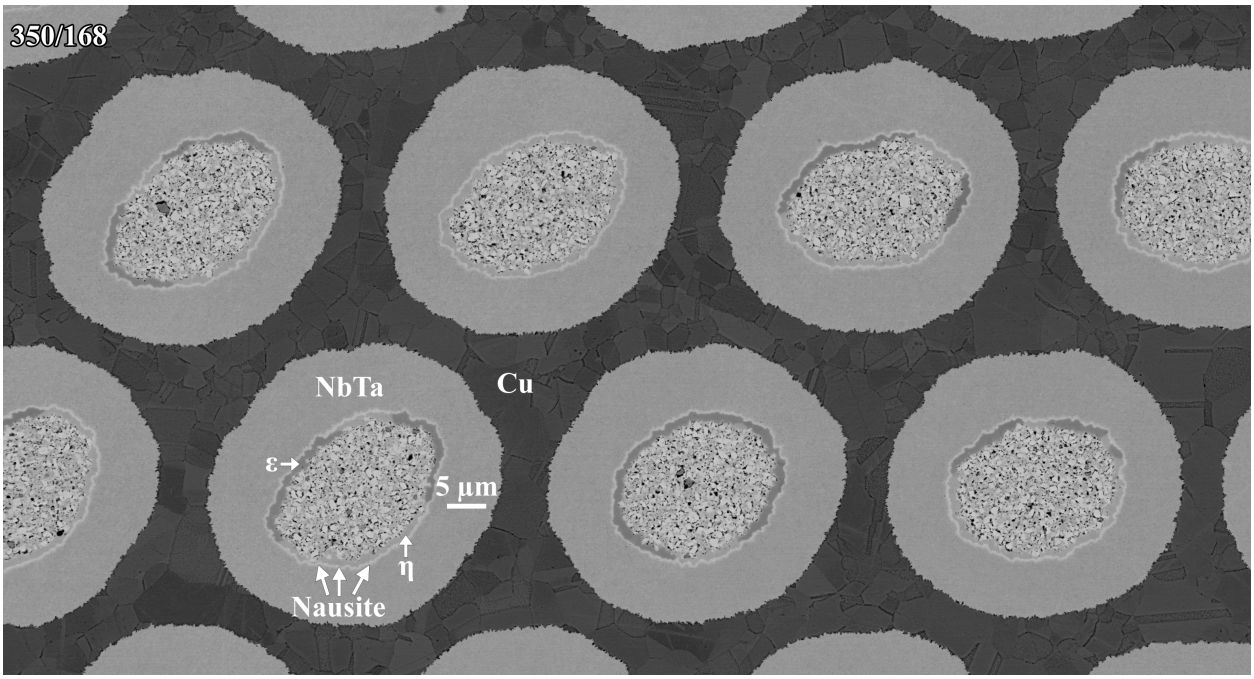

Figure 3.10: FESEM-BSE image of a wire quenched from the furnace showing phase formation after a 168 h hold at 350 °C. A significant amount of the η phase has turned into ϵ and a Nausite ring separates the Sn-rich core and its $\eta + \epsilon$ sheath from the Nb-Ta tube in all filaments.

is path independent for PIT Nb_3Sn, and any energy that is added into the system below the Nausite decomposition temperature of ∼560 °C will allow more Nausite to form. The best HT would then be one which ramps to the desired isothermal temperature as quickly as practical to minimize growth of the Nausite layer. It could be possible to suppress this thermodynamically unavoidable Nausite phase by adding Cu or Sn to the core, and such a possibility is discussed in chapter 5.

3.1.4 Summary of reactions occurring during temperature ramp up before isothermal A15 reaction

1. The initial Sn-rich powder diffuses Sn into the Cu sleeve, forming the intermetallic Nausite as early as 200 °C.

   - $$NbSn_2 + Cu \rightarrow (Nb_{0.75}Cu_{0.25})Sn_2$$

2. The Nausite grows until about 610 °C before rapidly decomposing back into $NbSn_2$, ejecting its Cu

   - $$(Nb_{0.75}Cu_{0.25})Sn_2 \rightarrow NbSn_2 + Cu_x$$

3. Around 630 °C the $NbSn_2$ and expelled Cu rapidly transform to Nb_6Sn_5 which can contain up to 5at% Cu. This transformation also creates free Sn in the system. The transformation is nearly complete after only ∼30 minutes into the isothermal hold at 630 °C.

   - $$NbSn_2 + Cu_x \rightarrow Nb_6Sn_5Cu_x + Sn$$

4. During the early hours of the heat treatment (1-15 h), the free Sn diffuses from the core into the Nb-Ta tube to form SG A15. This A15 formation is discussed in the following section.

3.2 A15 reaction from 600-690 °C

A15 has been found to form at temperatures as low as 600 °C in Nb_3Sn PIT conductors. However, the growth rate is very low compared to HT above 630 °C, making it impractical to study the A15 formation over the entire HT as it may take up to a month for a full reaction. Instead, we first looked at the A15 formation at 630 °C to understand how both the A15 and Nb_6Sn_5 phases evolve throughout the HT.

3.2.1 A15 formation in the early hours of heat treatment at 630 °C

After a 100 °C/h ramp to the isothermal reaction temperature at 630 °C, the dominant phase present is a thick layer of Nb_6Sn_5 which inscribes the Nb-Ta tube. This Nb_6Sn_5 has a columnar grain structure, whose long axis points radially outward from the core to the Nb-Ta tube. Various microstructures during the isothermal HT at 630 °C are shown in Figure 3.11. A thin layer of SG A15 is seena fter 5 h, and after 10 hours the SG A15 layer has grown to ∼0.5 μm. Only two hours

later the SG A15 layer thickness has increased to 0.85 μm, and LG A15 has now begun to appear. In these Nb_3Sn PIT wires, the LG A15 always forms at the interface between the Nb_6Sn_5 and the growing SG A15 layer. In addition, the LG A15 is always marked by Cu precipitates at the LG A15 boundaries. As the heat treatment progresses, both the SG A15 and the LG A15 layers grow, and after about 94 h the Nb_6Sn_5 has disappeared. At this stage, the remaining SG A15 that forms out of the Nb-Ta will have a Sn source of the Cu-Sn phases ϵ and α left in the core. Once the Nb_6Sn_5 is gone and there are only Cu-Sn phases left to drive the reaction, the LG A15 layer is nearly complete, and the SG A15 formation begins to slow down. By ~240 h at 630 °C there is no longer enough Sn to drive any A15 formation, and the reaction is functionally complete. The final A15 volume fractions for this heat treatment are 40.7% SG A15 and 14.4% LG A15, providing a SG/LG A15 ratio of 2.8. Previously, we have analyzed the SG/LG ratio of 10 PIT wires differing by both HT and billet design, and found that the total A15 volume fraction varies only slightly from 55-58% in fully reacted samples [49], with the SG/LG ratio varying from 2.4-3.0. We conclude that BEAS makes a well-defined and controlled wire.

3.2.2 Typical phase & morphology volume fractions of a reacted filament

This standard Nb_3Sn PIT formula forms rather similar A15 microstructures for HT's in the temperature range from 620-670 °C. After an optimized HT in this temperature range (620/100+640/90 for this wire), we typically observe about 40% SG A15, 13% LG A15, 23% residual DB, and 24% remnant core, which includes 3% core A15, and the remaining 21% is comprised of voids and residual Cu-Sn phases as shown in Figure 3.12 (all % refer to the non-Cu cross-section). An important metric for the quality of the A15 layer is the SG A15/LG A15 ratio, since our goal is to maximize the SG A15. This optimized heat treatment has a SG A15/LG A15 ratio of 3.0.

The 1 mm and 0.85 mm wires presented in this dissertation were given to us by CERN and the samples were already reacted under various heat treatments. We analyzed a billet of 0.85 mm wire with six different heat treatments, two 1 mm billets with two different heat treatments, as well as our own two heat treatments on the 0.78 mm wire. This analysis was performed to quantify the fractions of residual Nb-Ta barrier, SG A15, LG A15, core A15, and remnant core for each wire and heat treatment, as is summarized in Table 3.1. Figure 3.13 contrasts filament images from the least and most reacted samples. At the lower temperature HT of 630/100 we see a large amount of remnant DB (35%) and isolated A15 in the core (5%), and a total A15 fraction of only 46.4%. The

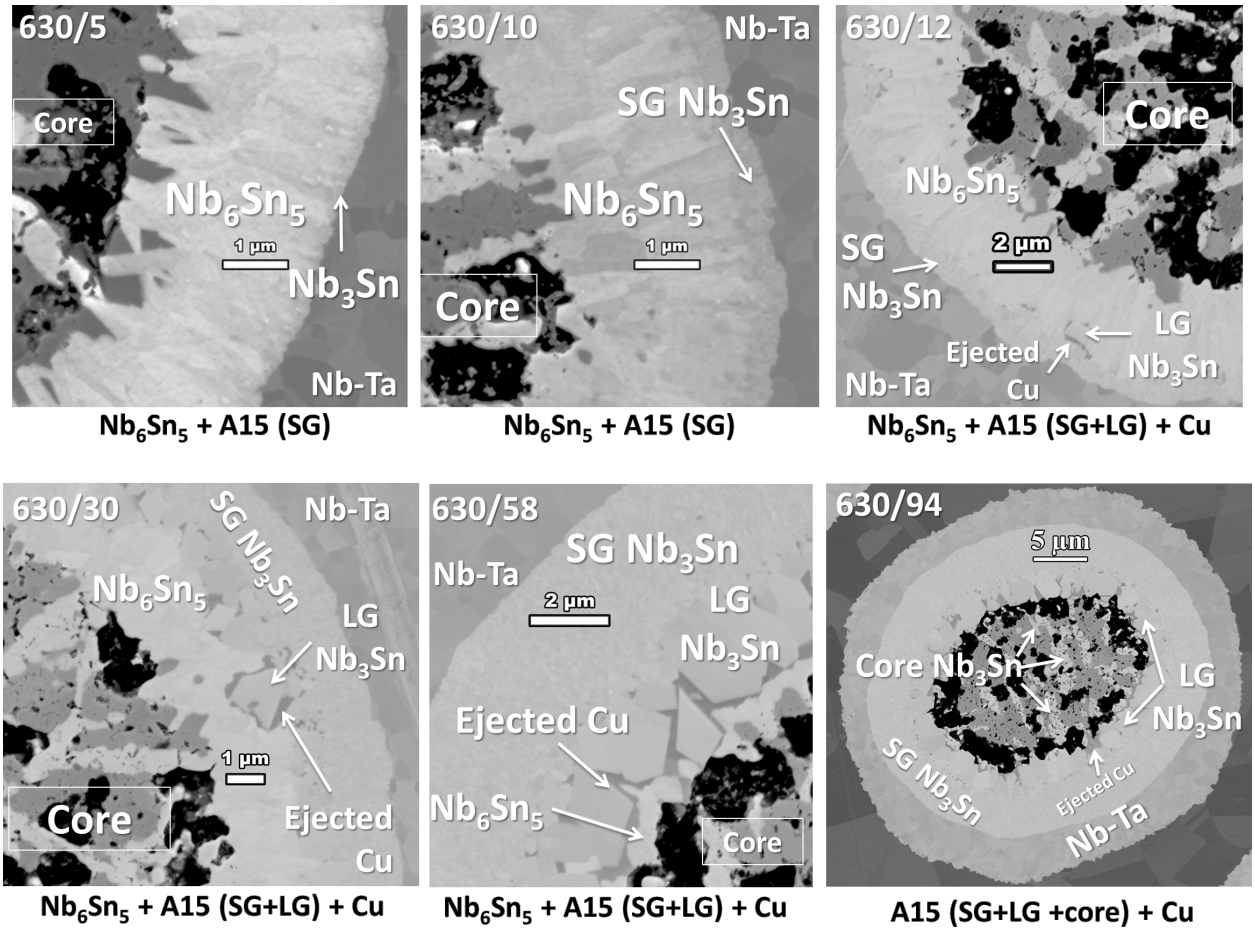

Figure 3.11: FESEM-BSE images of polished, transverse cross-sections of samples quenched from the furnace showing A15 phase growth at 630 °C at various times. The SG A15 layer steadily grows with increasing time and the LG A15 appears after the initial SG A15 growth, in this case 12 h at 630 °C. By 58 hours, most of the Nb_6Sn_5 is gone, and we have continuous layers of SG A15, LG A15, and Cu phases which separates the Nb_6Sn_5 from direct contact with the SG A15 layer. At 94 h, the Nb_6Sn_5 is gone, leaving behind the SG And LG A15 layers, core A15, Cu-Sn phases, and voids.

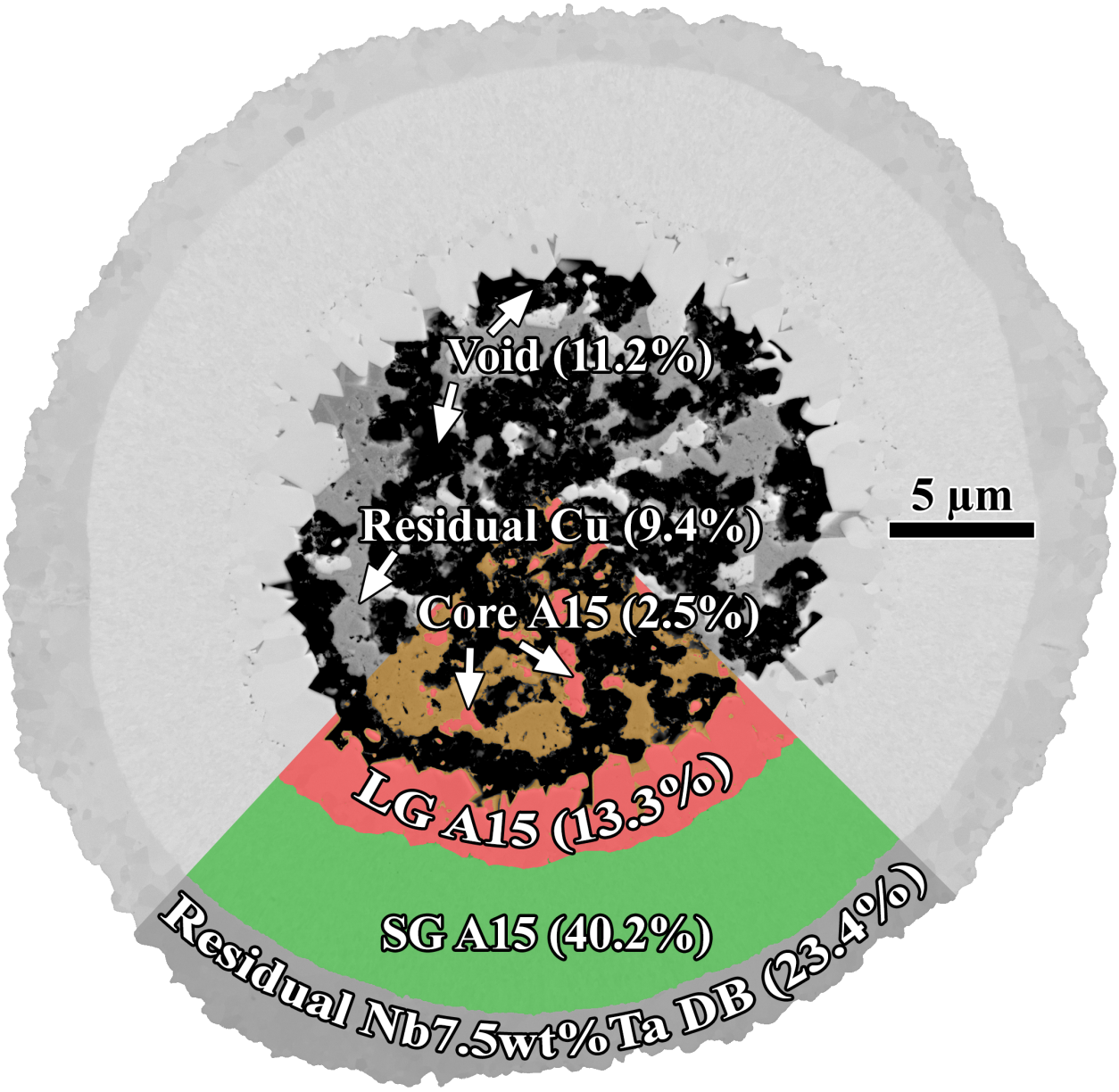

Figure 3.12: FESEM-BSE image of a polished, transverse cross-section of a filament in a 0.78 mm diameter Bruker PIT wire reacted with heat treatment 620/100 + 640/90. The cross-section is partially colored to distinguish between phases and morphologies. Nb-Ta is colored in gray, SG A15 in green, LG A15 and core A15 in red, and Cu in orange.

higher temperature HT at 670/100 shows the core nearly depleted of A15, less residual DB (22%), and total A15 fraction of 59.4%.

Table 3.1: The two 1 mm wires have CERN sample ID's of He10S11403A01.U.006 for the HT of 620+640 °C and He10S11403A01.U.011 for the 625 °C. The 0.85 mm are from BEAS billet B29992, and the 0.78 mm wire is from billet B31284. All reported dimensions were measured on reacted wires.

HT temperature (°C)	HT time (h)	Wire diameter (mm)	Filament diameter (μm)	Phase or morphology volume %						SG/LG A15 ratio
				DB	A15 total	core	A15 core	A15 LG	A15 SG	
620+640	120+120	1.0	50	23.0%	57.9%	19.1%	3.0%	14.2%	40.7%	2.9
625	280	1.0	50	23.6%	57.7%	18.7%	3.5%	14.5%	39.7%	2.7
630	100	0.85	42	34.5%	46.4%	19.1%	5.1%	13.3%	28.0%	2.1
630	200	0.85	42	24.9%	55.4%	19.7%	3.0%	14.5%	37.9%	2.6
650	50	0.85	42	32.8%	48.3%	18.9%	2.8%	15.4%	30.1%	2.0
650	100	0.85	42	24.6%	57.2%	18.2%	1.3%	16.4%	39.5%	2.4
670	50	0.85	42	24.4%	57.0%	18.6%	1.0%	13.7%	42.3%	3.1
670	100	0.85	42	22.2%	59.4%	18.4%	0.6%	15.2%	43.6%	2.9
620+640	100+90	0.78	39	23.4%	56.0%	20.6%	2.5%	13.3%	40.2%	2.8
630	240	0.78	39	22.7%	58.1%	19.2%	3.0%	14.4%	40.7%	2.8
unreacted	0	0.78		68%	-	32%	-	-	-	

The average LG A15 volume fraction is ∼15% and, while slightly higher for the 650/100 and 670/100 HT, the amount varies little between heat treatments probably because the LG A15 forms by the same Nausite→Nb_6Sn_5→Nb_3Sn decomposition reaction. This Sn-rich reaction pathway with increasing temperature is then [100, 101]:

$$NbSn_2 + Cu \rightarrow (Nb_{0.75}Cu_{0.25})Sn_2 \rightarrow NbSn_2 + Cu_x \rightarrow Nb_6Sn_5Cu_x \rightarrow Nb_3Sn(LG) + Cu_x + Sn \tag{3.1}$$

The free Sn then diffuses into the Nb-Ta tube to form SG A15.

The residual core volume fraction is 18 to 20% after reaction and is composed of α and ϵ Cu-Sn phases and voids, with up to an additional 5% disconnected A15. However, there is a clear

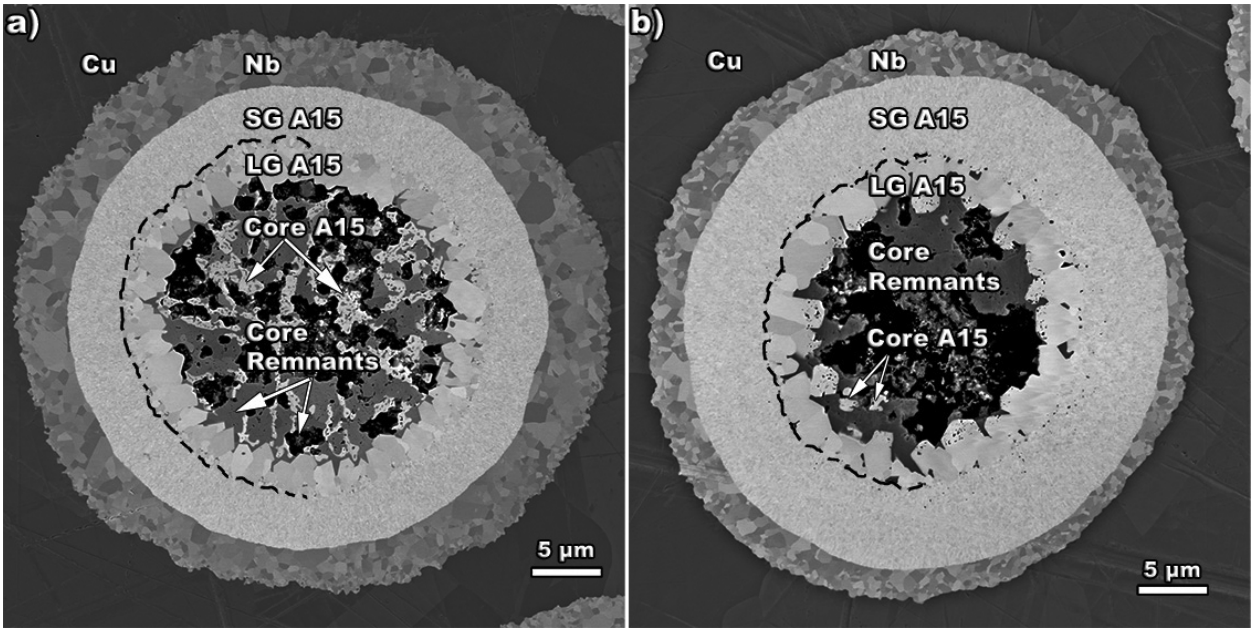

Figure 3.13: FESEM-BSE images of polished, transverse cross-sections of minimally distorted inner ring filaments of the 0.85 mm wire for the two extreme HTs studied: (a) 630 °C for 100 h and (b) 670 °C for 100 h. Images have had the contrast enhanced to better distinguishes the small and large grain A15 layers. A dashed line has been added at the left side of each image to better illustrate the interface between the two A15 regions. The 630/100 sample is under reacted with a very thick Nb-Ta DB remaining, while in the 670/100 HT the DB is much thinner in the lower right, susceptible to leaking.

trend that higher reaction temperatures decrease the amount of A15 in the core with only 0.6% after 670/100. The SG A15 varies from 28 to 44%, and as the diffusion barrier is consumed to produce SG A15, its volume fraction decreases from 35 to as little as 22%. The LG A15 only varies from 13.3-15.2%, this is because the LG A15 is essentially fully formed when the Nb_6Sn5 is gone, typically about halfway through any optimized HT, further explaining this narrow window of LG A15 volume fractions across all heat treatments.

3.2.3 Variation of LG A15 formation with reaction temperature early in the heat treatment

A vintage PIT sample made by SMI some 20 years ago shown in Figure 3.14 reveals that the ratio of SG/LG A15 does depend on the heat treatment temperature early in the reaction when LG A15 is just starting to form. Consequently we performed a study on the phase morphology ratios

as a function of temperature early in the HT, performing single stage HT's which all ramped up at 100 °C/h to an isothermal reaction temperature of either 630, 650, 670, or 690 °C for a time between 50-250 h, performing many furnace pull-outs in the first 20 hours of each heat treatment. For this experiment we obtained about 50 m of conductor at 0.78 mm wire diameter through the LARP collaboration. The focus of this series of heat treatments was to observe the early development of A15 growth during each isothermal heat treatment and determine if there is a temperature dependence on the volume of SG A15 which forms before the LG A15 appears.

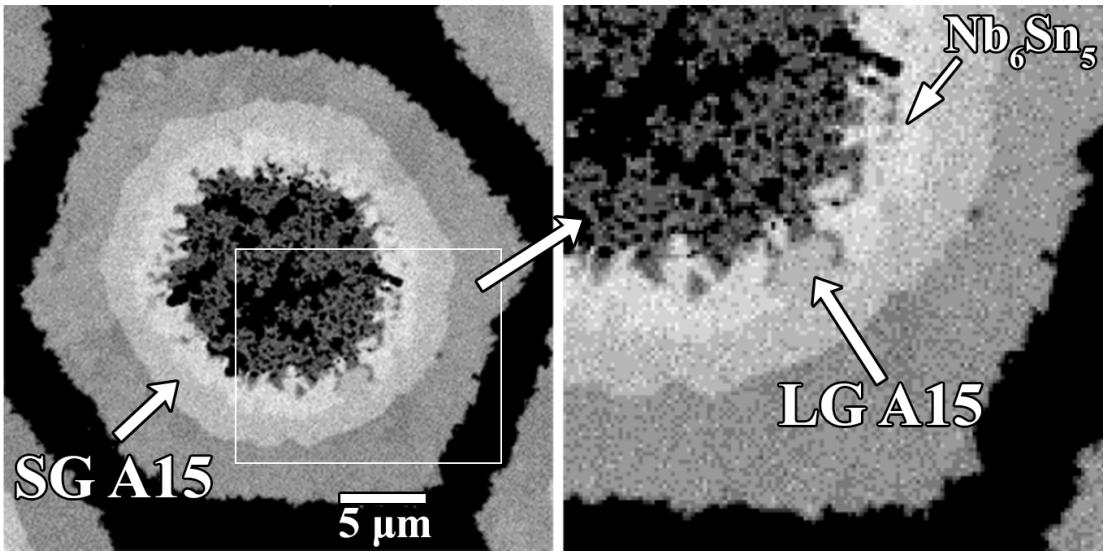

Figure 3.14: Micrographs of LG A15 nucleation after 4 h at 670 °C in a Nb_3Sn PIT wire made ∼20 years ago by SMI. Images from the thesis of Hawes [102],

In all cases, the SG A15 formed first, with the LG A15 forming later in the reaction; higher temperatures forming LG A15 more rapidly than lower reaction temperatures. From our quench experiment at 630 °C, we found that the LG A15 started forming around 12 h, with a SG A15 layer thickness of 0.85 μm. At 650 °C the SG A15 layer was 1.5 μm thick and the LG A15 first precipitates out after 8.3 h. At 670 °C the LG A15 begins forming after only 5 h, and the SG A15 layer formed is 2 μm thick. At 690 °C the SG A15 layer thickness is only 1.6 μm with LG A15 forming in less than two hours (Figure 3.15). If we take this data and try to create an isothermal transformation diagram for A15 morphology, we see a clear boundary in temperature-time space for LG formation (Figure 3.16).

This isothermal transformation diagram incited us to develop a new type of multi-temperature A15 reaction in which we start with a brief high temperature excursion to grow a thick SG A15 layer, then drop the temperature to minimize LG A15 formation. The results of these experiments are discussed later in this chapter.

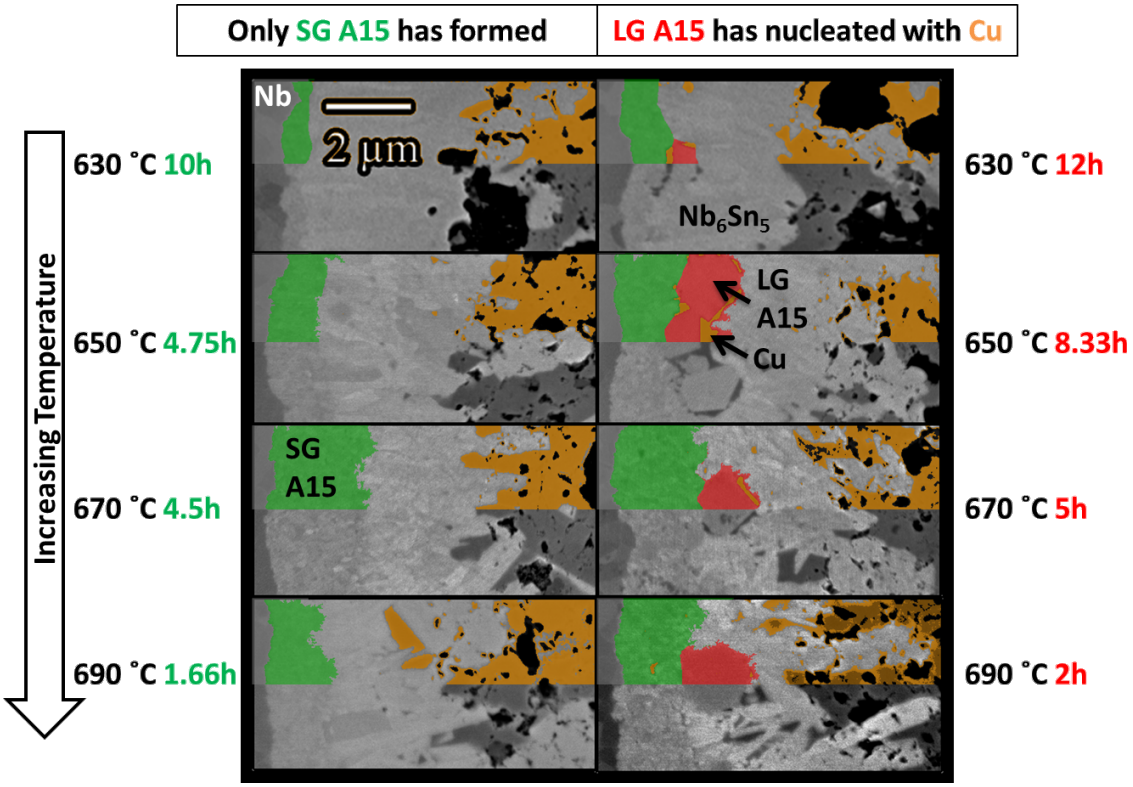

Figure 3.15: Micrographs of the LG A15 nucleation. From top to bottom the reaction temperature increases from 630 to 650, 670, and 690 °C. The left column shows images of SG A15 before LG A15 formation (less than 1% of the filament cross section). The right column is after LG A15 has formed. Half of each panel is colored to distinguish between phases and the two A15 morphologies. Considering a panel from the right column, from left to right, we see: Nb-Ta DB (gray), SG A15 (green), LG A15 (red), and Cu (orange). The Nb_6Sn_5 is uncolored and voids are black.

A high critical current density (J_c) demands a thick layer of small grains of A15 with strong vortex pinning, as well as a remnant diffusion barrier to prevent Sn from leaking into the stabilizing Cu and lowering *RRR*, worsening magnet stability. High J_c is typically obtained by reacting as much of the Nb-Ta barrier as possible to form the most SG A15, requiring higher temperatures or

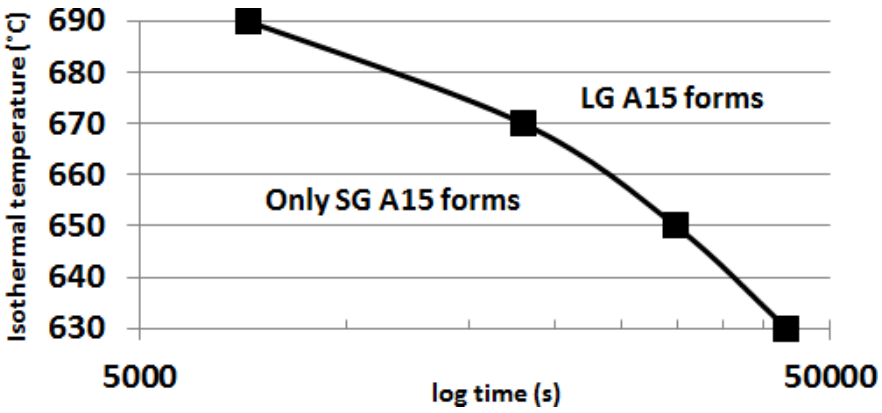

Figure 3.16: Isothermal transformation diagram showing how temperature and time effect the onset of large grain A15 formation in single dwell HT's. The line is generated from the right column of Figure 3.15 and is an approximate boundary for when LG A15 will form.

longer reaction times. However, high RRR is maintained by stopping the reaction before barriers breach, either by lower reaction temperatures or shorter reaction times. Since heat treatments which maximize J_c and RRR are in opposition to each other, a careful optimization needs to be made for each wire to achieve the best compromise.

3.3 Superconducting properties of PIT Nb_3Sn

The data in Figure 3.17 show the relationship between the J_c(12 T, 4.2 K) and RRR for one 0.85 mm and two 1 mm diameter wires with the various heat treatments detailed in Table 3.2. The two lowest J_c samples (~1800 A/mm^2) went through restricted HT's of 630/100 and 650/50. They show a very high RRR of near 300, but only 28% and 30% small grain A15 respectively (Table 3.2), significantly less than the 40% in optimum wires. Wires with the higher J_c(12 T, 4.2 K) values of ~2400 A/mm^2 have RRR between 130 and 175, and ~40% small-grained A15. We refer to this cluster of wires as "optimally reacted" since their properties are close to those required for the High Luminosity Upgrade of the LHC [74]. In addition, there is one over-reacted wire heat treated at 670/100 which had nearly the same J_c as the 670/50, but with RRR dropping from 130 to 67.

The 0.85 mm wires in the optimized cluster show a clear trend in A15 morphology. For optimized reactions at the reaction temperatures at 630, 650, or 670 °C there is a maximum SG A15 fraction

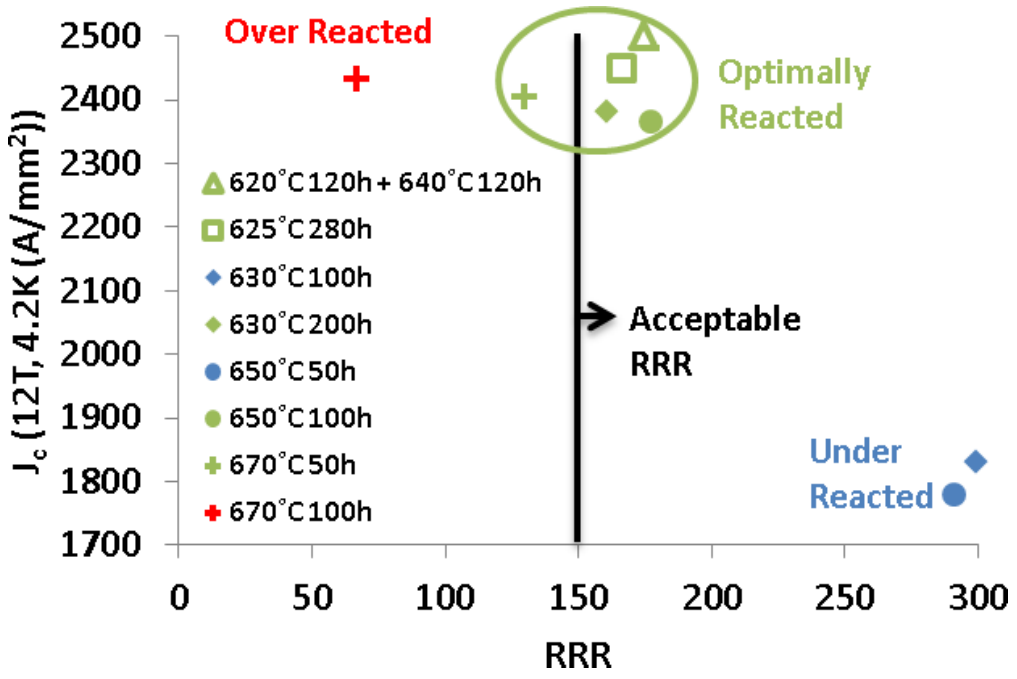

Figure 3.17: Correlation plot of J_c(12 T, 4.2 K) and *RRR* for 1 and 0.85 mm diameter PIT wires. The data show a high J_c wire with lower *RRR* (red), a low J_c cluster with high RRR>250 (blue), and a cluster of green points which are optimally reacted. The 1 mm wires are marked with open symbols and have slightly higher J_c than the 0.85 mm wires. The green cluster shows the important tradeoff between J_c and *RRR* that must be properly optimized.

of ∼38, 40, and 42% respectively, the core A15 then decreasing with increasing temperature to volume fractions of 3.0, 1.3, and 1.0% respectively (Table 3.1). These data show there is more overall A15 at higher temperatures, and much less core A15. It appears that higher temperatures agglomerate the voids in the core better, ensuring that core Sn has a diffusive path to the Nb-Ta tube where it forms SG A15. This is shown well in Figure 3.13 where the under-reacted filament has many small voids and 5% core A15, while the over-reacted filament shows a few large voids and only 0.6% core A15.

The important distinction between the two A15 morphologies is that small grains of A15 are needed for a high density grain boundary vortex pinning as described in chapter 1, while the large grain A15 has much lower grain boundary density. Moreover, as shown in Figure 1.8, Cu precipitates are present between the LG's, creating superconducting-normal-superconducting (SNS) junctions

Table 3.2: The two 1 mm wires have CERN sample ID's of He10S11403A01.U.006 for the HT of 620+640 °C HT and He10S11403A01.U.011 for the 625 °C HT. The 0.85 mm are from billet B29992, and the 0.78 mm wire is from billet B31284. J_c is in A/mm^2 and is measured at 12 T, 4.2 K. All reported dimensions were measured on reacted wires, while all J_c values were calculated over the unreacted filament area.

HT temperature (°C)	HT time (h)	Wire diameter (mm)	Filament diameter (μm)	Electrical Properties			Phase volume %	
				RRR	J_c non-Cu	J_c layer	A15 total	A15 SG
620+640	120+120	1.0	50	175	2500	6158	57.9%	40.7%
625	280	1.0	50	166	2450	6171	57.7%	39.7%
630	100	0.85	42	299	1830	6536	46.4%	28.0%
630	200	0.85	42	161	2380	6280	55.4%	37.9%
650	50	0.85	42	291	1779	5910	48.3%	30.1%
650	100	0.85	42	177	2367	5992	57.2%	39.5%
670	50	0.85	42	130	2404	5683	57.0%	42.3%
670	100	0.85	42	67	2433	5580	59.4%	43.6%
620+640	100+90	0.78	39	121	2444	5564	56.0%	40.2%
630	240	0.78	39	-	-	-	58.1%	40.7%

that prevent a superconducting path. Despite the change in reaction temperature from 620-670 °C, J_c values are very similar. This is because although high temperature reactions produce more SG A15, their grain size is bigger, reducing the grain boundary density and vortex pinning contribution to J_c [103]. A method to better correlate the J_c with the microstructure is to calculate a layer J_c, based on only the small grain A15 layer as described in section 1.4. Heat treatments with higher temperature and/or longer times have bigger small grains, and a suppressed $J_{c-layer}$ as shown in Table 3.2. $J_{c-layer}$ values for our standard design PIT wires range from 5580-6536 A/mm^2 at 12 T, 4.2 K. Most notably, the lowest $J_{c-layer}$ belongs to the most aggressive HT (670/100), while the highest $J_{c-layer}$ was attained by the HT with lowest temperature and reaction time (630/100). These results show that there are benefits and draw backs to both high and low temperature HT's, and in consideration of the results of our isothermal HT's in the 630-690 °C range, we designed a series of inverse multistage HT to avoid the LG A15 nucleation line in Figure 3.16 and attempt to get the best wire properties.

3.4 Inverse multistage heat treatments that benefit the small grain/large grain A15 ratio

In an attempt to avoid or at least delay the LG A15 nucleation, we designed four "inverse multistage" heat treatments (IMHT). We distinguish four different stages in these HT's:

- Ramp-up at 100 °C/h to the highest A15 reaction temperature (HRT).
- Short isothermal hold at the HRT
- Ramp-down to the isothermal, low-temperature A15 reaction temperature (LRT).
- A long LRT

All performed multistage HT's have a ramp-up of 100 °C/h and a LRT dwell at 630 °C. The HRT is either 670 or 690 °C, with HRT dwell times varying from 0-3.5 h, and the slow ramp-down to the LRT varies from 5-20 °C/h. Specific IMHT schedules are listed in Table 3.3 and shown in Figure 3.18. For the purpose of this work, we wanted to optimize the HRT, the HRT dwell time, and the slow ramp-down to the LRT dwell such that no LG A15 has formed and the layer thickness of SG A15 is maximized. Heat treatments and imaging were performed as described in chapter 2. Some of the following results have been previously reported in [104]

Table 3.3: Full heat treatment schedules for inverse multistage HT's.

HT name	Heat treatment schedule
Inverse multistage A	690/1, -20 °C/h, 630/220
Inverse multistage B	690/0, -5 °C/h, 630/190
Inverse multistage C	690/0, -5 °C/h, 670/0, -10 °C/h, 630/210
Inverse multistage D	670/3.5, -5 °C/h, 630/210

3.4.1 Microstructures early in the reaction

The first inverse multistage HT (A) was designed to grow the thickest layer of SG A15 possible before any LG A15 nucleated, then cool at a rate which stayed ahead of the LG A15 nucleation boundary shown in Figure 3.16. The first heat treatment "A" was then 690/1, -20 °C/h, 630/220. The LG A15 nucleated 13 hours into the LRT dwell at 630 °C when the SG A15 layer thickness was 2.2 μm, a 10 % increase in the SG A15 layer thickness with respect to the best single stage HT

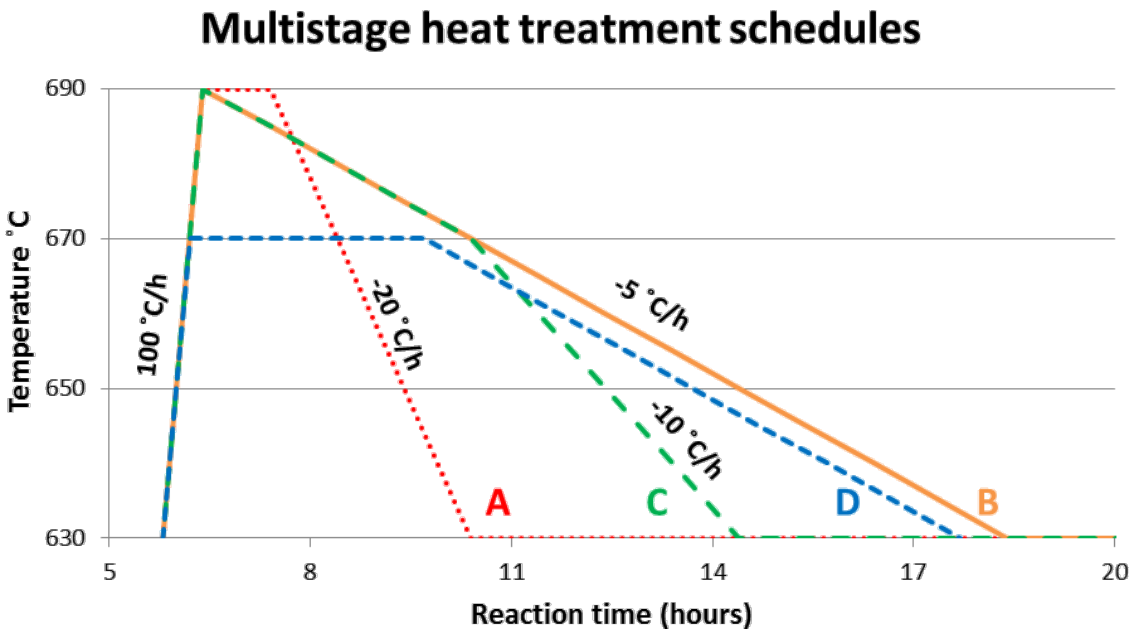

Figure 3.18: Heat treatment schedules for the inverse multistage HT's. All HT's ramp up at 100 °C/h to 690 °C, or 670 °C in the case of inverse multistage "D", then cool to 630 °C for ∼200 hours for the isothermal A15 reaction.

at 670 °C discussed in Figure 3.15. This experiment provided a proof of principle in using inverse multistage HT's to control LG A15 formation.

For inverse multistage HT "B" we recognized that while higher temperatures more rapidly grows SG A15 without nucleating LG A15, these higher temperatures do enable grain growth in the SG A15 layer, thus reducing the grain boundary vortex pinning density in the current-carrying portion of the filament. To balance these two effects, inverse multistage HT "B" ramped up to the 690 °C, but then skipped the 1 h hold at 690 °C and used a slow ramp rate of 5 °C/h from 690 °C to the LRT dwell at 630 °C. The LG A15 nucleated at 650 °C during the ramp down to the LRT dwell, with the SG A15 having a layer thickness of 2.7 μm, a 35% increase over the single step HT at 670 °C.

My interpretation of this early onset of LG A15 formation is that the cool-down to the low, isothermal reaction temperature was too slow, since the sample crossed the LG A15 nucleation line. For inverse multistage "C" we then kept the early portion of the ramp-down at 5 °C/h until 670 °C, then doubled the ramp rate to 10 °C/h. The LG A15 nucleated 10 hours into the 630 °C LRT

dwell with a SG layer thickness of 3 μm , which marks a 50% improvement in SG A15 thickness compared to the 670 °C single step HT.

Our last inverse multistage HT "D" lowered the HRT dwell to 670 °C in an effort to minimize SG A15 grain size, the HT being (670/3.5, -5 °C/h, 630/210). LG A15 formed during the ramp-down around 650 °C, with a SG A15 layer thickness of only around 2.2 μm; slightly better than the isothermal heat treatment at 670 °C.

3.4.2 Discussion of final microstructures

Inverse multistage HT "C" was the best at delaying LG A15 while producing the most SG A15 early in the reaction as is seen in Figure 3.19. The results of the four IMHT's after a full reaction are compiled in Table 3.4. The SG/LG A15 ratio in an optimized 0.78 mm PIT wire is 2.8, and all inverse multistage HT substantially enhanced this ratio, some reaching as high as 3.9. Inverse multistage heat treatments "A" and "B" had ~56% SG A15, however, IMHT "C" added another 0.5% volume fraction to each of the SG, LG, and core A15 morphologies to produce 57.3% total A15. A filament cross-section from inverse multistage HT C is shown in Figure 3.20.

Table 3.4: Final microstructure of the four wires heat treated using inverse multistage HT's, and the standard HT BEAS wire included for reference. J_c in A/mm^2 at 12 T, 4.2 K, calculated over the unreacted filament area.

			Electrical Properties			Phase or morphology volume %						
HT (°C)	HRT (°C)	Time in LRT dwell (h)	I_c(A)	J_c non-Cu	J_c layer	DB	A15 total (S+L+C)	Remnant core	A15 SG	A15 LG	A15 core	A15 SG/LG ratio
620+640	-	100+90	501	2444	5564	23.4%	56.0%	20.6%	40.2%	13.3%	2.5%	2.8
Inverse multistage A	690	220	-	-	-	25.4%	56.3%	18.4%	43.5%	12.0%	0.8%	3.6
Inverse multistage B	690	190	489	2385	4958	24.4%	56.0%	19.4%	44.0%	11.2%	0.8%	3.9
Inverse multistage C	690	210	491	2395	4926	24.0%	57.3%	18.7%	44.5%	11.6%	1.2%	3.8
Inverse multistage D	670	210	493	2405	5137	24.5%	56.6%	18.9%	42.8%	12.4%	1.3%	3.5

An interesting result from the inverse multistage HT's is that the only HT with an HRT dwell below 690 °C had the least SG A15, but the most LG and residual core A15. We originally believed this is because higher temperatures agglomerate the voids in the core better, ensuring the Sn has a diffusive path so it can reach the Nb-Ta tube and form SG A15. However, the inverse multistage heat treatments reacted about the same or *less* of the DB and formed nearly the same total A15 than our comparison HT which lacked the HRT stage. Nonetheless, the SG A15 layer was increased

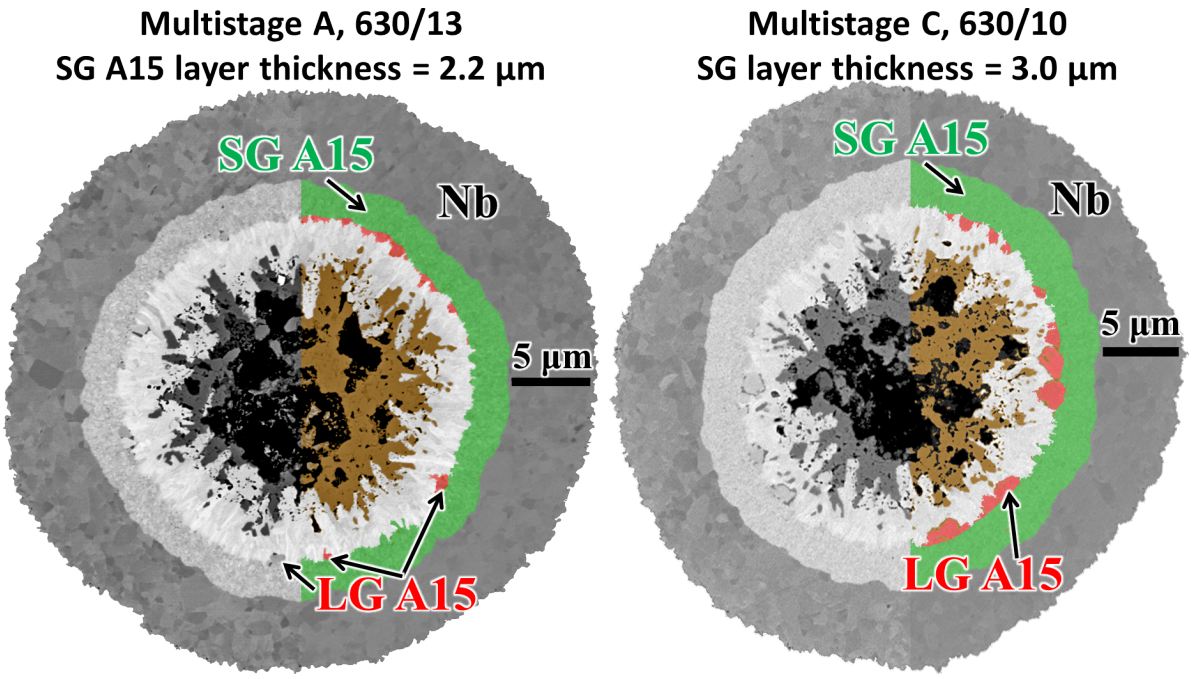

Figure 3.19: FESEM-BSE images of polished, transverse cross-sections of samples quenched from the furnace comparing inverse multistage HT "A" and "C" as the LG A15 is forming. Filaments are half colored to distinguish between phases. SG A15 in green, and LG A15 in red. The SG A15 layer thickness of both inverse multistage HT "A" and "C" are substantially enhanced from those SG A15 layers shown in the isothermal HT's of Figure 3.15.

by 10%, and this was an unexpected result. It implies that above 670 °C the core Nb from the Nb_6Sn_5 possibly interacts with the tube wall and form SG A15 *before* it decomposes into the LG A15. This further explains the reduced LG and core A15, whose volume seems to be added directly into the SG A15 layer. The evidence here shows that if the goal is to maximize the SG A15, the HT must either contain a isothermal dwell which is at a relatively high temperature of 670 °C as shown in Figure 3.13, or an HRT of ∼690 °C in the beginning of the HT as utilized in the inverse multistage heat treatment series. This stage above 670 °C providing time for the Nb_6Sn_5 to interact with to the Nb-Ta tube wall.

3.4.3 Critical current density measurements

To understand the effect of those various heat treatments and their significantly different microstructures, we compared I_c values of the IMHT's to the standard wire with HT of 620/100 +

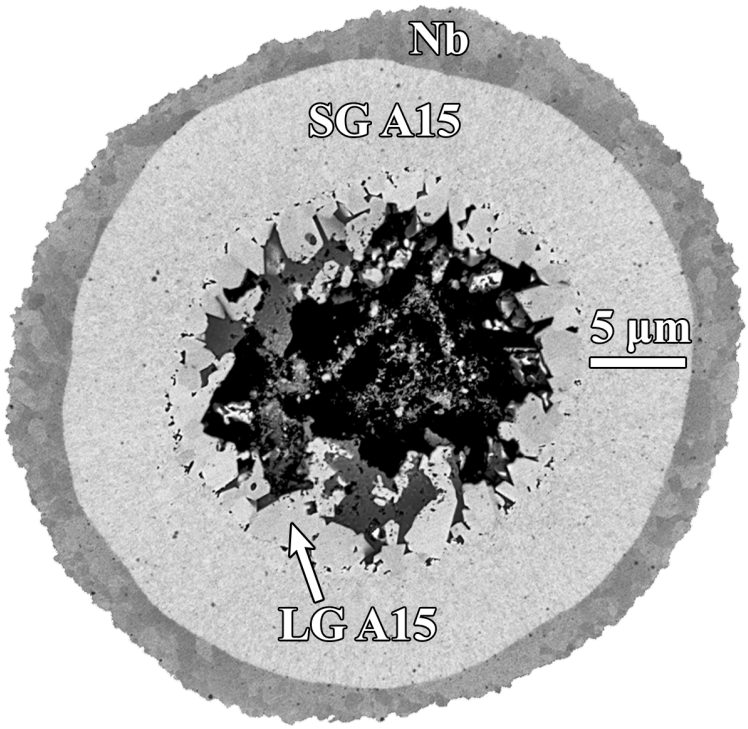

Figure 3.20: FESEM-BSE image of a polished, transverse cross-section showing an inner ring filament from inverse multistage HT C (690/0, -5 °C/h, 670/0, -10 °C/h, 630/210). The LG A15 fraction has been reduced to 11.6% compared to the 13.3% in a more typical HT (620/100 + 640/90). The LG A15 are only loosely connected to the SG A15 layer.

640/90. I_c values of IMHT's "B", "C", and "D" varied by less than 1%, from 489-493 A; about 2% less than the standard wire (Table 3.4). However, I_c is strongly dependent both on the amount of SG A15, and its grain size. We can better understand the differences between IMHT's by comparing $J_{c-layer}$. A wire reacted with a standard HT (620/100 + 640/90) has a $J_{c-layer}$(12 T, 4.2 K) of 5564 A/mm^2, while the highest $J_{c-layer}$ in the IMHT series was "D" which had a $J_{c-layer}$(12 T, 4.2 K) of only 5137 A/mm^2, a substantial drop. The cause of this drop in $J_{c-layer}$ is from the A15 formed above 670 °C which has a larger grain size than the standard wire reacted at lower temperatures of 620-640 °C. In Figure 3.21 the grain size is compared between IMHT "C" and a 625 °C heat treatment reproduced from [68]. Inverse multistage HT "C" was chosen for this grain size analysis because it showed the highest volume of SG A15 in this series of HT's, the anlysis was provided by Peter Lee. The top image is a color map of the area equivalent diameter for each

grain in IMHT "C" where lighter color depicts larger grains and darker depicts smaller grains of A15, the white areas in the SG A15 layer could not accurately be measured and were omitted. The plot on the bottom left shows the area equivalent grain diameter as a function of distance from the Nb-Ta diffusion barrier as shown in the top image of Figure 3.21. The bottom right plot is magnified from the left plot to show the SG A15 layer, the purple dashed lines and corresponding temperatures show the HT temperature at the time of the SG A15 formation for this IMHT "C". The SG A15 layer is approximately 6000 nm thick, with another 2000 nm of LG A15. The SG A15 which formed above 630 °C had an average grain size up to 170 nm in diameter, and a few individual small grains grew as large as 400 nm. However, the SG A15 layer which formed during the isothermal portion of the HT at 630 °C have grain diameters in the 100-110 nm range, slightly larger than the 90 nm grain size found in the 625 °HT for comparison. Close to the diffusion barrier, there are additionally columnar A15 grains that are larger in diameter (about 130 nm) than the equiaxed grains, however, these are common across all Nb_3Sn PIT wires regardless of HT.

This clearly shows how the high temperature stage of the HT above 670 °C degrades the $J_{c-layer}$ by reducing GB density. To try to minimize the reduction in grain boundary density, IMHT "D" only went to a maximum of 670 °C. Inverse multistage HT's "B" and "C" had a very similar $J_{c-layer}$(12 T, 4.2 K), but it is 10% lower than the standard HT for this wire. By staying below 670 °C, some of the $J_{c-layer}$(12 T, 4.2 K) was recovered, increasing from about 4940 A/mm^2 in HT's B & C to 5140 A/mm^2 in IMHT "D". However, less SG A15 and total A15 is produced. This result agrees with our grain size analysis in Figure 3.21 which shows that the grain size at higher temperatures early in the reaction is larger than at 630 °C, lowering grain boundary vortex pinning density.

It is clear that these inverse multistage HT's have benefits and drawbacks to consider, and additional optimization may still improve wire properties. High temperatures agglomerate voids in the core and provide a diffusive path for Sn to reach the Nb-Ta tube to maximize SG A15 formation, but also perhaps allows Nb_6Sn_5 to interact with the tube wall. However, a temperature as high as 690 °C is detrimental to grain size, and therefore grain boundary vortex pinning. The best solution might be to only go as high as 675-685 °C for 0-4 h. The data show that small changes to temperature and time during this sensitive portion of the HT can have substantial effects on the SG/LG A15 ratio and warrant further exploration.

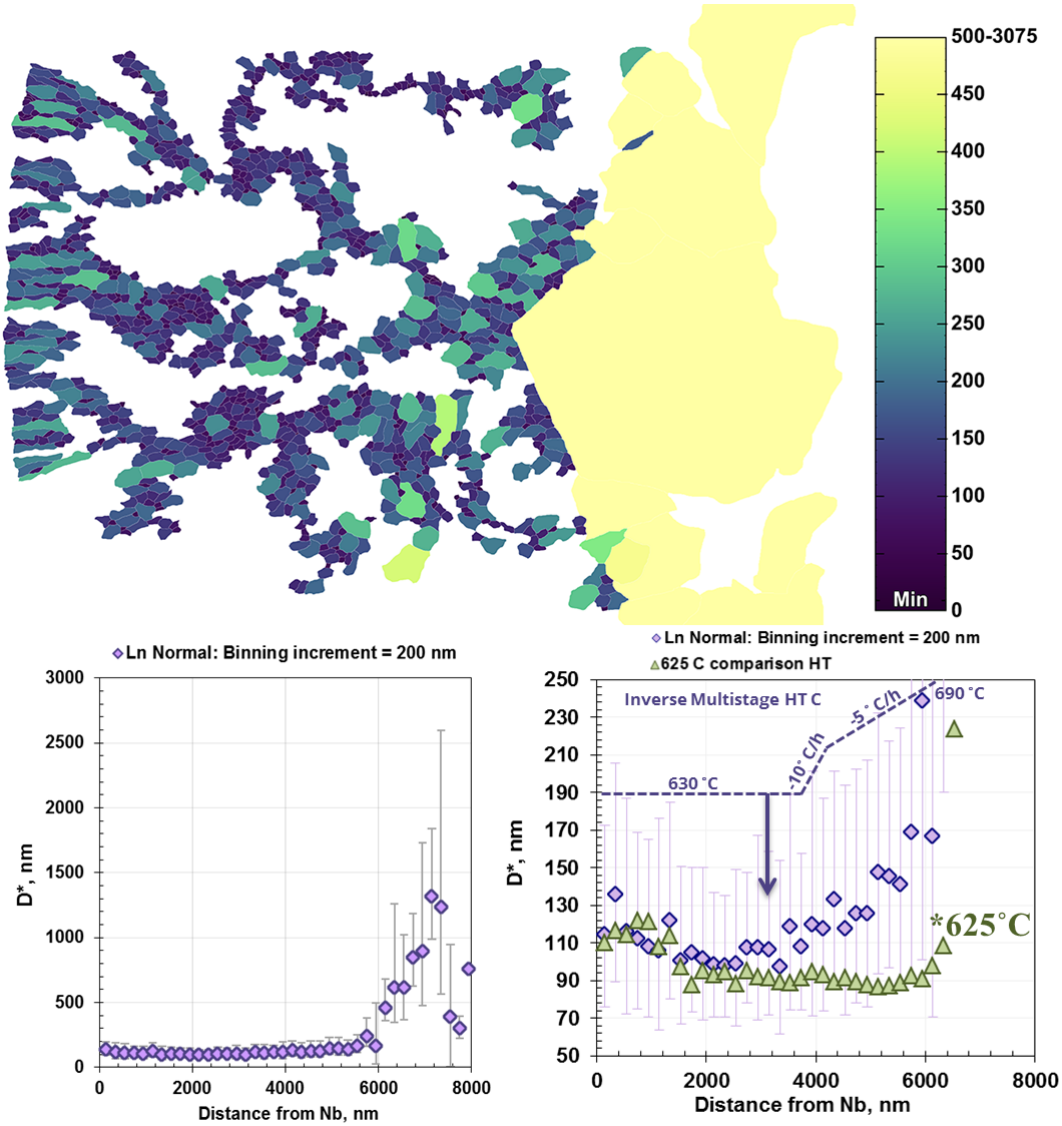

Figure 3.21: Grain size of the SG A15 after inverse multistage HT "C" in comparison to 625 °C HT from [68]. The top image is a color map of the area equivalent diameter of each grain in HT "C", lighter color depicts larger grains and darker depicts smaller grains. Grain size measurements were provided by Peter Lee The plot on the bottom left shows the diameter as a function of distance from the Nb-Ta diffusion barrier. The bottom right plot is magnified from the left plot to show the SG A15 layer, the purple dashed lines and corresponding temperatures show the HT temperature at the time of the SG A15 formation for this IMHT "C". The SG A15 which formed above 630 °C had an average grain size up to 170 nm in diameter, and a few individual small grains grew as large as 400 nm, while those grains that formed at 630 °C had grain diameters in the 100-110 nm range; just above the 90 nm grain size found in the 625 °C HT [68]. Close to the DB, both heat treatments show columnar A15 grains larger in diameter (up to ∼130 nm) than the equiaxed grains.

3.5 Summary and conclusions

As optimizations of both J_c and RRR are in general opposition to each other, we focused on driving J_c as high as possible without regard to RRR. The main considerations for improving J_c is to form smaller grains of A15, or form more SG A15 by either increasing Sn diffusion to the Nb-Ta tube, or by altering the reaction conditions to suppress the formation of LG A15 in favor of SG A15. The phase evolution studies, which ended at the A15 reaction, showed a complex reaction pathway:

$$NbSn_2 + Cu \rightarrow (Nb_{0.75}Cu_{0.25})Sn_2 \rightarrow NbSn_2 + Cu_x \rightarrow Nb_6Sn_5Cu_x \rightarrow Nb_3Sn(LG) + Cu_x + Sn \quad (3.2.2)$$

Above 600 °C, Nb_6Sn_5 delivers Sn to the Nb-Ta tube to first form SG A15, but later in the reaction the residual Nb_6Sn_5 decomposes into LG A15. The precursor to Nb_6Sn_5 is the Nb-Cu-Sn intermetallic known as Nausite, and we believe that minimizing the Nausite would be beneficial for reducing LG A15. We found that Nausite forms as low as 200 °C and appears to grow to its thermodynamic equilibrium under normal wire heating conditions <100 °C/h. We conclude that Nausite is thermodynamically unavoidable with this initial chemistry and architecture, and any time spent below ∼600 °C will only serve to grow the Nausite and later form more undesirable LG A15.

During the isothermal A15 reaction at 630 °C, SG A15 started to form first around 5 h, while LG A15 formed a short time later from Nb_6Sn_5 decomposition, during which Cu is ejected into the LG A15 grain boundaries. Both the SG and LG A15 layers grow as the HT progresses, the Nb_6Sn_5 disappearing around 94 h. At this point, ϵ Cu-Sn phase supplies Sn through the existing SG and LG A15 grain boundaries to react with the remaining Nb-Ta tube. After about 200 h the SG A15 layer stops growing, producing final A15 morphologies of ∼41% SG A15, 14% LG A15, and about 3% A15 trapped in the core of the 0.78 mm wire.

To study the effects of the A15 reaction temperature on the final wire properties, a series of six wires were sent to ASC from CERN which were identical except for the HT which varied from 630-670 °C for 50-200 h. This series demonstrated that the A15 conversion is substantially better at higher temperatures, the SG A15 volume fraction climbing from 38% to 43% in optimized HT's.

Additionally, the core A15 dropped from 3.0 to 0.4%, and the filament cores showed agglomerated voids compared to the lower temperature HT in which voids tend to surround the remaining A15 trapped in the core. The voids then separate the Sn from the tube wall and inhibit a well defined diffusion path to the Nb-Ta tube to form SG A15. This series of wires also made clear that higher temperatures produce slightly higher J_c values, largely by forming more SG A15. However, the $J_{c-layer}$ is substantially lower than that at 630 °C. The RRR values in this series show that higher temperatures decrease RRR as low as 67, while the RRR in low temperature HT's easily remains above 150.

Earlier work done on Shape Metal Innovations PIT wires made ∼20 years ago optimized for reactions in the 675 °C range showed a larger SG A15 layer formed before the appearance of LG A15 [102], implying that the SG/LG A15 ratio is strongly temperature dependent early in the HT. I then decided to heat treat wires at various temperatures between 630-690 °C to understand LG A15 formation in the early hours of the HT. We found that the SG A15 always forms first, the LG A15 following a short time later, and the time-gap shrinking as temperature increased. The maximum SG A15 layer that could be formed was about 2 μm at 670 °C after 4.5 h before the LG A15 formed. This was a substantial improvement over the 0.85 μm SG A15 layer thickness achieved before LG A15 formation in the 630 °C HT.

The temperature dependence of the SG/LG A15 ratio early in the reaction incited new heat treatments to be developed which first went to a high temperature of 670-690 °C, then slowly cooled ($\leq$ 20 °C/h) to a final isothermal reaction temperature of 630 °C. All four of these inverse multistage HT's increased the SG/LG A15 ratio. In the best case for improving the SG A15 volume (inverse multistage HT "C"), the SG A15 reached 44.5% of the cross-section with a SG/LG ratio of 3.8, substantially improved from the 2.8 in a standard heat treatment in the 620-640 °C range. These results were promising as we drove the bad A15 (core and LG) down from 18% to about 12%. However, the J_c decreased slightly for all wires. This was due to the larger grain size of the SG A15 which forms during the high temperature portion of the HT (above ∼640 °C), further evidenced by comparing the $J_{c-layer}$ between them. However, since small perturbations in temperature and time during the high temperature portion of the HT can have substantial effects on the SG/LG A15 ratio, further exploration is still recommended in the 675-685 °C range to determine the practicality of improving J_c through use of inverse multistage heat treatments.

CHAPTER 4

DEGRADATION OF J_C AND *RRR* PROPERTIES BY NON-UNIFORM FILAMENT DEFORMATION DURING WIRE FABRICATION

During wire fabrication, filaments incur non-uniform deformation that can be detrimental for both *RRR* and J_c. Through comprehensive SEM imaging and digital analysis paired with electrical property measurements, I found that a major but previously unreported source of degradation for these PIT wires is a movement of the filament cores away from the centers of the filaments towards the center of the strand cross-section. This "centroid drift" creates a thin inner side and a thick outer side for the diffusion barrier in each filament. Because the A15 reaction proceeds radially from the core, the thinned side reacts through while there is still a thick layer of unused Nb-Ta on the opposite side. Once the thinned layer has reacted through, the Sn can diffuse through the A15 layer directly into the Cu matrix, reducing the amount of Sn available for the further reaction of filament. Thus the centroid drift potentially decreases the overall critical current density of the wire and the magnet stability. We also report on an experiment that sequentially removes the rings of filaments furthest from the wire center, and the Cu surrounding them, so as to measure the local variation in RRR and J_c as a function of distance from the wire center.

4.1 Filament deformation and barrier failure effect

Mono-filaments, as assembled, have a symmetrical cross-section with an aspect ratio of one, where aspect ratio is defined as the ratio between major and minor diameter. However, mechanical processing to final size results in some distortion of the filaments, particularly those in the outer filament rings. We can classify the resulting filaments into three types. The first is encountered in the inner rings of filaments (1-4), where the majority retain their round shape with little distortion as seen in figure Figure 4.1a. In the outer rings (5-7) the second type is seen, where filaments tend to be heavily aspected with substantial thinning of the DB on the side facing the wire center and a thickening of the outer side (Figure 4.1b). During the reaction HT the thin side reacts-through

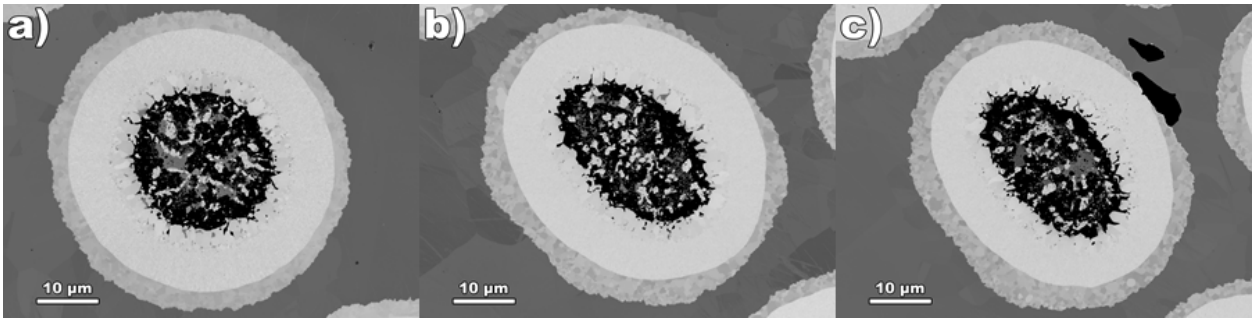

Figure 4.1: FESEM-BSE images of polished cross-sections of representative filaments from the 1 mm diameter conductor after reaction of 620/120 + 640/120. Each image is oriented with the wire center towards the upper right. (a) Typical inner ring filament with aspect ratio close to 1 and rather uniform residual diffusion barrier thickness. (b) Typical outer ring filament with aspect ratio ∼1.3 showing barrier thinning on the side facing the wire center with potential for A15 to contact the Cu. (c) A broken outer ring filament where the A15 layer touches the Cu at the top right, allowing Sn leakage into the Cu and degradation of RRR. Despite the leakage, this sample still maintained RRR = 175.

prematurely, resulting in SG A15 that is in direct contact with the Cu stabilizer, allowing Sn to diffuse into the Cu (thus reducing RRR) and limiting further reaction of the tube (and thus its contribution to I_c). In some cases the Sn flux into the Cu is sufficient enough to form a void, and the total volume of SG A15 is significantly reduced. This void forms by the Kirkendall effect, whereby the diffusion coefficient of Cu in Sn is sufficiently higher than the diffusion coefficient of Sn in Cu, and vacancies diffuse out of the Sn and precipitate in the Cu [105]. This third type of filament showing a Kirkendall void is shown in Figure 4.1c.

In addition to poisoning the Cu, we also observed that the leaked Sn can form A15 phase on the outside of the diffusion barrier as seen in Figure 4.2. In Figure 4.2b we see a leak in ring seven that was large enough to form a Kirkendall void nearly 20 μm wide between the A15 and the stabilizing Cu. The A15 has formed not only on the outside of the broken filament, but also on the neighboring filament, thus demonstrating the significant mobility of Sn in Cu. Figure 4.2 d & e show that this external A15 forms as far in as ring four, despite breaks generally occurring only in the outer two rings (6 and 7). Because of the discontinuity and low Sn content of this A15 layer it is unlikely to contribute to the transport J_c. The high mobility of Sn in Cu demonstrates the necessity to prevent leaks because outer barrier breaches can spread Sn widely into the Cu around

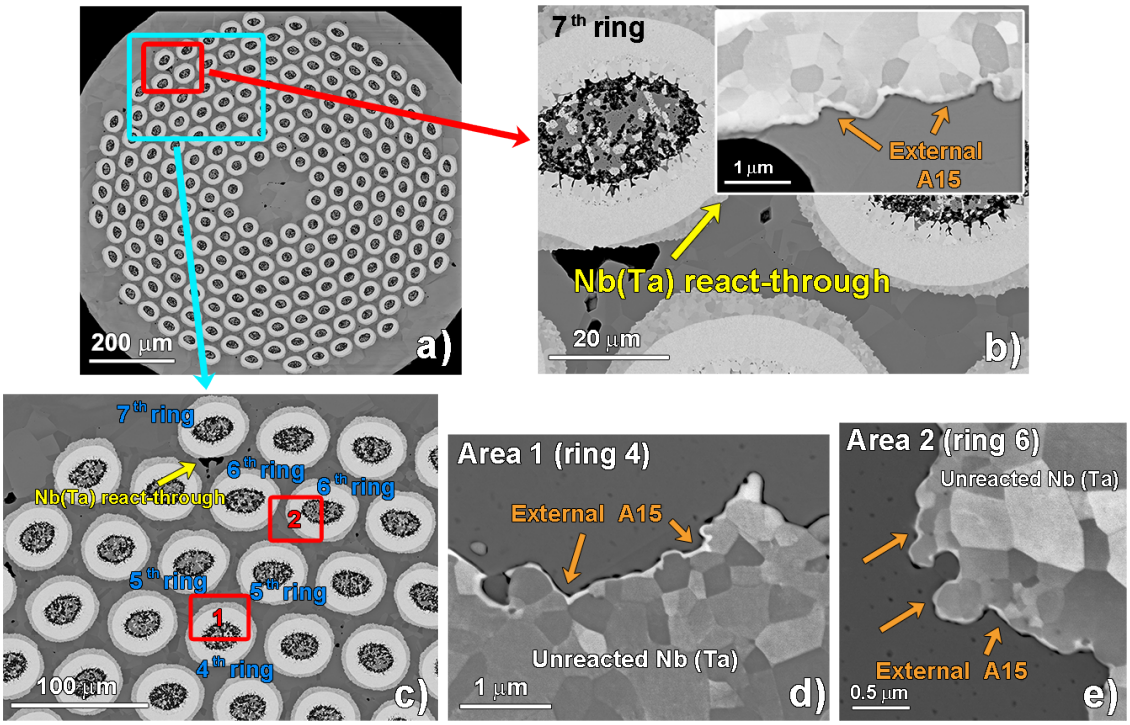

Figure 4.2: FESEM-BSE images of polished, transverse cross-sections of a 1 mm diameter PIT wire reacted for 280 h at 625 °C with *RRR = 166*. (a) Whole wire overview, (b) close up of A15 formation external to a breached diffusion barrier in outer ring 7 and a Kirkendall void formed by dissolution of Sn in the stabilizing Cu, (c) overview of filaments in rings 3–7 in the vicinity of the breach, (d) and (e) A15 formation on barrier outsides appears as far away as ring four.

inner ring filaments. This is an issue because very low levels of Sn in the Cu produce catastrophic drops in *RRR*.

In Figure 4.3 the filaments in a wire cross-section are color-coded so that the spatial distribution on filament aspect ratio can be easily observed. In this case it increases from a minimum of 1.01 in ring 1 up to a maximum of 1.31 in ring 7. In this cross-section we also find two large Kirkendall voids that have formed adjacent to the more aspected filaments of the outer two rings, marked with a red arrow in Figure 4.3. The most aspected filaments clearly occur in the outer ring filaments, while inner filaments remain mostly circular.

In Figure 4.4a, the filaments in a transverse cross-section of a 0.85 mm wire (650 °C/100 h) are color coded according to their continuous A15 area (LG+SG). In this case the overall variation in A15 area across the sample is small (Coeff. Var = 3.7%) except for two of the filaments, and

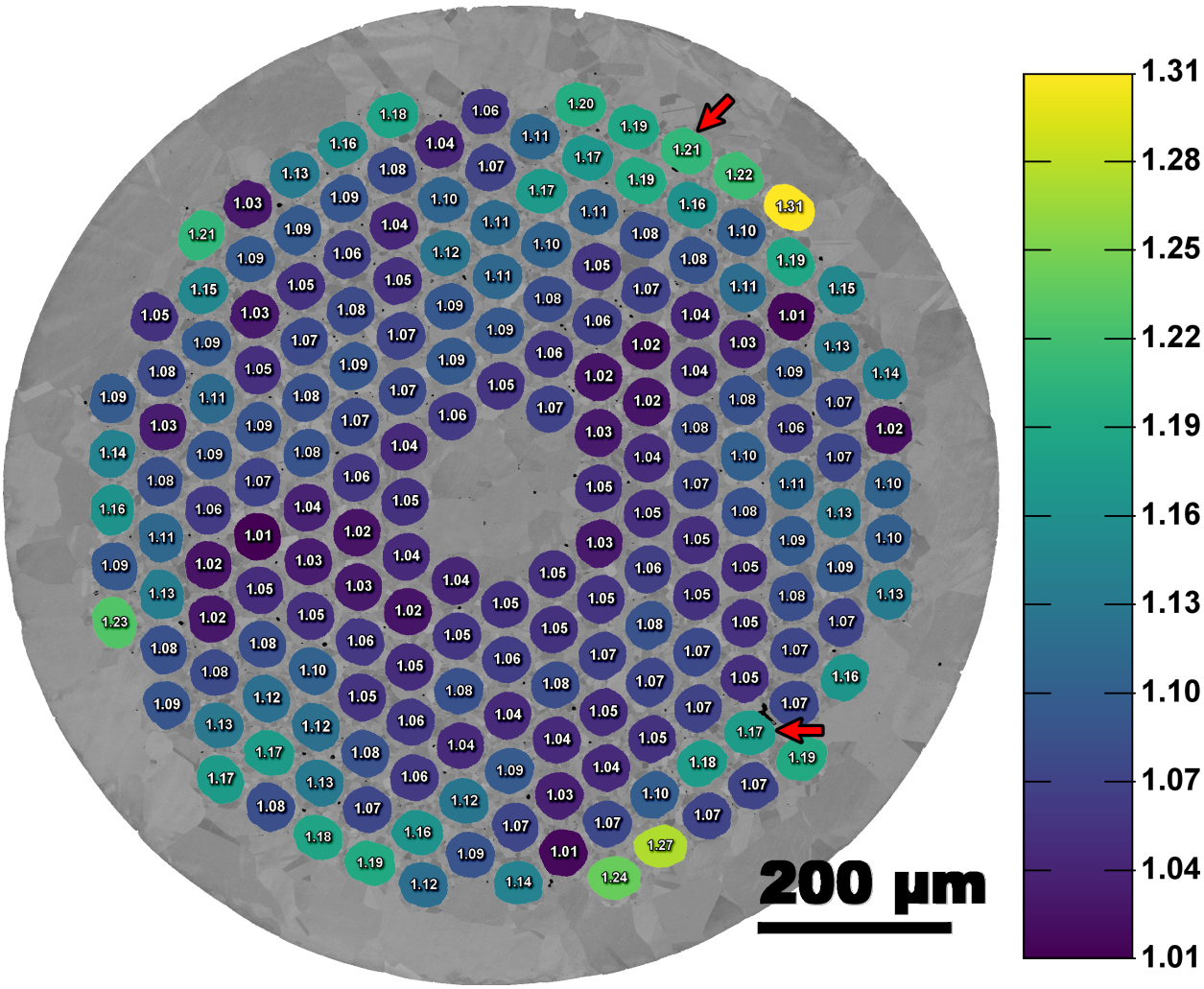

Figure 4.3: A color map of filament aspect ratio showing a range from 1.01 (dark/purple) to 1.31 (light/yellow). The two filaments with barrier breakthrough and a Kirkendall void are marked with a red arrow. This 1 mm diameter wire with CERN sample ID He10S11403A01.U.006 was reacted for 620/120 + 640/120 and had $RRR = 175$.

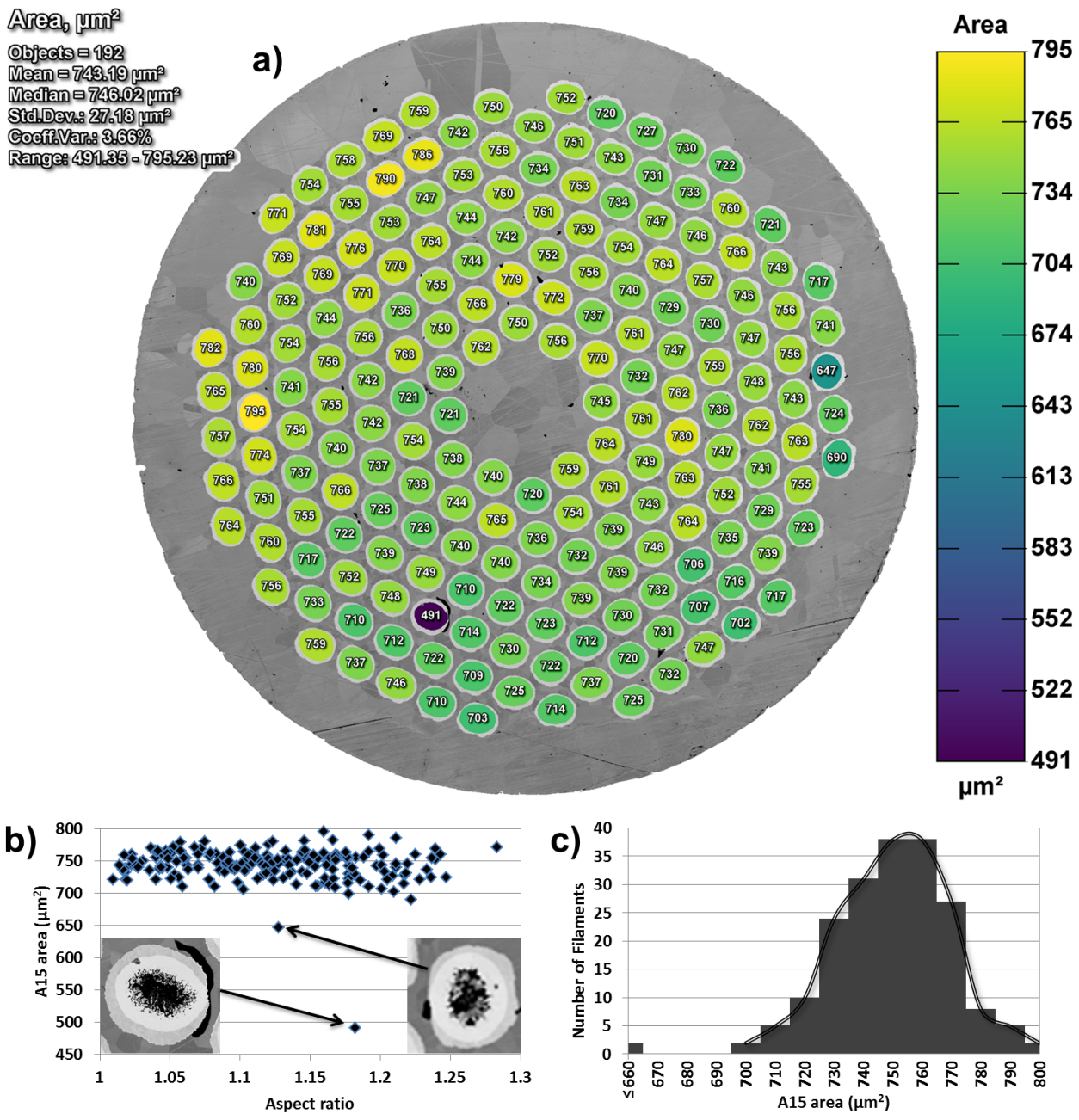

Figure 4.4: This 0.85 mm diameter wire was reacted for 100 h at 650 °C and had RRR = 145. The color map (a) is colored by connected A15 area in each filament (LG + SG), the lighter color depicting more A15 and darker colors depicting less A15, summary statistics are shown in the upper left. In (b) the filament A15 area as a function of its aspect ratio: two filaments have A15 area well below the mean, corresponding to the two darkest filaments in the color map of (a). The histogram in (c) shows a roughly Gaussian distribution of the A15 area with all but two filaments within 3σ: these are the filaments with lowest A15 area in (a) and (b).

we do not see the radial dependence observed in the aspect ratios in Figure 4.3. For this 0.85 mm wire, if we plot aspect ratio against A15 area we also find no dependence (Figure 4.4b). There are, however, two filaments that have A15 areas below three standard deviations from the mean as shown in the histogram in Figure 4.4c. The two filaments with a clearly reduced A15 area show leakages with evident Kirkendall voids, despite being only moderately aspected.

Our conclusion is that any barrier breach will allow Sn to flow into the Cu and lower *RRR*, however this does not generally affect the amount of SG A15 since barrier breakthrough frequently occurs towards the end of the reaction. However, when local thinning of the tube wall is severe enough to cause barrier breach earlier in the reaction, enough Sn can leak out to form a Kirkendall void, and the SG A15 area is substantially reduced. While the aspect ratio and Sn leaks are both radially dependent, the aspecting does not necessarily cause Sn leaks. An explanation for this is that if the aspecting is symmetrical about the core, the tube wall remains constant and so the Sn diffusion distance across the Nb4at%Ta tube is also constant, so that premature breaching is not in itself sensitive to aspect ratio.

However, the different deformation rates between the porous, Sn-rich powder core and the Nb-Ta reaction tube, may cause an asymmetrical filament deformation such that the center of the core is no longer at the center of the filament, leading to the large variation in barrier thicknesses, creating an uneven reaction front with a distinctly thin and thick side as shown in Figure 4.5. The centroid drift of each filament core was normalized to its filaments area effective diameter to allow comparison across samples of various filament size. This was done by measuring the distance between the center of a filament, and the center of its A15 and core area (as shown in Figure 4.5), then dividing by the filaments area effective diameter. Because of this centroid drift, during the heat treatment the thin side can be prematurely reacted through. To prevent this (and the consequent *RRR* reduction) the heat treatment has to be limited but at the expense of a reduced amount of SG A15. Thus a large amount of unused Nb-Ta DB is left behind on the thick side. Overall, the unused DB makes up 25% of the non-Cu cross-section. Figure 4.6 shows how the centroid drift steadily increases with distance from the wire center, the yellow data points showing the local average for each ring of filaments. As with aspect ratio, the color map in Figure 4.7 further illustrates that centroid drifting occurs more in the outer filaments than inner filaments. The one leak in this cross section occurred in ring seven in a filament with 2.58% centroid drift.

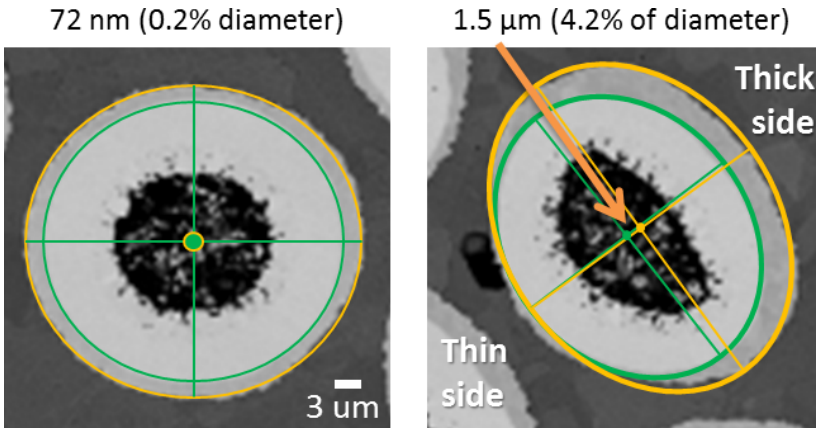

Figure 4.5: On the left, an inner ring filament with very little core drift where the centroids of the A15 layer and the Nb-Ta tube are nearly identical. On the right, a heavily deformed filament whose Sn core drifted 1.5 μm from its filament center (4.2% of its diameter), allowing enough Sn to leak out that a large Kirkendall void has formed at the tube:Cu interface.

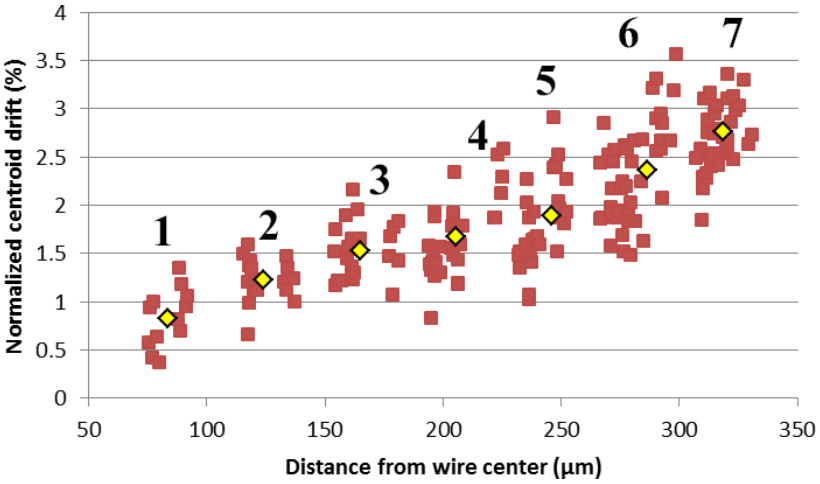

Figure 4.6: Normalized centroid drift becomes worse further away from the wire center in the 0.78 mm wire with heat treatment 620/100 + 640/90. The yellow, diamond data points are local ring averages and are labeled 1-7 above the data.

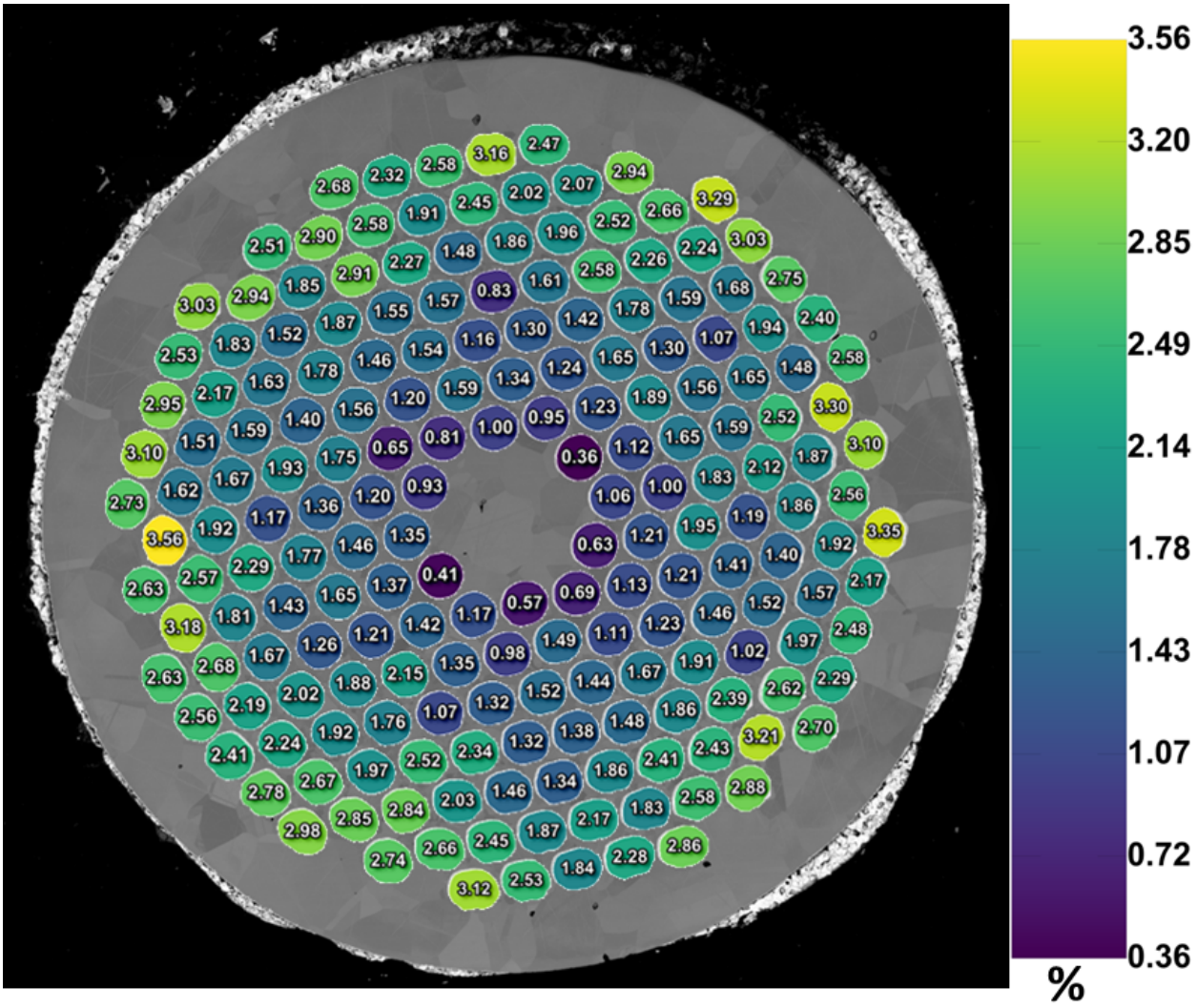

Figure 4.7: Colormap of normalized centroid drift in the 0.78 mm wire with heat treatment 620/100 + 640/90. Centroid drift becomes substantially worse in outer filaments, this cross-section showed one leak in a filament with 2.58% centroid drift.

To further quantify the impact of centroid drift on residual barrier thickness, we measured the variation in barrier thickness within each filament in a 1 mm wire (625 °C/280 h), by measuring the shortest distance between each pixel at the A15:Diffusion barrier interface, and the Cu stabilizer. In the case of a barrier breach, this distance goes to zero. When grouping the results for each filament by ring number (Figure 4.8), we found that the centroid drift is minor for the inner rings (1-4) with no detrimental thinning of the DB. However, the variation in barrier thickness increases in rings 5 to 7 where there are regions with the DB thickness going to zero on one side, and showing a thickening

of the DB on the opposite side of the distribution. Although the mean barrier thickness varies by less than 5% for all rings, the standard deviation grows substantially in the outer rings. For rings 1 through 4 there is little variation in minimum thickness (0.8-1.1 μm), maximum thickness (4.6-5.1 μm), or standard deviation (0.6-0.7 μm). However, in rings 5 to 7, the maximum thickness gets as high as 7 μm, while the minimum goes to zero due to the A15 reaction front reaching the Cu as shown in Figure 4.1c. Most noticeable is the widening of the distributions, the standard deviation of outer filament rings almost doubling to 1.3 μm compared to the inner rings.

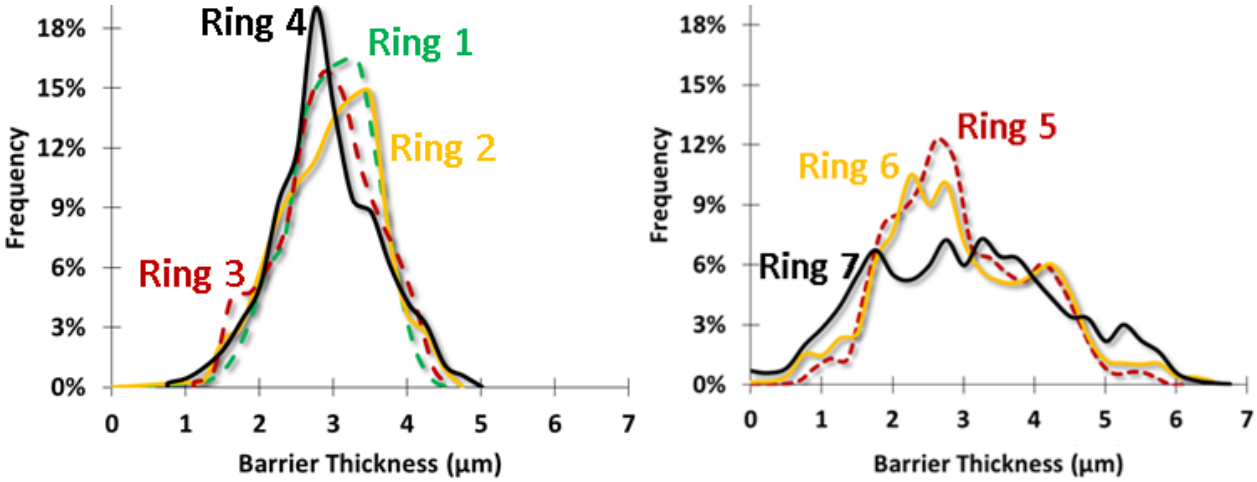

Figure 4.8: Distribution of residual barrier thicknesses within each of the seven rings of filaments in a 1 mm wire after reaction of 280 h for 625 °C. Barrier thickness variation is small in the four inner rings but significantly worsens in outer rings 5–7, in some cases the DB thickness going to zero.

Although only one or two filaments leaked in a given cross-section, breakdown is imminent in multiple filaments due to the stronger local distortions in the outer rings, even with the barriers globally comprising 25% of the non-Cu area. These signs of incipient DB failure are of definite concern when considering the additional filament distortion occurring during the Rutherford cable manufacture, particularly at narrow cable edges [106], as only two or three breached barriers can drop RRR below acceptable limits. Given that we are only looking at one cross-section from what could be 1 km or more of magnet strand, it is reasonable to assume that most filaments in the outer rings experience these local breaches somewhere along the length of the strand. We will describe a "metallographic tomography" which can be used to gather better statistics along the wire length in subsection 5.2.5.

4.2 Serial etching experiment reveals a leak zone of low *RRR*

4.2.1 Effects of the leak zone on *RRR*

To determine the local impact of barrier breakthrough on RRR I measured the resistivity after progressive etches in which Cu was sequentially removed from the surface of two 1 mm diameter wires, previously reported in [49]. Standard four-point contacts were made on a short 1 cm long sample whose resistance was then measured in a Physical Property Measurement System (PPMS). After the measurement, the current and voltage contacts were removed and the sample immersed in a dilute nitric acid bath for 5-10 min to partially remove the Cu matrix. Current and voltage leads were attached, and RRR was measured again. This process was repeated until ∼4-5 inner rings of filaments remained. Transverse cross-sections showing the approximate depths of each etch are shown in Figure 4.9, and their corresponding RRR values are plotted in Figure 4.10. This progressive etching revealed that RRR steadily degrades from 166-175 to 93-125 with removal of the outer sheath of Cu until the filament pack is exposed. Removing the two outer filament rings containing the 2 or 3 broken barriers and their surrounding degraded Cu shows *RRR* returning to >170 because of the pure Cu remaining in the wire center.

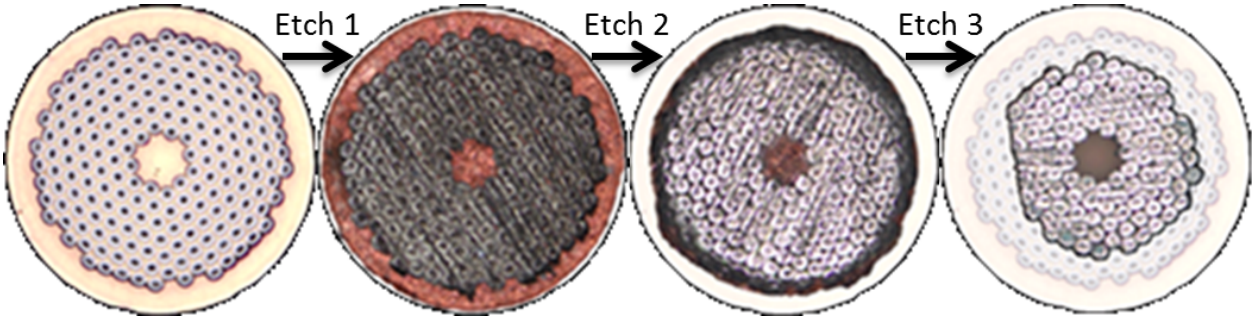

Figure 4.9: Light microscope images of a progressively etched 1 mm diameter PIT wire cross-sections. The images of the etched wire are overlaid on the initial cross section, the left is the initial wire, with progressive etching moving to the right. Etch 3 removed the outer two filament rings, as well as some interfilamentary Cu further into the wire. *RRR* was measured after each etch as is shown in Figure 4.10.

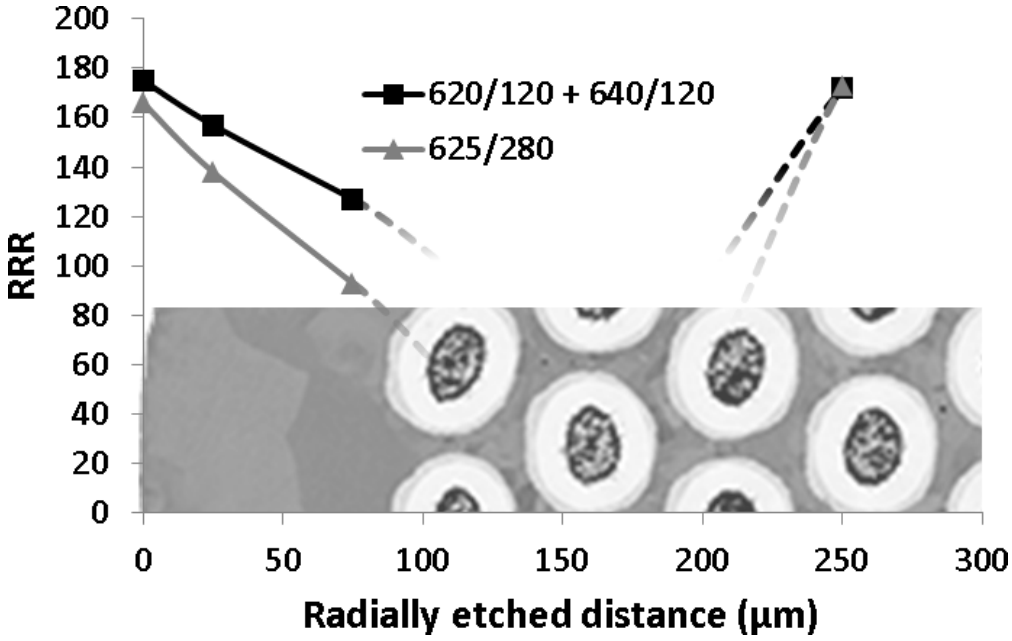

Figure 4.10: *RRR* values as measured after each step of the progressive Cu etch in the two 1 mm wires, with inlay showing the approximate depth the Cu was removed before *RRR* measurement. The heat treatments are listed above the curves. Dashed lines are shown to guide the eye, and indicate a possible RRR profile in the filament pack based on our analysis of where filaments leak.

4.2.2 Effects of the leak zone on J_c

This *RRR* etching experiment clearly showed that the filaments in the outer two rings are most susceptible to barrier breach and leaking Sn. Our hypothesis was that if there are many breaches, the overall J_c should increase by removing the outer filaments, since the most Sn-deficient, and thus lower J_c filaments would be removed from the measurement. The sample used for this measurement was 4.5 cm long, with voltage taps spaced 1 cm apart in the center. Its I_c was measured at applied fields from 12-15 T. After the initial I_c measurement, nitric acid was carefully applied by pipette to the region between the voltage taps. After dissolving some Cu, the most external filaments were broken out of this center region between the voltage taps so that the external filaments did not have a continuous current path along the full sample length, leaving only the inner 3-5 rings intact (Figure 4.11). In fact, the small size of the filaments and their hexagonal symmetry (rather than circular) makes it quite difficult to remove individual rings of filaments, and after the I_c measurement, the sample had to be destructively analyzed to determine how many filaments

participated in the measurement. This was done by metallographic tomography. The sample was mounted in a puck, the surface was polished and then imaged in a light microscope. A total of eight polishing and imaging steps were made, and the sample was polished further down by 0.5-1 mm between each step. Results of the metallographic tomography show the minimum number of filaments along the wire length was 77, this cross-section is superimposed onto the original cross-section for comparison in the right side of Figure 4.12.

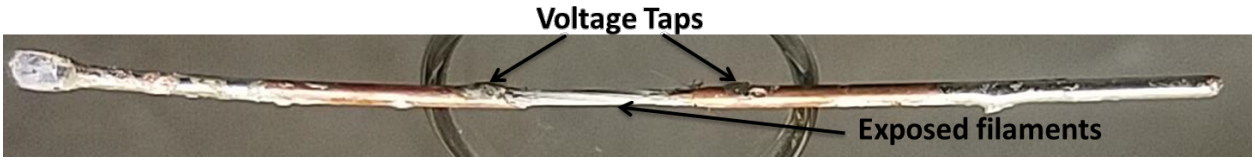

Figure 4.11: A 4.5 cm long sample which has been etched in the center between the voltage taps, in order to remove the outer ring filaments. This sample was 0.78 mm in diameter from billet 32184, and the HT was inverse multistage HT "D" (670/3.5, -5 °C/h, 630/210).

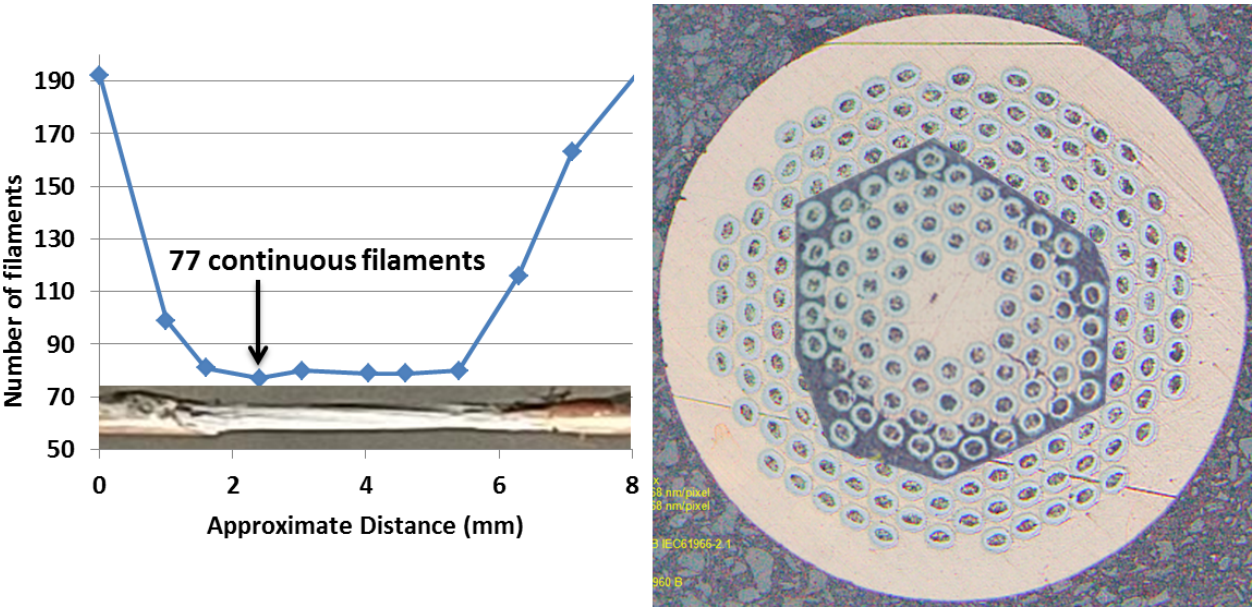

Figure 4.12: On the left, results of the metallographic tomography show the minimum number of filaments along the wire length was 77, this cross-section is superimposed onto the original cross-section for comparison on the right.

The results of this experiment actually showed that the inner filaments had the same J_c within the error of the measurement (Table 4.1). In these wires there may be multiple barrier breaches in a cross section, however, there still tends to be only a few which leak enough Sn to form a Kirkendall void. This sample showed few Kirkendall voids, so the similar J_c agrees with our previous results that A15 production is only affected when a Kirkendall leak forms. In the case where only one or two Kirkendall voids are seen, the overall J_c remains unchanged. For future experiments, it is recommended to perform slower etches that leave filaments fully supported by Cu, as J_c is affected by strain state of the filaments [107], and it is unclear how J_c is affected in the filaments which are not fully supported by Cu after the etch. Furthermore, the transport J_c measured here is only over a length of ~4.5 cm and may not reflect the impact of a random distribution of filament breaches along the length of the wire

Table 4.1: Results of the I_c etching experiment, where we found that J_c is nominally the same comparing the inner 77 filaments and the entire wire with all 192 filaments. J_c is measured over the unreacted filament area.

Sample name	I_c (12 T, 4.2 K)	J_c (12 T, 4.2 K)
B31284 - full wire	493 A	2405 A/mm^2
B31284 - inner filaments	198 A	2408 A/mm^2

4.3 Conclusions of deformation effects on *RRR* and J_c

During wire fabrication, the wide range in mechanical properties of the components of the wire can result in non-uniform deformation and local mechanical instabilities. In these PIT wires we observe that a critical feature of this non-uniformity can be characterized as inward drift of the powder core relative to the center of the Nb-Ta tube. This centroid drift becomes more severe in the outer rings of filaments, providing opportunities for Sn to leak out into the Cu stabilizer on the thinned inner side of the tube. This leaves a large, unused volume of Nb-Ta after the reaction on the thick side. Of these breached filaments, there tend to be a few which breach very early in the reaction and leak enough Sn to form a Kirkendall void. Measurements of the A15 area in each filament show that in general, barrier breaches that are small or occur late in the reaction do not produce a Kirkendall void and no reduction in A15 area was seen. In those few filaments with Kirkendall voids, however, more Sn can be lost to degrade the A15 volume by up to 35%.

Measurements of the variation in barrier thickness revealed that inner rings 1-4 have rather uniform barrier thickness, while rings 5-7 have a large variation in barrier thickness, in some places going to zero. These outer ring filaments then have a thin and a thick side, the thin side then capable of being fully reacted through, which is detrimental for maximizing J_c while maintaining high RRR.

A serial etching experiment was then designed to directly measure the impact of these deformed, leaking filaments on RRR and J_c. The results show that an initial RRR of 175 can fall to a low of 93 when the best Cu is removed. Further removing the Cu surrounding the outer rings 6-7 returns RRR to 175. This demonstrates how even small Sn leaks can substantially degrade RRR. A similar experiment was then made to determine if J_c was impacted by these leaks, the results showing that J_c is largely unchanged if only a few filaments leak enough Sn to show a Kirkendall void.

CHAPTER 5

ANALYSIS OF BUNDLE BARRIER PIT WIRES DESIGNED FOR HIGHER J_C WITHOUT LOSS OF *RRR*.

An argument for substantially increasing the Sn content of PIT cores developed in 2014 when a wire showed an anomalous result during microstructural analysis. While preparing samples for heat treatment, I found that a high temperature weld while sealing the wire ends could alter the local area chemistry near the weld, presumably by locally rearranging the core contents, especially the local Sn content. This provided an opportunity to see how the A15 morphology might vary under different starting conditions without fabricating any new wires. Through examination of cross-sections near the weld we found that an improvement in the amount of SG A15 could be obtained presumably by locally increasing the Sn content in the powder core. Bruker reacted to these results by fabricating a new wire series which had increased Sn in the core. However, to mitigate the anticipated RRR degradation, they protected the outer Cu with a second, so-called "bundle barrier" placed between the filament bundle and the outer annulus of Cu. In this new design, the wire can be reacted without regard to Sn leaks from the filaments since the bundle barrier should protect the external annulus of pure Cu from any Sn contamination. We received nine versions of this new wire, with variations in Sn content, filament number, filament size, and Cu:non-Cu ratio. The best of these wires had filaments with d_{eff} = *36 μm*, a J_c*(12 T, 4.2 K)* of ~2650 A/mm^2, while maintaining a *RRR* of 190. These J_c values are reported over the unreacted filament area, and exclude both the stabilizer Cu and the Nb bundle barrier. The bundle barrier design improved all three major parameters; J_c, *RRR*, and d_{eff}, bringing PIT wires closer to the FCC conductor specifications enumerated in chapter 1. This new PIT wire design showed that the previous PIT design, whether by chemistry or architecture, was limiting the potential of PIT Nb_3Sn.

One drawback to the bundle barrier wire design is that radially, non-uniform deformation occurs during wire fabrication, allowing for more Sn leaks from filaments. Although this is no longer a

RRR issue, leakage outside the filaments imply that we are not using the full potential of these wires because of the reduction to the A15 reaction. However, this also gave an opportunity to better correlate leaks to the deformation parameter of filament/core centroid drift, the main cause and predictor of Sn leaks. Indeed, we found that centroid drift and its associated Sn leaks were quite extensive along the length of the wire. For instance in one case I found that in only a 4 cm length almost half of the filaments present Sn leaks with a Kirkendall void and reduced SG A15 volume. The digital image analysis presented here enables a sophisticated overview of how to explore the true potential of added Sn to raise the J_c of PIT wires.

5.1 Atypical filaments

In this section I will summarize the results obtained on a standard PIT wire that led to the development of the bundle barrier conductor, previously reported in [49]. A possible method of improving the SG A15 amount in Nb_3Sn PIT wires came from a close examination of the 0.78 mm wire heat treated at 630/240 which produced an anomalous result. Typically, wire ends are sealed shut prior to HT by crimping the ends to prevent Sn from leaking out, and any end effects are further avoided by cutting samples from the center of the wire for J_c and metallographic analysis. However, one wire was prepared by welding the ends shut, and after examining a cross-section near the weld, a small fraction (∼10-15%) of distinctly atypical filaments with substantially different microstructure was found, as shown in Figure 5.1 and Figure 5.2. In these atypical filaments, up to 46% SG A15 was found, despite the relatively low reaction temperature. By contrast, the more typical 85% of filaments (typical also of the wires described in chapter 3) generated the more usual 41% SG A15.

The volume fractions of the LG A15 in the typical and atypical filaments were 14% and 10% respectively and the core A15 was also entirely suppressed in atypical filaments, as shown in Table 5.1. Considering the reduction of the LG A15 area, the absence of A15 in the core, the reduced residual DB, and the increased SG A15 volume, it is clear that Sn can be utilized much more efficiently in these atypical filaments.

5.1.1 Discussion

Subsequent analysis of other cross-sections from the same length of wire did not show the atypical filaments, leading us to conclude that their formation was an end-effect in only this particular

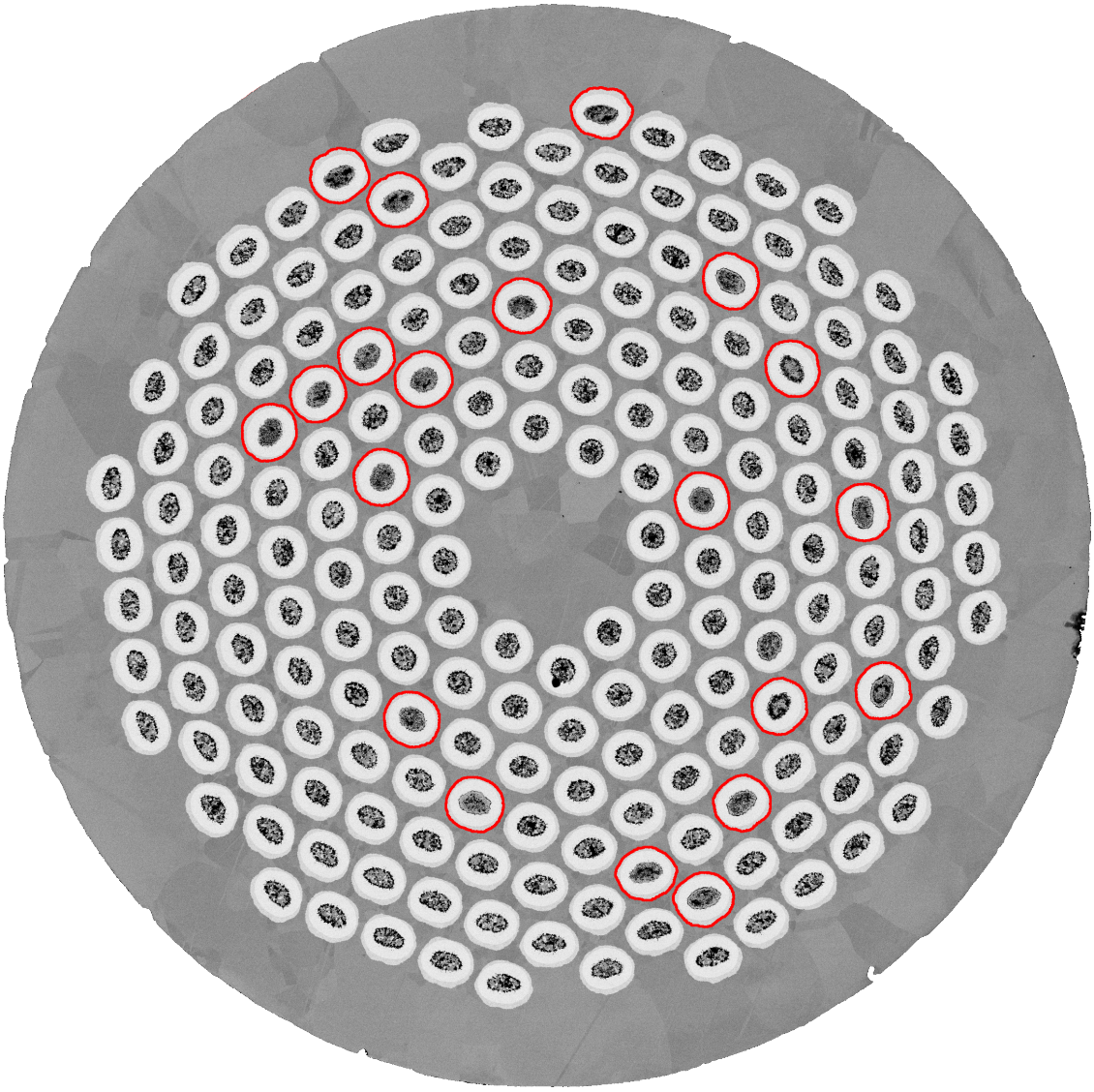

Figure 5.1: FESEM-BSE images of polished, transverse cross-sections of filaments in a 0.78 mm diameter wire whose ends were sealed by welding and subsequently heat treated at 630 °C for 240 h, with 20 atypical filaments outlined in red. The most notable difference at this resolution is the absence of the light-appearing A15 phase in the core.

Table 5.1: This standard design 0.78 mm diameter wire is from billet B31284 with d_{eff} = ~39 μm. The ends were welded shut and near the weld two different filament types were produced with different microstructures.

	Phase or morphology volume %						
Filament type	DB	A15 total	core	core A15	LG A15	SG A15	SG/LG A15 ratio
typical	22.7%	58.1%	19.2%	3.0%	14.4%	40.7%	2.8
atypical	18.2%	56.5%	25.3%	0.0%	10.2%	46.3%	4.5

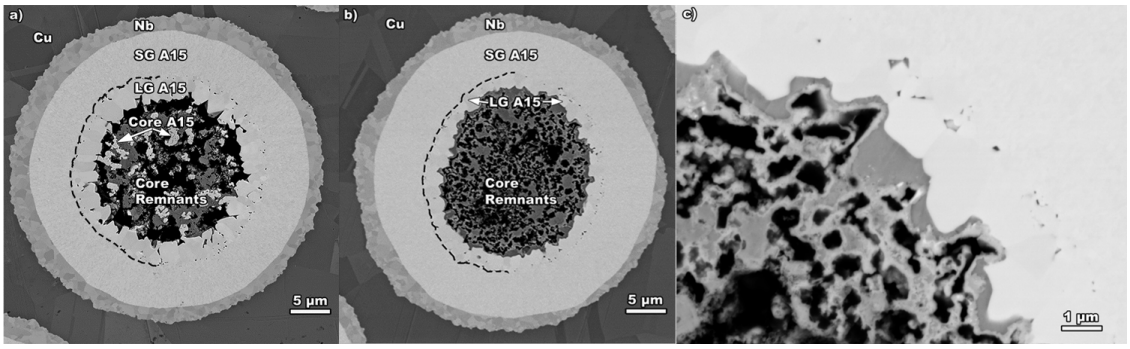

Figure 5.2: FESEM-BSE images of polished, transverse cross-sections of filaments taken from the welded-end of the 0.78 mm wire in Figure 5.1 with HT 630/240, showing typical (a) and atypical (b) microstructure. The atypical filament in (b) has no core A15, a diminished LG A15 area, and an enhanced SG A15 area. An artificial dashed line has been added to better distinguish regions of small and large grain A15 morphologies, in addition, a Cu-rich layer appears (c) which separates the LG A15 annulus from the core remnants in the atypical filament.

welded-end sample. We believe that the high temperature excursion above the melting point of Cu (1085 °C) during end welding acted to rearrange the local area ratios of Sn/Cu/Nb in the core, increasing the Sn content of some filament regions to more favorably form SG A15 by consuming the DB more efficiently.

Since the atypical filaments were generated by the welding of the ends prior to HT, it is not meant to be a practical method to improve wires. However, I thought it might be interesting to repeat the weld and again look to see what different microstructures could arise. After the ends were welded shut, this wire had a HT of 630/94. In Figure 5.3 a menagerie of filaments is produced after the weld, with A15 areas making from almost nothing to about 35% of the filament cross-section. The main driver for repeating this experiment was to show that the local chemistry near

the weld could be favorably altered to improve the SG/LG A15 ratio, as this method is fast and cheaper than forming individual R&D billets with varying Sn-Cu-Nb ratios.

It is interesting to speculate what critical current density a completely atypical wire might develop if the effects of this local temperature excursion could be replicated along the entire length of the wire. A simple estimate suggests J_c could be enhanced by the ratio of the SG fractions $0.463/0.407 = 1.14$, a 14% increase to J_c.

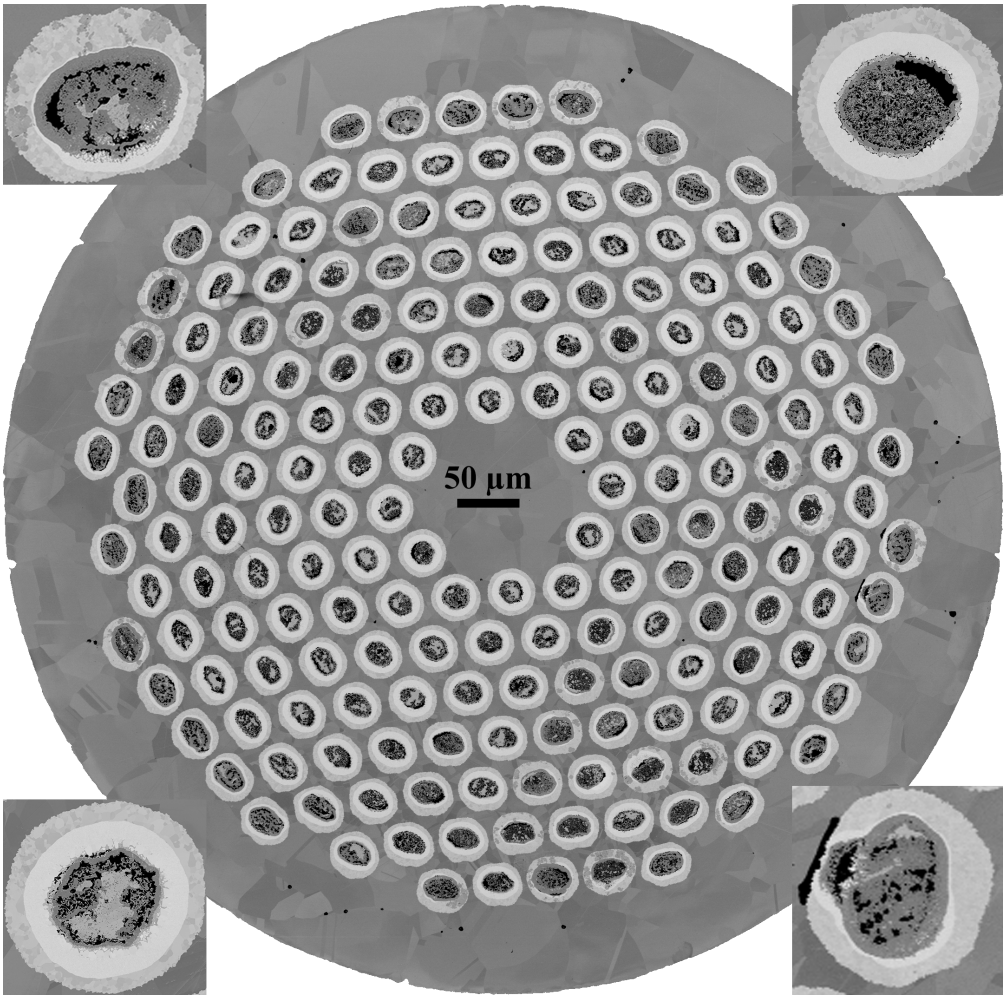

Figure 5.3: FESEM-BSE image of a polished, transverse cross-section of filaments in a 0.78 mm wire with welded ends and a subsequent heat treatment at 630 °C for 94 hours. This cross-section is very close to the welded end to see if high temperature effects from the weld would generate atypical filaments. Here we found that a menagerie of filament types is generated by applying the pre-heat treatment weld. Four select filaments are magnified and inset at the corners of the figure.

5.2 Bundle barrier wires

Stimulated by the atypical filaments described in the previous section, BEAS designed new wires which had increased Sn in the powder core and the addition of a global diffusion barrier that encompasses the filament bundle, so as to maintain a high RRR in the outer annulus of Cu. However, they did not wish to disclose the core compositions, noting only that this pair of wire modifications allowed for more aggressive heat treatments which increased J_c across all samples, while also maintaining a high RRR in most wires. An unexpected result was that the SG/LG A15 ratio fell to a low of 2.3 compared to nearly 3.0 in the previous non-bundle barrier wires. In spite of this increase in the undesired LG A15 fraction, the improved superconducting properties means that the additional Sn improved the quality of the SG A15 layer. However, we found that the addition of the bundle barrier generated a non-uniform deformation in the form of filament size variation and worsened the centroid drift wherein the Sn-rich core drifts from the center of its Nb-Ta reaction tube, often allowing Sn to leak. Unlike previous wire designs, we found Sn leaks can be centimeters long in the bundle barrier wires. With higher Sn in the core and the additional bundle barrier the PIT wire has already shown a substantial J_c improvement, however, the extensive image analysis and electrical property measurements in this chapter will show that PIT Nb_3Sn could see significantly greater gains in performance if this non-uniform deformation could be better managed or controlled.

5.2.1 Electrical and microstructural properties of bundle barrier wires

A major constraint of standard PIT Nb_3Sn wires is that the A15 reaction effectively stops when a filament's diffusion barrier breaches, allowing Sn to leach into the Cu stabilizer where it can no longer be used to form A15. The outer filament rings 6 and 7 are those which breach first, since their filaments have the most centroid drift produced during wire fabrication, as was shown in chapter 4. The longer the reaction proceeds after filaments breach, the more Sn will leak from these filaments, and the lower the RRR will fall. The reaction needs to be stopped when the diffusion barriers of those outer filaments begin to breach if RRR is to be maintained. However, this leaves the less deformed inner ring filaments with unused Sn in the core, and extra diffusion barrier that could have been used to make more SG A15 if the heat treatment had continued.

The method chosen by Bruker to combat these degrading diffusion barriers was to add a secondary diffusion barrier around the filament bundle in addition to the distributed diffusion barriers already surrounding each filament. This global diffusion barrier is similar to many bronze route conductors [108, 109]. The so-called "bundle barrier" contains any leaked Sn, and separates the leaks from the outer annulus of pure Cu so that wires can be heat treated for longer to form the most A15 without regard to barriers breaching and lowering RRR. With this additional diffusion barrier in place, additional Sn can also be added to the filament cores to consume more of the remnant DB to make more A15. Bruker produced ~20 varieties of this "bundle barrier" wire and sent nine wires to the ASC for analysis. All nine of these wires had bundle barriers made of pure Nb, but they varied in their Sn content, filament size, and/or Cu:non-Cu ratio. Additionally, the Cu:non-Cu ratio was altered by varying the Cu content both inside and outside the bundle barrier. The wire cross-sections are shown in Figure 5.4 with their various Sn contents, wire diameters, and sample names.

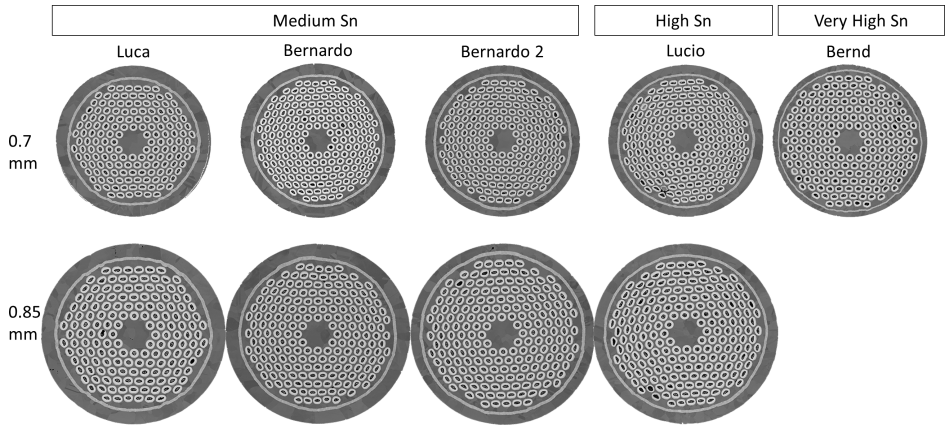

Figure 5.4: FESEM-BSE images of polished cross-sections of bundle barrier wires sent to ASC for analysis. The 0.7 mm wires were reduced in size from the 0.85 mm wires of the same name. The first three wires are medium Sn, Lucio is high Sn, and Bernd is very high Sn.

All bundle barrier wires have higher Sn than those previously mentioned in this dissertation. In this chapter, wires without a bundle barrier may be referred to as 'low-Sn' in comparison to the new bundle barrier designs with increased Sn.

The first group of bundle barrier wires in Figure 5.4 are medium Sn wires (Luca, Bernardo, and Bernardo 2) which have respectively decreasing Cu:non-Cu ratios (1.2, 1.1, 1.0), as well as varying

filament sizes as described in (Table 5.2). Lucio has nominally the same Cu:non-Cu ratio (1.0) and filament size (∼35 μm) as Bernardo 2 , but has a high Sn core. The Bernd wire has the lowest Cu:non-Cu ratio of 0.9 and a very high Sn core. In the Bernd design very little Cu was included outside the bundle barrier. Additionally, Luca has only 156 filaments compared to the standard 192 for all other PIT wire architectures described in this work.

These bundle barrier wires all had the BEAS HT "A" (280/20 + 620/120 + 640/160) with the exception of the 0.85 mm Bernardo which had BEAS HT "N", which differs by a slightly altered first stage of 250/40. They claim that this is nominally the same as the 280/20 stage and should not be regarded as an additional variable in the analysis. The standard PIT comparison wire without bundle barrier in Table 5.2 was from BEAS billet B31284 with a reacted diameter ∼0.78 mm, and a d_{eff} = 39 μm, heat treated for 620/100 + 640/90, the BEAS recommended HT for this wire. The J_c results in Table 5.2 were provided by BEAS and were calculated over the unreacted filament area, excluding the area of the bundle barrier.

Most bundle barrier wires had higher J_c than the standard, lower Sn PIT wires previously described in earlier chapters of this dissertation. In the best case J_c(12 T, 4.2 K) went up to 2658 A/mm^2, nearly a 25% increase, with the $J_{c-layer}$ increasing by more than 25% to over 7000 A/mm^2 in one case (Table 5.2). RRR was maintained above 100 for all wires except Bernd which fell to 61, with the 0.7 mm Luca having a high RRR of 190. As future work on FCC conductors will require higher fields, we include the 15 T data in Table 5.2 for future comparison, noting that the J_c trends between wires are the same for both 12 or 15 T. Luca has the highest J_c, while Bernd has the lowest.

In terms of the microstructure, all wires had increased total A15 volume, which rose from ∼56% to 58-60%. However, the SG/LG A15 ratio declined from 3.0 to 2.3-2.6 range mostly due to the increased LG A15 volume, previously 13-14%, now 15-16% in the bundle barrier wires. (Table 5.3). Additionally, we introduced a new variable into our image analysis and measured the amount of stabilizer Cu which became Kirkendall void (K-void) due to aggressive Sn leaks. While the overall area of Kirkendall voids is low, the correlation of more voids to lower J$_c$ is clear. In the worst wires (Bernd and Lucio), the Kirkendall void fraction is ∼0.35% some seven times that of Luca which had $<$ 0.05% of its Cu cross-section converted to Kirkendall void.

Table 5.2: Bundle barrier wires and their electrical properties. All bundle barrier wires had the HT 280/20 + 620/120 + 640/160 with the exception of the 0.85 mm Bernardo wire which had a different first stage HT of 250/40. The standard wire used for reference here was heat treated with 620/100 + 640/90, previously shown in Table 3.2. All reported dimensions were measured on reacted wires, while all J_c(4.2 K) values were calculated over the unreacted filament area. J_c values for bundle barrier wires were provided by BEAS.

Sample Name	Sample ID	Sn content	Filament Count	Wire d. (mm)	d_{eff} (μm)	Cu: non-Cu	J_c (12 T) A/mm^2	J_c (15 T) A/mm^2	$J_{c-layer}$ (12 T) A/mm^2	RRR
Luca	P2693	med	156	0.71	36.0	1.2	2658	1508	6515	190
Bernardo	P2658	med	192	0.71	33.3	1.1	2561	1462	6308	132
Bernardo 2	P2743	med	192	0.72	34.7	1.0	2455	1389	5859	141
Lucio	P2689	high	192	0.72	35.0	1.0	2434	1363	6257	168
Bernd	P2499	very high	192	0.71	36.3	0.9	2310	1315	5474	61
Luca	P2686	med	156	0.86	44.0	1.2	2640	1488	7021	112
Bernardo	P2656	med	192	0.87	40.5	1.1	2599	1481	6370	127
Bernardo 2	P2736	med	192	0.87	42.1	1.0	2473	1400	6136	131
Lucio	P2683	high	192	0.87	42.2	1.0	2458	1390	6145	109
standard	B31284	low	192	0.78	39.0	1.2	2444	1376	5564	121

Table 5.3: Bundle barrier wires and their microstructural volume fractions and A15 morphology fractions. All bundle barrier wires went through the HT 280/20+620/120+640/160 with the exception of the 0.85 mm Bernardo which had a different first stage of 250/40. The standard wire used for reference here was heat treated with 620/100+640/90. All area fractions refer to the filament area except for the fraction of Kirkendall voids (K-voids), which refers to the % of the Cu stabilizer area which is void.

Sample Name	Sample ID	Sn content	Filament Count	Wire d. (mm)	d_{eff} (μm)	Cu: non-Cu	Total A15	SG/LG ratio	SG A15	LG A15	Core A15	Nb	% K-void
Luca	P2693	med	156	0.71	36.0	1.2	59.2%	2.55	40.8%	16.0%	2.4%	21.0%	0.03%
Bernardo	P2658	med	192	0.71	33.3	1.1	58.6%	2.59	40.6%	15.7%	2.3%	21.7%	0.13%
Bernardo II	P2743	med	192	0.72	34.7	1.0	60.5%	2.64	41.9%	15.9%	2.7%	21.5%	0.27%
Lucio	P2689	high	192	0.72	35.0	1.0	58.1%	2.30	38.9%	16.9%	2.3%	20.9%	0.36%
Bernd	P2499	very high	192	0.71	36.3	0.9	59.0%	2.78	42.2%	15.2%	1.6%	19.9%	0.34%
Luca	P2686	med	156	0.86	44.0	1.2	56.4%	2.28	37.6%	16.5%	2.3%	22.6%	0.04%
Bernardo**	P2656	med	192	0.87	40.5	1.1	59.3%	2.63	40.8%	15.5%	3.0%	21.9%	0.10%
Bernardo II	P2736	med	192	0.87	42.1	1.0	58.8%	2.53	40.3%	15.9%	2.6%	23.0%	0.09%
Lucio	P2683	high	192	0.87	42.2	1.0	59.6%	2.37	40.0%	16.9%	2.7%	20.9%	0.21%
standard	B31284	low	192	0.78	39.0	1.2	56.0%	3.02	40.2%	13.3%	2.5%	23.4%	~0.01%

5.2.2 Discussion of bundle barrier microstructure and electrical properties

These results showed a substantial advance in the J_c(12 T, 4.2 K), setting a new record of 2658 A/mm^2. This is a 6% increase over the previous record J_c(12 T. 4.2 K) of 2,500 A/mm^2 in a 1 mm wire with 50 μm filament diameters. However, the filaments in Luca are only 36 μm in diameter, and it may be more appropriate to compare the J_c with a wire of similar filament size. The best J_c(12 T. 4.2 K) from our 0.78 mm wire with d_{eff} = 39 μm was 2444 A/mm^2. This means in consideration of small d_{eff}, Luca improved the J_c(12 T. 4.2 K) by 9%.

An important distinction to make in bundle barrier wires is how to treat the area of the bundle barrier for J_c calculations. J_c historically refers to a "non-Cu" J_c which has been synonymous with filament area in PIT wires, but now it could also include the additional bundle barrier area in the non-Cu, lowering the value. In this dissertation the J_c is always normalized to the unreacted filament area, disregarding any bundle barrier or stabilizer Cu.

Considering a small d_{eff} after reaction, bundle barrier PIT wires are ahead of the competing RRP wires, as PIT now has a 1508 A/mm^2 (15 T, 4.2 K) with d_{eff} = 36 μm , while RRP has J_c = ~1,400 A/mm^2 (15 T, 4.2 K) at d_{eff} = 35 μm [54].

Although we found a substantial increase in J_c, the mechanism was quite different than we had hypothesized. Since the SG/LG A15 ratio decreased while J_c went up, this implies a big improvement in $J_{c-layer}$, which indeed exceeded 7,000 A/mm^2 at 12 T, 4.2 K in the the 0.85 mm Luca wire, a new record. This is interesting because while we thought the additional Sn would drive a larger SG A15 layer volume (46.3% in the atypical filaments vs 40.7% in the typical), its main effect was to improve the quality of the typical 40-41% SG A15 volume. In fact, the extra Sn does not appear to increase the SG A15 quantity, but it may be that the higher Sn activity drives the SG A15 reaction rate and produces smaller grains. Since improvement was made by adding Sn, we expect to find either smaller grains, A15 closer to stoichiometry, or a more homogeneous A15 layer.

To continue exploring the potential of these bundle barrier wires, we decided to try to further improve the microstructure by increasing the SG/LG A15 ratio using the inverse multistage HT "C" from chapter 3. The results are shown for Luca at 0.85 mm in Table 5.4, where the top row is BEAS heat treatment "A" (280/20 + 620/120 + 640/160), the middle row is inverse multistage HT "C" with an extra 28 hours at 630 °C (690/0, -5 °C/h, 670/0, -10 °C/h, 630/238), and the

Table 5.4: Comparison of HT's for Luca at 0.85 mm. The top row is BEAS heat treatment A (280/20 + 620/120 + 640/160), the middle row is inverse multistage HT "C" with an extra 28 hours at 630 °C (690/0, -5 °C/h, 670/0, -10 °C/h, 630/238). The bottom row shows the substantial improvement to the SG/LG A15 ratio, nearly doubling, while the superconducting properties all degraded. I_c and J_c are reported at 12 T, 4.2 K.

Heat Treatment	I_c (A)	J_c (A/mm^2)	$J_{c-layer}$ (A/mm^2)	Nb%	Total A15%	Core A15%	LG A15%	SG A15%	SG/LG ratio
BEAS HT A	546	2640	7021	22.6	56.4	2.3	16.5	37.6	2.3
Inverted multistage HT C	512	2476	5370	21.1	60.7	3.7	10.9	46.1	4.2
% change from inverted HT	-6%	-6%	-24%	-7%	-7%	+61%	-33%	+23%	+83%

bottom row shows the change from applying the IMHT "C". The most notable change is that the SG/LG A15 ratio nearly doubled from 2.3 in the BEAS HT to 4.2 in our IMHT "C". This was from an increased SG A15 volume which climbed from 38% to 46%, while the LG A15 volume dropped from 16.5% to 11%, raising the overall A15 volume to ∼61% from ∼56%. This SG/LG A15 ratio of 4.2 is very close to the atypical filaments discussed in the previous section which had a SG/LG A15 ratio of 4.5. However, this new wire and HT combination did have 4% core A15, abnormally high compared to the BEAS HT and to the atypical filaments which had no core A15. Unfortunately, the J_c fell by 6% in the IMHT, with the $J_{c-layer}$ falling by 24%. The bundle barrier wires seem to behave the same as the standard PIT wires with respect to the IMHT.

5.2.3 Non-uniform filament deformation in bundle barrier wires and its effect on small grain A15 volume

The increased Sn in bundle barrier wires allows for an A15 reaction which encourages filament breakthroughs. No longer limited by the poisoning of the stabilizer Cu, I see 15-20 filaments with Kirkendall voids in the bundle barrier wires, compared to only a few leaks in previous standard-Sn wires lacking a bundle barrier. The bundle barrier wires gave us an opportunity to more systematically analyze how the diffusion barrier failure occurs. We noted that most of the Sn leaks occur in the outer filaments, the Sn-rich cores in those filaments having drifted far from the center of the Nb-Ta tube containing them. We accordingly analyzed every filament in each cross-section and asked: is the diffusion barrier breached? If yes, has enough Sn leaked to form a Kirkendall void? The results are shown in Figure 5.5, where orange filaments have breached diffusion barriers and A15 is in contact with the Cu stabilizer, and the red filaments denote a breach which leaked

enough Sn to additionally produce a Kirkendall void. There is a clear pattern going from lower to higher Sn wires (left to right), Luca only having a few breaches with Kirkendall voids, while Lucio and Bernd had many (>15 in these cross-sections). Sn leaks large enough to form Kirkendall voids will reduce the volume of A15, and primarily the SG A15 is reduced since the LG A15 layer mostly formed about halfway through an optimized reaction, and barrier breach typically occurs in the latter half of the reaction. With low J_c and many breached and leaking filaments in Bernd, we sought to analyze the deformation, and specifically compare the centroid drift with the Luca wire which had the best J_c and fewest breached or leaking filaments. This section details how the non-uniform filament deformation, evident from core centroid drift measurements, can substantially reduce the SG A15 volume.

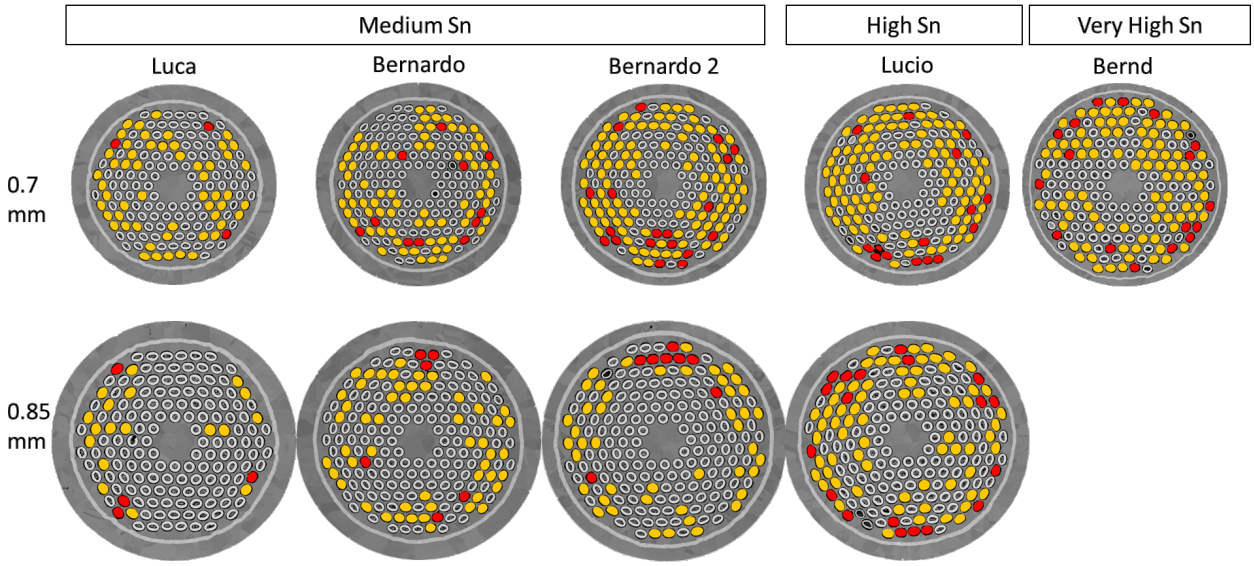

Figure 5.5: FESEM-BSE images of polished cross-sections of bundle barrier wires sent to ASC for analysis, this is a colored version of Figure 5.4. Filaments in orange have A15 in contact with the Cu stabilizer, and filaments in red additionally had a breach severe enough to produce a Kirkendall void.

My first observation was that the filament area can vary by up to 15% within a cross-section in all varieties of bundle barrier wire, the outer filaments being smaller than those closest to the wire center, demonstrated on the 0.85 mm Bernardo wire (Figure 5.6). Summary statistics are shown in the upper left corner. The area equivalent d_{eff} from the data in the color map varied from 38.8 μm in the outer ring filaments, to 41.5 μm in the inner ring filaments. This variation in filament size

causes a number of problems, one of which is that the average area of the filaments in inner rings 1-4 of this cross-section is about 2.5% higher than the average for the entire wire.

When considering that 40.8% of the filament is current-carrying SG A15, preventing the non-uniform area reduction of the outer filaments should increase J_c proportionally to the increase in SG A15 volume, about 1% (2.5%X40.8%). However, this calculation underestimates the effect on J_c because it does not account for how much Sn is lost from leaking outer filaments, even as the inner filaments maintain integrity through the end of the reaction. In Figure 5.7 we apply the same type of color map but now for the A15 area, and find that the A15 area for the inner ring filaments is 3.6% higher than the overall filament average. As only about 1% of the SG A15 and J_c increase comes from the variation in filament size, the remaining 2.6% must arise from preventing Sn leaking out to form a Kirkendall void and reducing the total SG A15 volume. Because an optimized reaction must stop while RRR is still reasonably high (100-150), the reaction length is controlled by breach of the smallest filaments. Protecting them means leaving unreacted Sn and Nb in the larger filaments closer to the wire center. In the example of the 0.85 mm bernardo wier, if the outer filaments could be maintained at the size of the inner filaments, and core drift be reduced enough to prevent Kirkendall voids from forming, the SG A15 volume could then increase from 40.8% to 44.4%.

In summary, this study shows:

1. Smaller filaments in the outer rings reduce the overall SG A15 area by 1%
2. Sn leaks in these smaller outer filaments further reduce the SG A15 by 2.6%
3. The reaction heat treatment must be limited to that which does not breach the smallest filaments to ensure RRR is maintained, wasting Nb and Sn in the larger filaments

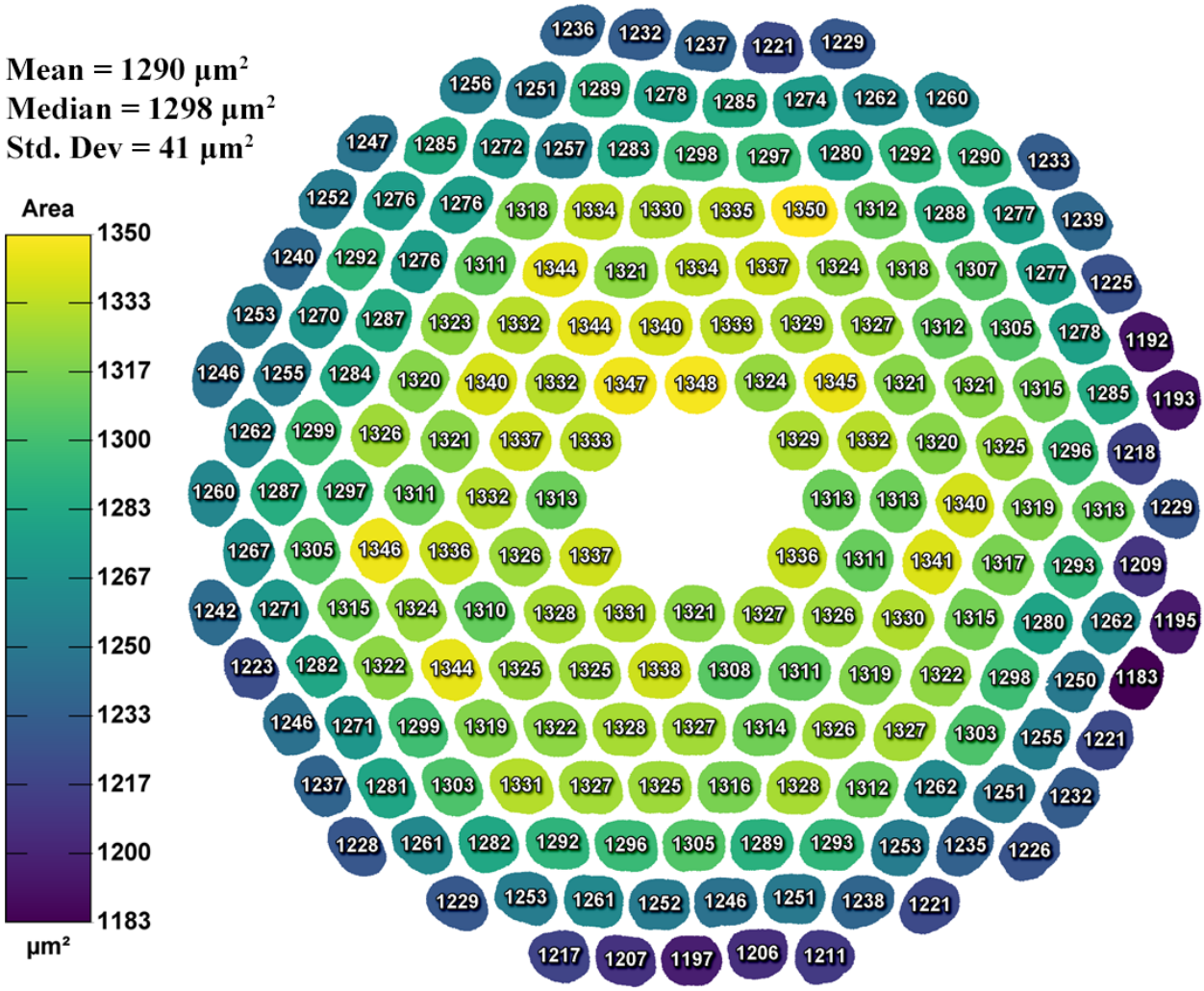

Figure 5.6: Bundle barrier wire Bernardo, 0.85 mm in diameter, colored by reacted filament area. The inner most filaments are the largest (largest area 1350 μm^2), while the area fell to a low of 1183 μm^2 in the outer filaments. Summary statistics are shown in the upper left corner. The mean area of 1290 μm^2 corresponds to a d_{eff} = 40.5 μm.

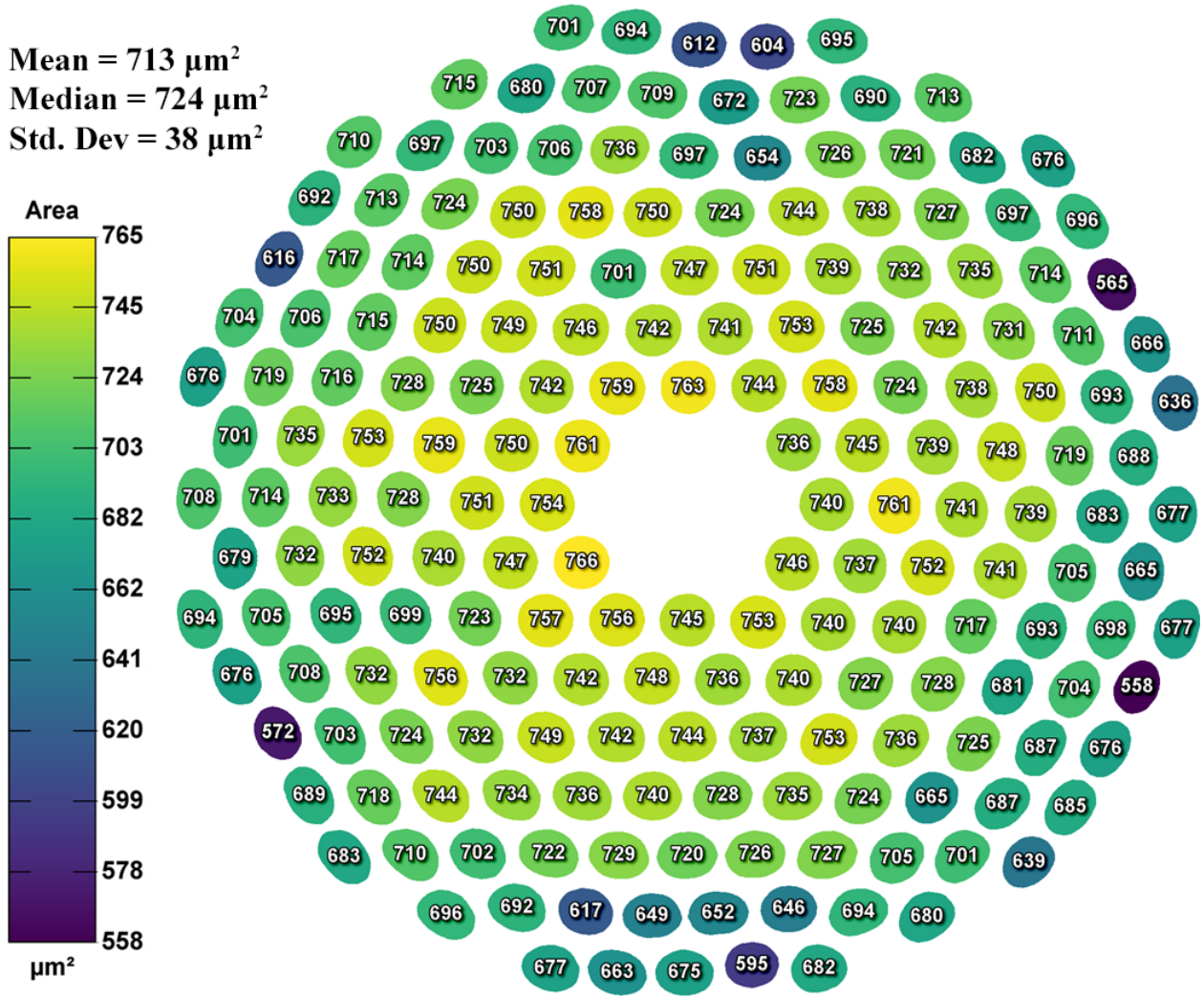

Figure 5.7: Bundle barrier wire Bernardo, 0.85 mm in diameter, colored by SG+LG A15 area to show the radial dependence. The inner most filaments have larger A15 areas up to 765 μm^2 while the area fell to a low of 558 μm^2 in the outer filaments. Summary statistics are shown in the upper left corner, which show a mean A15 area of 713 μm^2.

5.2.4 Filament centroid drift and its correlation to barrier breach

As with the previous generation of non-bundle barrier wires, the cause of diffusion barrier breach is the centroid of the porous, Sn-rich core drifting from the center of its Nb-Ta reaction tube. Here we look at two examples of how centroid drift can affect A15 production. In the bundle barrier wire with highest J_c (Luca at 0.7 mm diameter), there were only two breaches severe enough to form a Kirkendall void in the analyzed cross-section (Figure 5.8), and these leaks occur in filaments with the high centroid drifts of 4.2% and 3.8%. These two filaments are annotated in red throughout the figure. To the left of the cross-section are the five filaments with highest centroid drift, including the two showing Kirkendall voids. The bottom left plot shows the radial dependence of centroid drift, the yellow data points show a local average for each ring of filaments. The bottom right plot shows how the SG+LG A15 area fraction is affected by centroid drift; the two filaments with Kirkendall voids both have substantially reduced A15 volume (data points in red). The key conclusion is that centroid drift causes barrier breach. When enough Sn leaks out to form a Kirkendall void, the A15 area is significantly depressed. To develop some statistics about how likely filaments are to leak, we arbitrarily considered 3% centroid drift as a critical point, beyond which filament degradation is much more likely. In the Luca wire, 8 filaments were beyond this point, and two of them formed Kirkendall voids, a 25% leak rate for filaments beyond 3% normalized centroid drift. Additionally, if we consider the stabilizer Cu, about 0.03% of its volume became Kirkendall void. The volume of Kirkendall voids is a good marker for how severe a filament leaked, and also that the A15 area will be reduced in that filament.

The same analysis was performed on the worst bundle barrier wire (Bernd), and the results are shown in Figure 5.9. Two filaments had very high centroid drift, 5.3% and 4.2%, annotated in red throughout the figure, and 3 out of the 5 worst filaments shown to the left of the cross-section showed Kirkendall voids. In the bottom left plot, the radial dependence of centroid drift is seen, the yellow points representing local averages for each ring of filaments. Again, the filaments with the highest centroid drift are the two which leaked the most. In the bottom right plot we see that the dependence of A15 volume on centroid drift shows that the greater the Sn-rich core drift, the more likely it is to breach and leak Sn. Bernd had 17 leaks in this cross-section (red data points), many more than the two of Luca. In the Bernd wire, 25 filaments had their cores drift beyond 3%, and 6 of them formed Kirkendall voids, a 24% leak rate. As Luca also had a leak rate of 25%

beyond the 3% criterion, these data validate the 3% centroid drift criterion as a reasonable marker for leakage.

The filament in the inset of the bottom right of Figure 5.9 shows an interesting anomalous filament which has very little A15 and a core drift of just over 3%. Despite the lack of Kirkendall void in this cross-section, the reduced A15 area suggests that this filament must have leaked further up or down the wire to explain the absence of so much of the core Sn. This made us consider whether there might be many more filaments which are compromised along the length, beyond what we see in a single cross-section.

This positional variation of centroid drift suggests that if the filament cores can not be prevented from drifting, it might be beneficial remove the bundle barrier and stack standard Sn-cores in the external filaments, with enhanced Sn filaments only in the inner rings.

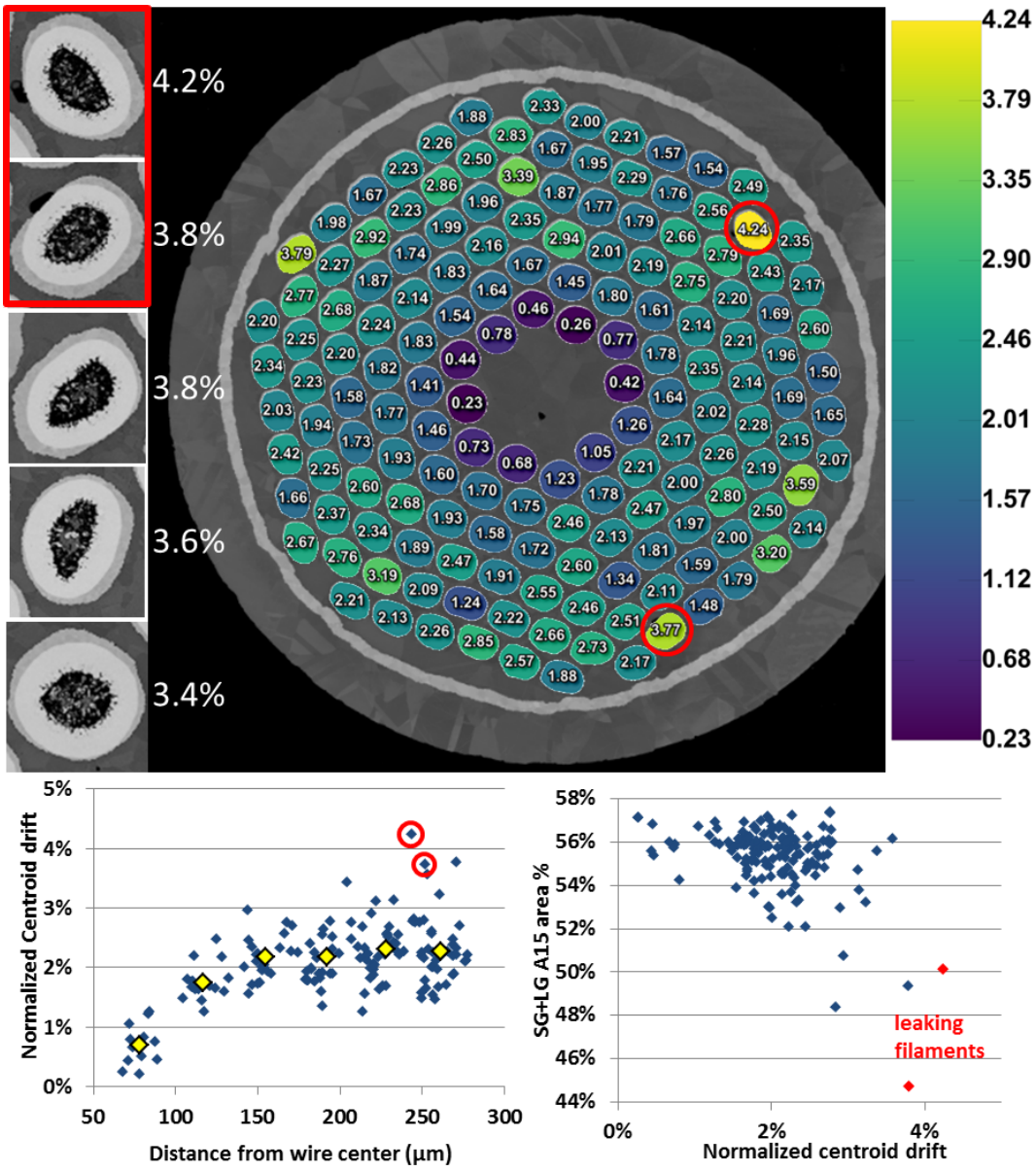

Figure 5.8: Top: bundle barrier wire Luca (0.7 mm diameter) colored by normalized centroid drift as indicated by the color bar to the right of the wire cross-section. Only two filaments leaked, labeled in red throughout the figure. The five filament cross-sections on the left are those with the highest centroid drift. The lower left plot shows the radial dependence of the centroid drift, the yellow points representing local averages for each ring of filaments. The two filaments with high centroid drift are the same two which are shown leaking in the color map. The bottom right plot shows how the SG+LG A15 area fraction is affected by centroid drift, the two filaments with Kirkendall voids have substantially reduced A15 volume.

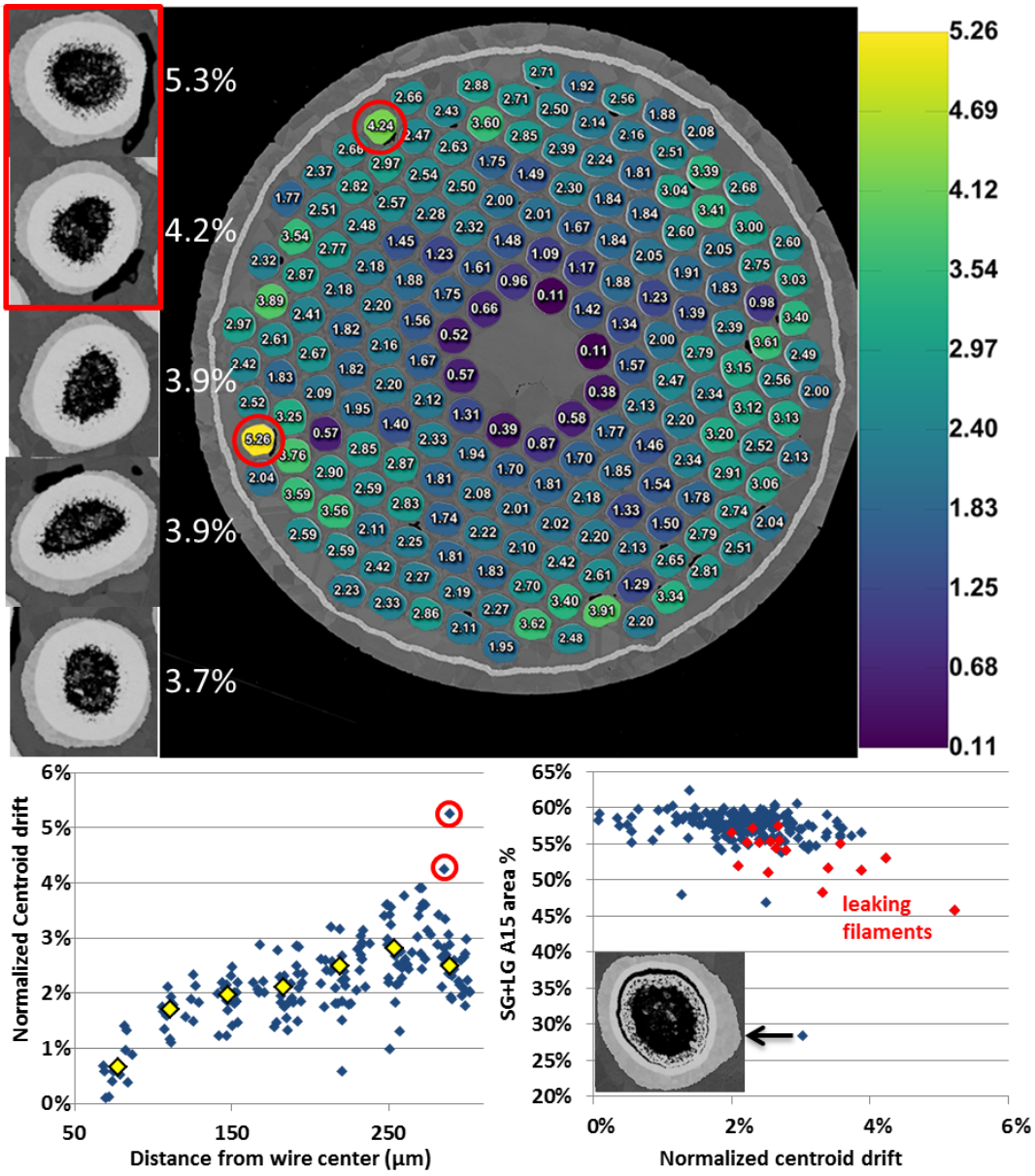

Figure 5.9: Top: bundle barrier wire Bernd (0.7 mm diameter) colored by normalized centroid drift as indicated by the color bar to the right of the wire cross-section. The two filaments with highest centroid drift are circled in red throughout the figure, and all filaments with Kirkendall void are red in the lower right plot. Three out of the five worst filaments to the left of the cross-section present Kirkendall voids. The lower left plot shows the radial dependence of the centroid drift, the yellow points representing local averages for each ring of filaments. The two filaments with highest centroid drift are the same two which are shown leaking in the color map. The bottom right plot shows how the SG + LG A15 area fraction is affected by centroid drift, 17 filaments show Kirkendall voids, many with substantially reduced A15 volume. The filament inset shows an interesting filament which has very little A15 and a core drift of just over 3%. Despite the absence of Kirkendall void in this cross-section, the reduced A15 area means this filament must have leaked further up or down the wire.

5.2.5 Evidence for lengthwise Sn leakage due to centroid drift

To determine the extent of filament degradation along the wire length, we used a technique of metallographic tomography. In this method, we took a 4 cm length of wire and made eight cross-sections by cutting every 5 mm, mounting them in a conductive puck for imaging in the SEM. We chose 4 cm because it is approximately twice the length of the wire twist pitch. If more detailed metallography is needed, the puck can be easily polished down in ∼0.5 mm increments to get additional images. In Figure 5.10 we show a subset of filaments in the Bernd 0.7 mm wire that show how one particular filament changes over 4 cm. This wire was heat treated with BEAS HT A (280/20 + 620/120 + 640/160).

In image A, the filament is severely compromised with substantial Sn loss and a large Kirkendall void: the A15 area clearly diminished. In panels B and C, the diffusion barrier has breached, however, there is no Kirkendall void and the A15 area appears full. In panel D, there is a large Sn leak with a Kirkendall void over 10 μm wide, and only a thin discontinuous A15 layer in the core. In panel E, the diffusion barrier appears fully intact with a full A15 area. In panels F and G, the filament diffusion barrier is entirely breached, with essentially no A15, and large Kirkendall voids tens of microns wide. In panel H, this breach appears contained, with a thin, continuous ring of A15 present. With the considerable damage along the length and the lack of current sharing between PIT filaments, this wire may have many fewer filaments participating in transport than intended, or at least filaments which are participating in a diminished capacity.

To better understand filament continuity along this 4 cm sample of the Bernd wire, we integrated the data from all eight images to measure the frequency that each barrier breached over this length. This is simply counting the filament as either broken, or broken with a Kirkendall void in each cross-section. In total there were 81 filaments which breached and leaked enough Sn to form a Kirkendall void over 4 cm, with the majority of leaks occurring in the outer ring filaments (Figure 5.11). One filament was broken and leaking in 6 out of the 8 cross-sections examined, while many more still leaked in 4 or 5 cross-sections, diminishing the SG A15 volume in these filaments over centimeters. The key conclusion is that individual filaments are unlikely to carry the same current. Moreover, the outer ring filaments with many regions of reduced SG A15 volume contain bottlenecks within the filament which must lower the overall J_c of the wire.

If we now consider any filament whose diffusion barrier breaches (whether or not sufficiently serious to produce Kirkendall voids), a clear pattern emerges in which the inner ring of filaments rarely breach, while many filaments in the outer rings are compromised over the entire 4 cm length. Considering all 192 filaments over 8 cross-sections in Figure 5.12, 170 out of the 192 filaments had at least one cross-section where the A15 made contact with the stabilizing Cu. Moreover, 25% of the filaments breached in at least 6 of the 8 cross-sections. The key conclusion here is that if only 20 filaments out of 192 retain a fully continuous diffusion barrier RRR will be degraded, as only one or two breached filaments can degrade RRR below 100 for conductors without a global, bundle barrier. These tomographic results suggest the value of considering a dual-quality filament stack, where only the inner ring filaments have enhanced Sn, while the outer ring filaments have standard Sn.

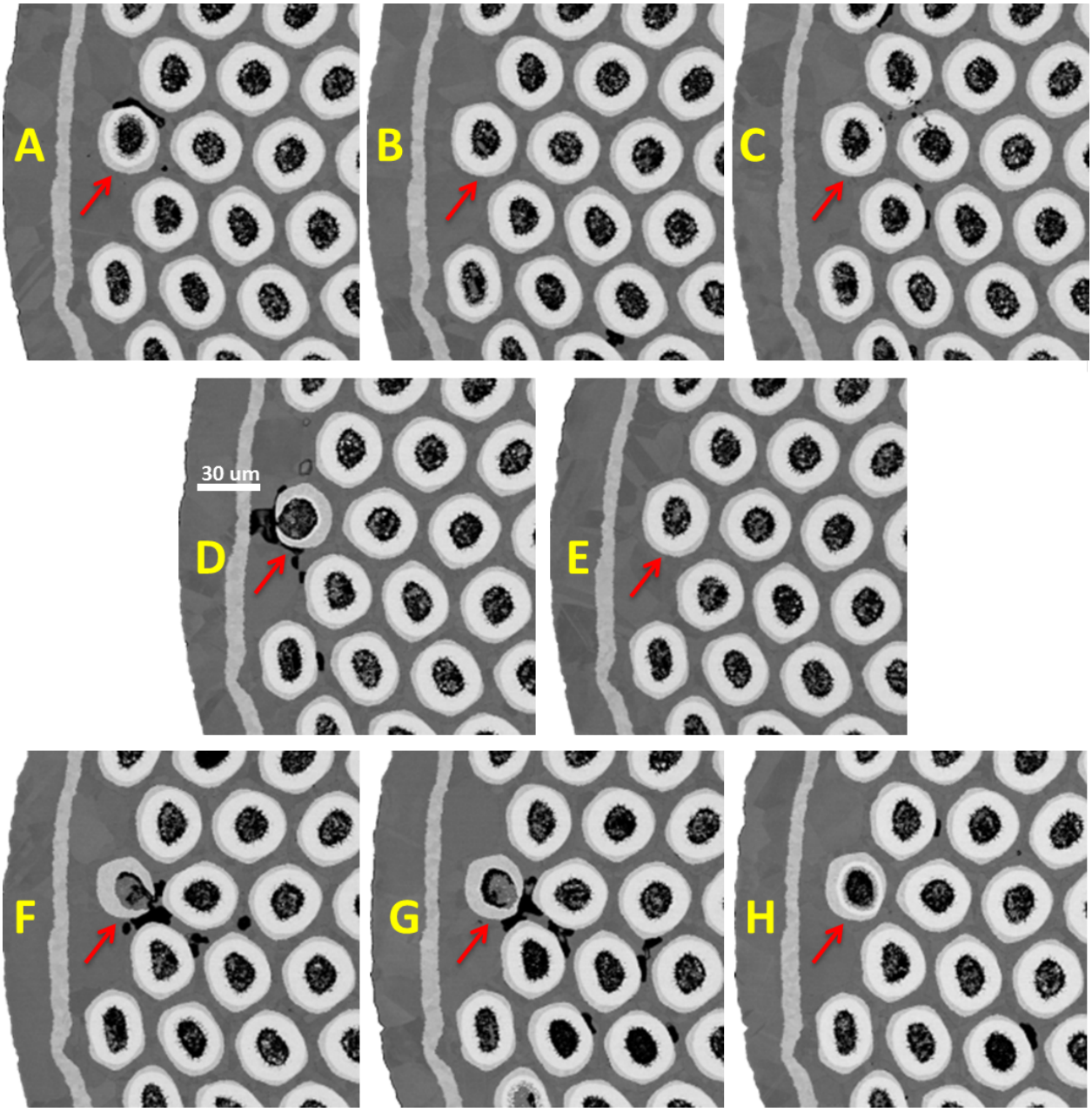

Figure 5.10: This metallographic tomography was made over eight cross-sections, each subsequent panel being separated by 5 mm along the wire length. The wire is Bernd with BEAS HT A (280/20 + 620/120 + 640/160). Each panel (A-H) shows the same sub-set of filaments and the red arrow points to a particularly interesting filament which is severely damaged in cross-sections A, D, F and G, but appears intact in B, C, E, and H.

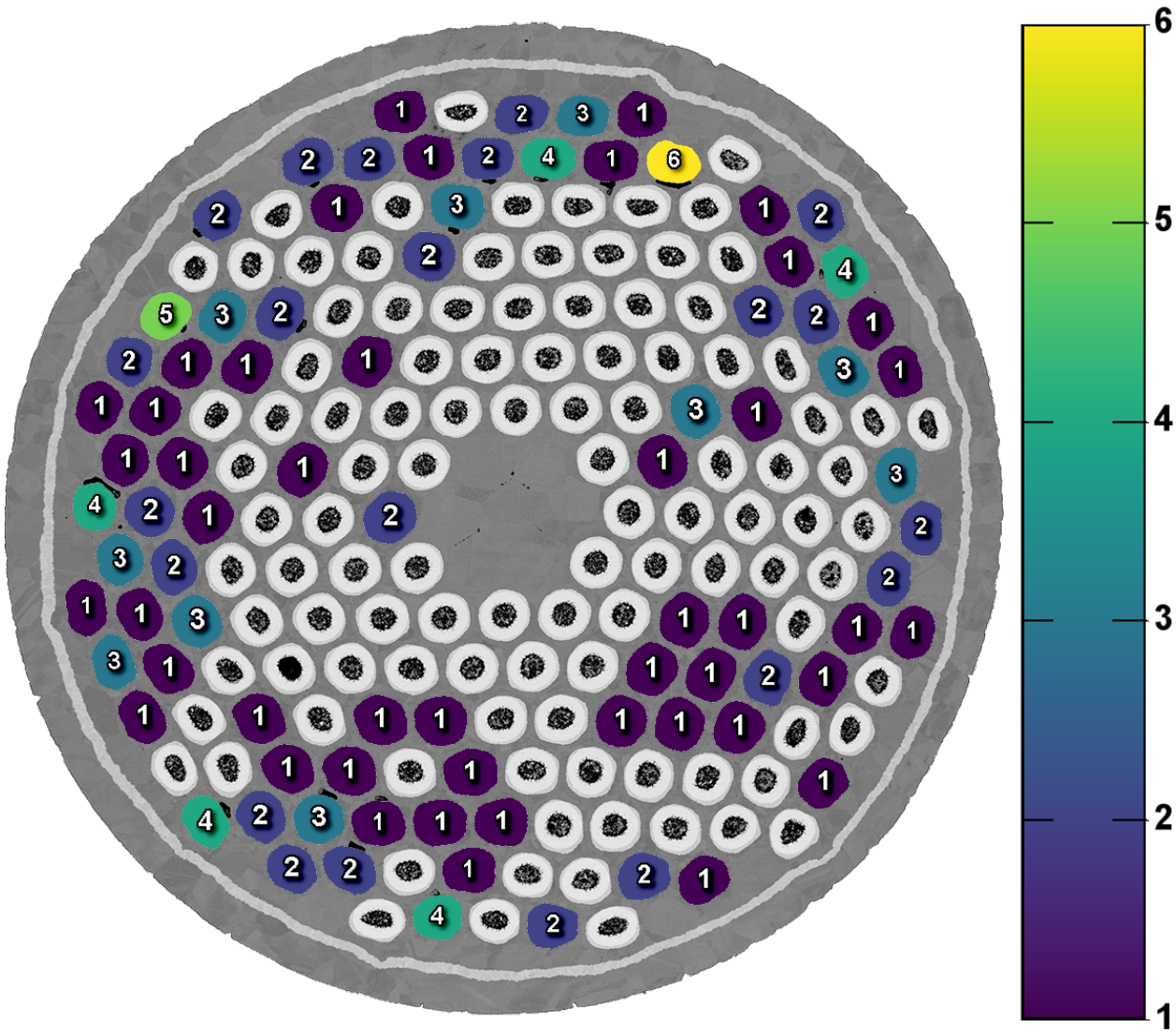

Figure 5.11: Bundle barrier wire Bernd with diameter 0.7 mm, heat treated with BEAS HT A (280/20 + 620/120 + 640/160). Each filament is colored and labeled by the number of cross-sections in which the filament breached and leaked enough Sn to form a Kirkendall void. Over the 4 cm long sample there were 15-20 leaks in each of the eight cross-sections, and a total of 85 unique filaments leaked enough Sn to form a Kirkendall void. The worst filament leaked in 6 of the 8 cross-sections.

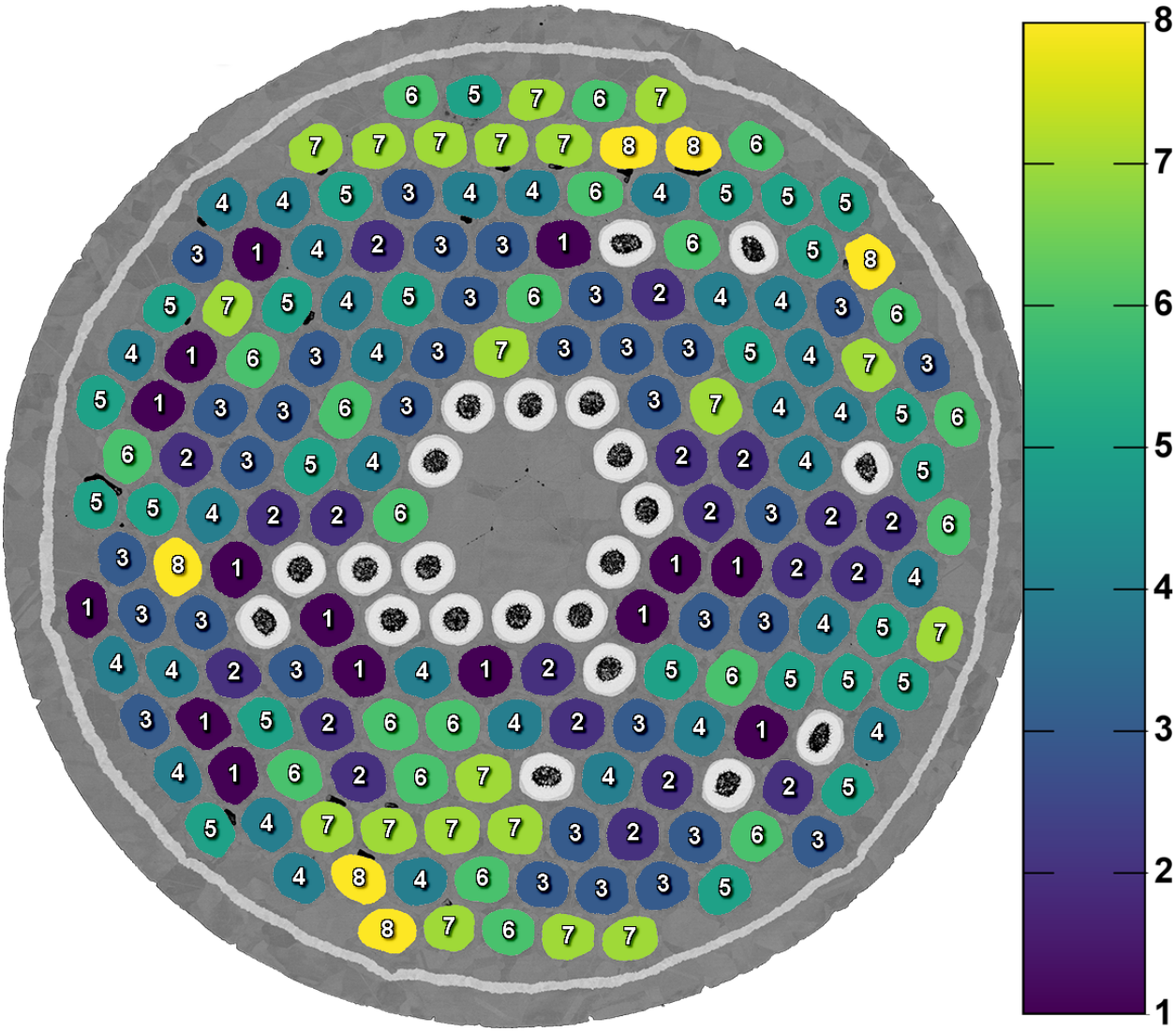

Figure 5.12: Bundle barrier wire Bernd with diameter 0.7 mm, heat treated with BEAS HT A (280/20 + 620/120 + 640/160). By integrating the data from our metallographic tomography across eight cross-sections along the 4 cm length, we can color each filament by its frequency of barrier breach. 170 out of the 192 filaments had their A15 make contact with the Cu stabilizer.

5.3 Conclusions and future work for bundle barrier wires

Our observation in 2014 of the increased SG A15 volume after welding standard design wires led to a proposal to develop wires with increased Sn in the filament cores. BEAS made ∼20 wires (sending us 9) with increased Sn, but they also added a second, bundle barrier to protect an outer annulus of Cu so as to maintain high *RRR*. The best bundle barrier wire set a new 12 T J_c record for PIT wires of 2658 A/mm^2, nearly a 10% improvement over the 0.78 mm diameter wire of comparable filament size (39 μm) which had a J_c(12 T, 4.2 K) of only 2444 A/mm^2. This same bundle barrier wire had a J_c of 1508 A/mm^2 (15 T, 4.2 K) and, putting PIT ahead of the best RRP wire of comparable filament size which has J$_c$ = 1,400 A/mm^2 with d$_{eff}$ = 35 μm. Since the volume of SG A15 did not increase in the bundle barrier wires, our conclusion is that the higher Sn content generated a higher quality of A15, either by smaller grain size, being closer to stoichiometry, or by creating a more uniform distribution of Sn [110].

The SG/LG A15 ratio in the bundle barrier wires was lower than in previous wires because the higher Sn produced more LG A15. Accordingly, we tried to increase the SG A15 volume by using our inverted multistage HT "C". Indeed, we were successful in raising the SG A15 from 40% to 46% and reducing the LG A15 from 17% to 11%, but none of this successful microstructural morphology engineering benefited either the J_c (12 T, 4.2 K) which fell from 2640 to 2480 A/mm^2 (at 12 T) nor the $J_{c-layer}$ which dropped from 7021 to 5370 A/mm^2. We infer that the initial 670-690 °C HT stage degrades the A15 grain size and vortex pinning, however beneficial it is for the SG/LG A15 ratio.

In addition to the superconducting properties, we measured how non-uniform deformation during wire fabrication affected filament centroid drift. The most noticeable difference with the addition of the bundle barrier is that the filament area decreased by ∼14% going radially outward from the wire center. Additionally, the centers of the Sn-rich cores drifted from the center of their Nb-Ta tubes which provided opportunities for Sn to leak. We focused on comparing the wire with the best superconducting properties (Luca) to the worst wire (Bernd), both at 0.7 mm wire diameter, and $d_{eff} \sim 36$ μm. The filaments with highest centroid drift are substantially higher in bundle barrier wires, especially those with lower Cu:non-Cu (such as Bernd). Our conclusion is that the Cu provides a cushion between the filament bundle and the die wall during wire fabrication, allowing the Nb-Ta tube and porous, Sn-rich cores to co-deform more favorably.

In filaments which had centroid drift >3%, about 25% of the diffusion barriers visible in any one cross-section breached and leaked enough Sn to form a Kirkendall void, diminishing the volume of SG A15 which could be formed. To further explore this damage, I then measured multiple centimeters of wire by metallographic tomography, in which a 4 cm sample was imaged at eight cross-sections 5 mm apart. We found that the wire Bernd had ∼10% of its 192 filaments showing Kirkendall voids, Sn leaks, and reduced A15 areas in a given cross-section along the wire length. This means that many of the filaments are only partially participating during current transport, since their A15 areas are significantly diminished. Additionally, we found only 10% of the filaments have fully intact barriers over an entire 4 cm wire sample, with 25% of filaments being breached for nearly the entire 4 cm long wire sample.

The ultimate recommendation coming from the work of this chapter would be to further increase the Cu:non-Cu ratio in a wire of the Luca design and make the core 'very high' Sn as opposed to medium Sn. The additional Cu stabilizer would reduce core centroid drift, and the additional Sn, which now does not escape the reaction tube, could be used to form more SG A15 or otherwise improve the A15 layer. If core centroid drift can not be prevented, it may be beneficial to have a wire made of dual-quality filaments, with high Sn filaments in the inner rings, and standard Sn in the outer rings. This would allow the best filaments to fully react, and avoid the most deformed filaments from leaking Sn and lowering RRR. Additionally, there have been past suggestions to add Cu to the core as well so as to reduce the LG A15 volume, and improve the SG/LG A15 seen in the welded-end atypical wires. However, this added Cu always comes at the cost of a reduction in starting Sn volume, and therefore produces less overall A15, and lower J_c [94, 111, 112]. At this time, the most clear direction to improve J_c and RRR would be to prevent this centroid drift. The irony here is that if centroid drift is sufficiently minimized, the bundle barrier may no longer be needed since the Sn can be better contained to the Nb-Ta reaction tube.

CHAPTER 6

CONCLUSIONS AND FUTURE WORK

Prior to the work presented in this dissertation, Powder-In-Tube process Nb_3Sn wire technology had evolved only slowly in the last 15 years, steadily being overtaken by the more flexible, cheaper, and more reproducible RRP process. The best conductor manufactured at long lengths had been a 1 mm diameter wire with $d_{eff} = 50$ μm, a non-Cu J_c of 2,500 A/mm^2 (12 T, 4.2 K), and a RRR of 175. This same wire converted 58% of the non-Cu cross-section into A15 phase, with 41% converted to the desirable, current-carrying SG A15. All of these values were substantially lower than the leading competitor, the Rod Restack Process which exceeded 3,000 A/mm^2 (12 T, 4.2 K), RRR > 350, and a non-Cu A15 area of 60% (nearly all SG A15) [69]. To determine what was holding PIT back from the high J_c seen in RRP wires, we performed detailed microstructural analysis of the phase evolution in PIT wires from room temperature up to the A15 reaction above 600 °C. This revealed a complex reaction pathway:

$$NbSn_2 + Cu \rightarrow (Nb_{0.75}Cu_{0.25})Sn_2 \rightarrow NbSn_2 + Cu_x \rightarrow Nb_6Sn_5Cu_x \rightarrow Nb_3Sn(LG) + Cu_x + Sn \quad (3.2.2)$$

A critical part of this pathway is the formation of Nausite ($(Nb_{0.75}Cu_{0.25})Sn_2$) which ultimately transforms to the undesired LG A15 phase. I explored some possibilities of suppressing this Nausite phase with no success; my results show that the more time spent under the A15 reaction temperature, the larger the Nausite layer would grow.

I found that once the A15 reaction begins, SG A15 always forms before the LG A15, with the rate of formation increasing with reaction temperature. I also found that the layer thickness of the SG A15 when the LG A15 started to form was strongly dependent on temperature. This led me to perform a set of furnace pull-out experiments to better understand how SG and LG A15 evolve in the early hours of different isothermal heat treatments.

These results stimulated a new type of inverse multistage heat treatment which first ramps the wire to a high temperature in the 670 - 690 °C range before slow cooling at 5 - 20 °C/h to a final

isothermal A15 reaction temperature of 630 °C. Four such inverse multistage heat treatments were designed and the volume of SG A15 increased in all cases while also suppressing the LG A15, driving the SG/LG A15 ratio from 2.8 in a typical HT to a high of 3.9 in the best inverse multistage heat treatment. Unfortunately, the high temperature stage reduced the grain boundary vortex pinning in the SG A15 layer, and non-Cu J_c was diminished by about 2%. Many experiments on both standard and bundle barrier wires failed to produce an overall J_c benefit, even though I was able to increase the SG A15 fraction from about 40% to 44%.

Bruker was stimulated by our experiments which showed the potential of increasing the Sn in the filament cores to increase the SG A15 volume and drive up J_c. Bruker then manufactured a new generation of PIT wire with increased Sn in the core and a second diffusion barrier, which surrounds the filament bundle to mitigate the increased risk to RRR degradation. These "bundle barrier" wires outperform all previous Nb_3Sn PIT wires, with the best performing wire having a filament J_c(12 T, 4.2 K) of 2658 A/mm^2, RRR = 190, and d_{eff}=36 μm. The major constraint in this new wire design, however, is the substantial degradation of the filament size and round filament shape moving from the filaments closest to the wire center to the outer filaments. Our thorough digital image analysis techniques showed that filaments vary in size depending on their radial position in the wire, making it difficult to optimize a heat treatment. Additionally, in the worst wire, 170/192 filaments breached their barriers along a 4 cm length of wire, with many filaments leaking enough Sn to form Kirkendall voids and diminish the SG A15 volume. We measured how likely a filament was to breach by measuring how far the centroids of the Sn-rich core and Nb-Ta reaction tube have drifted from each other, as this creates a thin side of the diffusion barrier. We found that there is a 25% chance of a filament breaching and producing a Kirkendall void if the normalized centroid drift is beyond 3%. This is a strong validation of the need to control the non-uniform deformation during wire fabrication to keep the Sn in the reaction package, and out of the Cu. Additionally, if the non-uniform deformation is reduced, the bundle barrier would no longer be needed to maintain a high RRR.

6.1 Suggestions for future work to improve Nb_3Sn PIT wires

6.1.1 Improvements to bundle barrier architecture and chemistry

Our analysis showed that the non-uniform deformation imposed on the filaments during wire fabrication is what allows Sn to leak from the filaments. The Sn leakage lowers *RRR* and also reduces the volume of SG A15. The Luca wire had the most uniform filament bundle with the fewest Kirkendall voids, and the highest J_c. We suggest that its larger Cu:non-Cu ratio, specifically the large volume of Cu *outside* of the bundle barrier, provides a cushion to the die wall, allowing more uniform co-deformation of the porous, powder core and the Nb-Ta reaction tube. The worst performing wire was Bernd which had the least external Cu, further consistent with our explanation of the good properties of Luca. As this deformation is improved, and the threat of Sn leak abates, it would make sense to increase the Sn content of the core up to the very-high level utilized in Bernd. This very-high Sn core improvement was not fully manifested in the Bernd wire due the more severe deformation which allowed substantial amounts of Sn to leak from the reaction tubes, hardly "very high Sn" after the leaks.

If core centroid drift can not be mitigated, it may be beneficial to have a wire made of dual-quality filaments, with high Sn filaments in the inner rings which can fully react to over 60% A15 volume without breaching diffusion barriers, and standard Sn in the outer rings. These more deformed outer ring filaments with standard Sn would then reach a complete reaction well before barrier breach and maintain high RRR.

Additionally, there have been suggestions in the past to add Cu to the core as well to reduce the LG A15 volume and to improve the SG/LG A15 ratio as seen in the atypical wires. However, this added Cu always comes at the cost of a reduction in Sn volume, and therefore produces less overall A15, or A15 which is Sn deficient, lowering J_c [94, 111]. At this time, the more clear direction to improve J_c and *RRR* would be to prevent centroid drift. The irony here is that if centroid drift is sufficiently minimized, the bundle barrier may no longer be needed since the Sn can be better contained within the Nb-Ta reaction tube and *RRR* would not degrade.

6.1.2 Artificial Pinning Centers (APC)

One possibility of improving Nb_3Sn PIT conductors is through artificial pinning centers which have been shown to enhance J_c by 60% in irradiation studies which induced point pinning centers

[113]. The essential result is that radiation adds point-pinning centers, leading to an increase of the maximum volume pinning force and shifting the pinning force peak to higher fields. Although this method is of course not suitable for engineering pinning centers as the conductor becomes radioactive, it shows the value and potential of artificial point-pinning.

Recently, multiple groups have reported on the development of engineering artificial pinning centers (APCs) in multifilamentary Nb_3Sn superconductors by a PIT technique of internal oxidation [114, 115]. In this approach, a Zr-alloyed Nb tube is filled with a powder made of η (Cu_6Sn_5) and SnO_2 powders. During the heat treatment, Zr oxide nano particles form acting as a dispersion of APCs. Results recently reported out of the Applied Superconductivity Center show a successful grain size refinement down to $\sim$38 nm from the 90 - 130 nm presented in this thesis [114]. If the desire is to increase pinning and operate in higher fields up to 16 T, an APC PIT approach appears to be compatible.

BIBLIOGRAPHY

[1] H Kammerlingh Onnes. "Akad van Wetenschappenn (Amsterdam), 14 113". *Commun. Phys. Lab. Leiden, 120b, 124c* (1911).

[2] H Kamerlingh Onnes. "The liquefaction of helium". *Koninklijke Nederlandse Akademie von Wetenschappen, Proceedings* 11 (1908), pp. 1908–1909.

[3] H Kammerlingh Onnes. "Akad van Wetenschappenn (Amsterdam), 16 113". *Commun. Phys. Lab. Leiden, 133d* (1913).

[4] Dirk van Delft and Peter Kes. "The discovery of superconductivity". *Physics Today* 63., no.9 (Sept. 1, 2010), pp. 38–43.

[5] W. Meissner and H. Franz. "Messungen mit Hilfe von flüssigem Helium. VIII. Supraleitfähigkeit von Niobium". *Zeitschrift für Physik* 63., no.7 (July 1, 1930), pp. 558–560.

[6] H. Hartmann, F. Ebert, and O. Bretschneider. "Elektrolysen in Phosphatschmelzen. I. Die elektrolytische Gewinnung von α- und β-Wolfram". *Zeitschrift für anorganische und allgemeine Chemie* 198., no.1 (May 28, 1931), pp. 116–140.

[7] George F. Hardy and John K. Hulm. "Superconducting Silicides and Germanides". *Physical Review* 89., no.4 (Feb. 15, 1953), pp. 884–884.

[8] B. T. Matthias et al. "Superconductivity of Nb_3Sn". *Physical Review* 95., no.6 (Sept. 15, 1954), pp. 1435–1435.

[9] B. T. Matthias. "Empirical Relation between Superconductivity and the Number of Valence Electrons per Atom". *Physical Review* 97., no.1 (Jan. 1, 1955), pp. 74–76.

[10] John K. Hulm, J. Eugene Kunzler, and Bernd T. Matthias. "The road to superconducting materials". *Physics Today* (Jan. 1981).

[11] H Rogalla and P. H Kes. *100 years of superconductivity.* Boca Raton: CRC Press/Taylor & Francis Group, 2012.

[12] J. K. Hulm and R. D. Blaugher. "Superconducting Solid Solution Alloys of the Transition Elements". *Physical Review* 123., no.5 (Sept. 1, 1961), pp. 1569–1580.

[13] Yinshun Wang. *Fundamental elements of applied superconductivity in electrical engineering.* Singapore: Science Press/John Wiley & Sons Inc, 2013.

[14] J. G. Bednorz and K. A. Muller. "Possible high T_c superconductivity in the Ba-La-Cu-O system". *Zeitschrift für Physik B Condensed Matter* 64., no.2 (June 1, 1986), pp. 189–193.

[15] M. K. Wu et al. "Superconductivity at 93 K in a new mixed-phase Y-Ba-Cu-O compound system at ambient pressure". *Physical Review Letters* 58., no.9 (Mar. 2, 1987), pp. 908–910.

[16] Hiroshi Maeda et al. "A New High-T_c Oxide Superconductor without a Rare Earth Element". *Japanese Journal of Applied Physics* 27., no.2 (Feb. 1988), p. L209.

[17] M. A. Subramanian et al. "A New High-Temperature Superconductor: $Bi_2Sr_{3-x}Ca_xCu_2O_{8+y}$". *Science* 239., no.4843 (Feb. 26, 1988), pp. 1015–1017.

[18] J. L. Tallon et al. "High-T_c superconducting phases in the series $Bi_{2.1}(Ca,Sr)_{n+1}Cu_nO_{2n+4+delta}$". *Nature* 333., no.6169 (May 1988), p. 153.

[19] Jian-Feng Ge et al. "Superconductivity above 100 K in single-layer FeSe films on doped $SrTiO_3$". *Nature Materials* 14., no.3 (Mar. 2015), p. 285.

[20] Jeremy Weiss. "Synthesis and characterization of superconducting ferropnictide bulks and wires". PhD thesis. The Florida State University, 2015. 148 pp.

[21] Maxime Matras. "Investigation of Ag-Sheathed Multi-Filamentary $Bi_2Sr_2CaCu_2O_{[8-X]}$ Superconducting Round Wires Processed with Overpressure, for High Field Magnets". PhD thesis. Florida State University, 2016.

[22] Peng Chen. "Processing and Characterization of Superconducting Solenoids Made of Bi-2212/Ag-Alloy Multifilament Round Wire for High Field Magnet Applications". PhD thesis. Florida State University, 2016.

[23] Xinbo Hu. "Studies on the origins and nature of critical current variations in rare earth barium copper oxide coated conductors". PhD thesis. Florida State University, 2017.

[24] Charles P. Poole, Horacio A. Farach, and Richard J. Creswick. *Superconductivity*. San Diego: Academic Press, 1995. 620 pp.

[25] Fritz London and Heinz London. "The electromagnetic equations of the supraconductor". *Proceedings of the Royal Society of London A: Mathematical, Physical and Engineering Sciences*. Vol. 149. The Royal Society, 1935, pp. 71–88.

[26] Arno Godeke. "Performance Boundaries in Nb_3Sn Superconductors". PhD thesis. University of Twente, 2005.

[27] E. J. Kramer. "Scaling laws for flux pinning in hard superconductors". *Journal of Applied Physics* 44., no.3 (Mar. 1, 1973), pp. 1360–1370.

[28] Lyndon R. Evans, ed. *The Large Hadron Collider: a marvel of technology*. 1. ed. Fundamental sciences. Lausanne: EPFL Press [u.a.], 2009. 251 pp.

[29] Q. Li, W. Si, and I. K. Dimitrov. "Films of iron chalcogenide superconductors". *Reports on Progress in Physics* 74., no.12 (2011), p. 124510.

[30] P.J. Lee. *The expanded ASC "Plots" page*. 2017. URL: http://fs.magnet.fsu.edu/~lee/plot/plot.htm.

[31] J. J. Hanak, K. Strater, and G. W. Cullen. "Preparation and Properties of Vapor-Deposited Niobium Stannide". *RCA (Radio Corporation of America) Review (U.S.)* Vol: 25 (Sept. 1, 1964).

[32] H Devantay et al. "The physical and structural properties of superconducting A15-type Nb-Sn alloys". *Journal of Material Science* 16 (Jan. 8, 1981), pp. 2145–2153.

[33] L. D. Cooley, Y. F. Hu, and A. R. Moodenbaugh. "Enhancement of the upper critical field of Nb_3Sn utilizing disorder introduced by ball milling the elements". *Applied Physics Letters* 88., no.14 (Apr. 3, 2006), p. 142506.

[34] G. Lefranc and A. Muller. "Effect of copper additions to superconducting niobium-tin sinter materia". *Journal of the Less Common Metals* 45., no.2 (Mar. 1, 1976), pp. 339–342.

[35] H. H. Farrell, G. H. Gilmer, and M. Suenaga. "Grain boundary diffusion and growth of intermetallic layers: Nb_3Sn". *Journal of Applied Physics* 45., no.9 (Sept. 1, 1974), pp. 4025–4035.

[36] H. H. Farrell, G. H. Gilmer, and M. Suenaga. "Diffusion mechanisms for the growth of Nb_3Sn intermetallic layers". *Thin Solid Films* 25., no.1 (Jan. 1975), pp. 253–264.

[37] "Deposition of crystalline niobium stannide". , no.US3268362 A. Joseph Hanak and Leslie Cooper John. Aug. 23, 1966.

[38] "Deposition of niobium stannide". , no.US3420707 A. Joseph John Hanak. Jan. 7, 1969.

[39] R. E. Enstrom et al. "Effect of Impurity Gas Additions on the Superconducting Critical Current of Vapor-Deposited Nb_3Sn". *Journal of The Electrochemical Society* 119., no.6 (June 1, 1972), pp. 743–747.

[40] C. T. Wu, R. T. Kampwirth, and J. W. Hafstrom. "High-rate magnetron sputtering of high T_c Nb_3Sn films". *Journal of Vacuum Science and Technology* 14., no.1 (Jan. 1, 1977), pp. 134–137.

[41] R. T. Kampwirth, C. T. Wu, and J. W. Hafstrom. "Nb_3Ge and Nb_3Sn Films Prepared by High-Rate Magnetron Sputtering". *Advances in Cryogenic Engineering.* Advances in Cryogenic Engineering (1978), pp. 465–472.

[42] B. Hillenbrand et al. "Superconducting Nb_3Sn cavities with high microwave qualities". *IEEE Transactions on Magnetics* 13., no.1 (Jan. 1977), pp. 491–495.

[43] M. Benz. "Superconducting properties of diffusion processed niobium-Tin tape". *IEEE Transactions on Magnetics* 2., no.4 (Dec. 1966), pp. 760–764.

[44] G. Otto, O. Y. Reece, and U. Roy. "Synthesis of Nb_3Sn by shock waves". *Applied Physics Letters* 18., no.10 (May 15, 1971), pp. 418–420.

[45] AR Kaufmann and JJ Pickett. "Multifilament Nb_3Sn superconducting wire". *Bulletin of the American Physical Society*. Vol. 15. Amer. Inst. Physics Circulation Fulfillment Div., 500 Sunnyside Blvd, Woodbury, NY 11797-2999, 1970, p. 838.

[46] "Method for producing $(Nb,Ti)_3Sn$ wire by use of Ti source rods". , no.US6981309 B2. S. Hong, J. Parrell, and M. Field. Jan. 3, 2006.

[47] D. B. Smathers et al. "Production of tin core modified jelly roll cable for the MIT Multipurpose Coil". *IEEE Transactions on Magnetics* 24., no.2 (Mar. 1988), pp. 1131–1133.

[48] D. Smathers et al. "Observations of the effect of pre-reaction on the properties of Nb_3Sn Bronze composites". *IEEE Transactions on Magnetics* 19., no.3 (May 1983), pp. 1417–1420.

[49] Christopher Segal et al. "Evaluation of critical current density and residual resistance ratio limits in powder in tube Nb_3Sn conductors". *Superconductor Science and Technology* 29., no.8 (2016), p. 085003.

[50] "powder-in-tube process and method of manufacture". , no.US20100031493 A1. Leszek Motowidlo. Feb. 11, 2010.

[51] D. Larbalestier et al. "Multifilamentary niobium tin solenoids". *IEEE Transactions on Magnetics* 11., no.2 (Mar. 1975), pp. 555–558.

[52] Y. Murakami et al. "Improvement in Characteristics of Bronze-processed Nb_3Sn Superconducting Wires". *TEION KOGAKU (Journal of Cryogenics and Superconductivity Society of Japan)* 47., no.8 (2012), pp. 474–478.

[53] X. Xu, M. D. Sumption, and E. W. Collings. "A model for phase evolution and volume expansion in tube type Nb_3Sn conductors". *Superconductor Science and Technology* 26., no.12 (Dec. 1, 2013), p. 125006.

[54] Charlie Sanabria. "A new understanding of the heat treatment of Nb_3Sn superconducting wires". PhD thesis. Florida State University, 2017.

[55] J.A. Parrell et al. "High field Nb_3Sn conductor development at Oxford Superconducting Technology". *IEEE Transactions on Applied Superconductivity* 13., no.2 (June 2003), pp. 3470–3473.

[56] C. van Beijnen and J. Elen. "Potential fabrication method of superconducting multifilament wires of the A-15 type". *IEEE Transactions on Magnetics* 11., no.2 (Mar. 1975), pp. 243–246.

[57] J. Elen, C. van Beijnen, and C. van der Klein. "Multifilament V_3Ga and Nb_3Sn superconductors produced by the ECN-technique". *IEEE Transactions on Magnetics* 13., no.1 (Jan. 1977), pp. 470–473.

[58] C. van Beijnen and J. Elen. "Multifilament Nb_3Sn superconductors produced by the E.C.N. technique". *IEEE Transactions on Magnetics* 15., no.1 (Jan. 1979), pp. 87–90.

[59] E.M. Hornsveld and J.D. Elen. "Development of Niobium-Tin Conductors at ECN". *Advances in Cryogenic Engineering* 36A (1990), pp. 157–160.

[60] J.L.H. Lindenhovius et al. "Progress in the development of Nb_3Sn conductors based on the "powder in tube" method with finer filaments". *IEEE Transactions on Applied Superconductivity* 9., no.2 (June 1999), pp. 1451–1454.

[61] C. M. Fischer. "Investigation of the Relationships Between Superconducting Properties and Nb_3Sn Reaction Conditions In Powder-In-Tube Nb_3Sn Conductors". PhD thesis. University of Wisconsin - Madison, 2002.

[62] C. M. Fischer, P. J. Lee, and D. C. Larbalestier. "Irreversibility field and critical current density as a function of heat treatment time and temperature for a pure niobium powder-in-tube Nb_3Sn conductor". *AIP Conference Proceedings*. Advances in Cryogenic Engineering: Proceedings of the International Cryogenic Materials Conference - ICMC. Vol. 614. AIP Publishing, May 15, 2002, pp. 1008–1015.

[63] A. Godeke et al. "The upper critical field of filamentary Nb_3Sn conductors". *Journal of Applied Physics* 97., no.9 (Apr. 27, 2005), p. 093909.

[64] B. ten Haken, A. Godeke, and H. H. J. ten Kate. "The strain dependence of the critical properties of Nb_3Sn conductors". *Journal of Applied Physics* 85., no.6 (Mar. 15, 1999), pp. 3247–3253.

[65] A. Godeke. "A review of the properties of Nb_3Sn and their variation with A15 composition, morphology and strain state". *Superconductor Science and Technology* 19., no.8 (Aug. 1, 2006), R68.

[66] A. Ballarino and L. Bottura. "Targets for R&D on Nb_3Sn Conductor for High Energy Physics". *IEEE Transactions on Applied Superconductivity* 25., no.3 (June 2015), pp. 1–6.

[67] J. A. Parrell et al. "Nb_3Sn Conductor Development for Fusion and Particle Accelerator Applications". *AIP Conference Proceedings* 711., no.1 (June 28, 2004), pp. 369–375.

[68] C. Tarantini et al. "Composition and connectivity variability of the A15 phase in PIT Nb_3Sn wires". *Superconductor Science and Technology* 28., no.9 (Sept. 1, 2015), p. 095001.

[69] C. Tarantini et al. "Examination of the trade-off between intrinsic and extrinsic properties in the optimization of a modern internal tin Nb_3Sn conductor". *Superconductor Science and Technology* 27., no.6 (June 1, 2014), p. 065013.

[70] C. Scheuerlein et al. "Phase transformations during the reaction heat treatment of Nb_3Sn superconductors". *Journal of Physics: Conference Series* 234., no.2 (June 1, 2010), p. 022032.

[71] "Semi-finished wire for a Nb_3Sn superconducting wire". , no.US20140096997 A1. K. Schlenga. Apr. 10, 2014.

[72] B. Bordini et al. “The Bundle-Barrier PIT Wire Developed for the HiLumi LHC Project”. *IEEE Transactions on Applied Superconductivity* 27., no.4 (June 2017), pp. 1–6.

[73] Peter J. Lee and David C. Larbalestier. “Microstructural factors important for the development of high critical current density Nb_3Sn strand”. *Cryogenics*. Special Issue: Low-Tc Superconducting Materials 48., no.7 (July 2008), pp. 283–292.

[74] L. Bottura et al. “Advanced Accelerator Magnets for Upgrading the LHC”. *IEEE Transactions on Applied Superconductivity* 22., no.3 (June 2012), pp. 4002008–4002008.

[75] M.B. Field et al. “Optimizing Conductors for High Field Applications”. *IEEE Transactions on Applied Superconductivity* 24., no.3 (June 2014), pp. 1–5.

[76] B. Bordini et al. “Impact of the Residual Resistivity Ratio on the Stability of Magnets”. *IEEE Transactions on Applied Superconductivity* 22., no.3 (June 2012), pp. 4705804–4705804.

[77] Joseph Goldstein, ed. *Scanning electron microscopy and x-ray microanalysis*. 3rd ed. New York: Kluwer Academic/Plenum Publishers, 2003. 689 pp.

[78] Washington Mills. *Particle Size Conversion Chart- ANSI - Washington Mills*. 2017. URL: http://www.washingtonmills.com/guides/grit-sizes-ansi/particle-size-conversion-chart-ansi/ (visited on 12/08/2017).

[79] C. A. Schneider, W. S. Rasband, and K. W. Eliceiri. “NIH Image to ImageJ: 25 years of Image Analysis”. *Nature methods* 9., no.7 (July 2012), pp. 671–675.

[80] ThermoFisher Scientific. *An Introduction to Electron Microscopy*. 2010.

[81] B. Hafner. “Scanning Electron Microscopy Primer”. Characterization Facility, University of Minnesota - Twin Cities, 2007.

[82] Johannes Schindelin et al. “Fiji: an open-source platform for biological-image analysis”. *Nature Methods* 9., no.7 (July 2012), pp. 676–682.

[83] Kenneth Moreland. “Diverging Color Maps for Scientific Visualization”. *Advances in Visual Computing*. International Symposium on Visual Computing. Lecture Notes in Computer Science. Springer, Berlin, Heidelberg, Nov. 30, 2009, pp. 92–103.

[84] John C. Russ. *The image processing handbook*. 6th ed. Boca Raton: CRC Press, 2011. 867 pp.

[85] John Hunter. *Choosing Colormaps — Matplotlib 2.0.2 documentation*. 2017. URL: https://matplotlib.org/users/colormaps.html (visited on 03/14/2018).

[86] M. Borkin et al. “Evaluation of Artery Visualizations for Heart Disease Diagnosis”. *IEEE Transactions on Visualization and Computer Graphics* 17., no.12 (Dec. 2011), pp. 2479–2488.

[87] Nathaniel Smith and Stefan van der Walt. *A Better Default Colormap for Matplotlib — SciPy 2015 — Nathaniel Smith and Stefan van der Walt*. 2015.

[88] J. Ekin. "Strain dependence of the critical current and critical field in multifilamentary Nb_3Sn composites". *IEEE Transactions on Magnetics* 15., no.1 (Jan. 1979), pp. 197–200.

[89] W. L. Neijmeijer and B. H. Kolster. "Ternary System Nb-Sn-Cu at 675 degree C." *ResearchGate* 78., no.10 (Oct. 1, 1987), pp. 730–737.

[90] "Semifinished wire with PIT elements for a superconducting wire containing Nb_3Sn and method of producing the semifinished wire". , no.US20160247606 A1. M. Thoener and B. Sailer. Aug. 25, 2016.

[91] J. Elen et al. "Development of stabilized Nb_3Sn wire containing a reduced number of filaments". *IEEE Transactions on Magnetics* 17., no.1 (Jan. 1981), pp. 1002–1005.

[92] L. R. Motowidlo and G. M. Ozeryansky. "A new PIT Nb_3Sn conductor for high magnetic field applications". *IEEE Transactions on Applied Superconductivity* 18., no.2 (June 2008), pp. 1001–1004.

[93] L. R. Motowidlo and G. M. Ozeryansky. "A Nb_3Sn conductor via Cu_5Sn_4 PIT process for high field applications". *AIP Conference Proceedings* 986., no.1 (Mar. 3, 2008), pp. 269–276.

[94] W.L. Neijmeijer and B.H. Kolster. "Characteristics of a production route for filamentary Nb_3Sn superconductors based on a reaction between niobium and Nb_6Sn_5". *Journal of the Less Common Metals* 160., no.1 (Apr. 1990), pp. 161–170.

[95] S. Fürtauer et al. "The Cu–Sn phase diagram, Part I: New experimental results". *Intermetallics* 34 (Mar. 2013), pp. 142–147.

[96] J. P. Charlesworth, I. Macphail, and P. E. Madsen. "Experimental work on the niobium-tin constitution diagram and related studies". *Journal of Materials Science* 5., no.7 (July 1970), pp. 580–603.

[97] M.T. Naus, P.J. Lee, and D.C. Larbalestier. "The influence of the starting Cu-Sn phase on the superconducting properties of subsequently reacted internal-Sn Nb_3Sn conductors". *IEEE Transactions on Applied Superconductivity* 11., no.1 (Mar. 2001), pp. 3569–3572.

[98] I. Pong, L. Oberli, and L. Bottura. "Cu diffusion in Nb_3Sn internal tin superconductors during heat treatment". *Superconductor Science and Technology* 26., no.10 (Oct. 1, 2013), p. 105002.

[99] S. Martin et al. "The crystal structure of $(Nb_{0.75}Cu_{0.25})Sn_2$ in the Cu-Nb-Sn system". *Intermetallics* 80 (Jan. 2017), pp. 16–21.

[100] C. Scheuerlein et al. "Coarse Grain Formation and Phase Evolution During the Reaction of a High Sn Content Internal Tin Strand". *IEEE Transactions on Applied Superconductivity* 21., no.3 (2011), pp. 2554–2558.

[101] H. Veringa, P. Hoogendam, and A. Wees. "Growth kinetics and characterization of superconducting properties of multifilament materials made by the ECN powder method". *IEEE Transactions on Magnetics* 19., no.3 (May 1983), pp. 773–776.

[102] C. D. Hawes. "Investigations of the Inhomogeneity of a Powder-In-Tube Nb_3Sn Conductor". PhD thesis. University of Wisconsin - Madison, 2000.

[103] R. M. Scanlan, W. A. Fietz, and E. F. Koch. "Flux pinning centers in superconducting Nb_3Sn". *Journal of Applied Physics* 46., no.5 (May 1, 1975), pp. 2244–2249.

[104] Christopher Segal et al. "Improvement of small to large grain A15 ratio in Nb_3Sn PIT wires by inverted multistage heat treatments". *IOP Conference Series: Materials Science and Engineering* 279.1 (2017), p. 012019.

[105] D.S. Easton and D.M. Kroeger. "Kirkendall voids–A detriment to Nb_3Sn superconductors". *IEEE Transactions on Magnetics* 15., no.1 (Jan. 1979), pp. 178–181.

[106] L. Oberli. "Development of the Rutherford Cable for the EuCARD High Field Dipole Magnet FRESCA2". *IEEE Transactions on Applied Superconductivity* 23., no.3 (June 2013), pp. 4800704–4800704.

[107] B. Bordini et al. "Extensive Characterization of the 1 mm PIT Strand for the 13 T FRESCA2 Magnet". *IEEE Transactions on Applied Superconductivity* 22., no.3 (June 2012), pp. 6000304–6000304.

[108] M. C. Jewell. "The effect of strand architecture on the fracture propensity of Nb_3Sn composite wires". PhD thesis. University of Wisconsin - Madison, 2008.

[109] Carlos Sanabria et al. "Metallographic autopsies of full-scale ITER prototype cable-in-conduit conductors after full cyclic testing in SULTAN: II. Significant reduction of strand movement and strand damage in short twist pitch CICCs". *Superconductor Science and Technology* 28., no.12 (2015), p. 125003.

[110] P. J. Lee and D. C. Larbalestier. "Compositional and microstructural profiles across Nb_3Sn filaments produced by different fabrication methods". *IEEE Transactions on Applied Superconductivity* 11.1 (Mar. 2001), pp. 3671–3674.

[111] X. Xu et al. "The effects of Ti addition and high Cu/Sn ratio on tube type $(Nb,Ta)_3Sn$ strands, and a new type of strand designed to reduce unreacted Nb ratio". *IEEE Transactions on Applied Superconductivity* 24., no.3 (June 2014), pp. 1–4.

[112] Xingchen Xu. "Prospects for Improving the Critical Current Density of Superconducting Nb_3Sn Strands via Optimization of Nb_3Sn Fraction, Stoichiometry, and Grain Size". PhD thesis. Ohio State University, 2016.

[113] T. Baumgartner et al. "Performance Boost in industrial multifilamentary Nb_3Sn wires due to radiation induced pinning centers". *Scientific Reports* 5 (June 1, 2015), p. 10236.

[114] L. R. Motowidlo et al. “An intermetallic powder-in-tube approach to increased flux-pinning in Nb_3Sn by internal oxidation of Zr”. *Superconductor Science and Technology* 31., no.1 (2018), p. 014002.

[115] X. Xu, M. D. Sumption, and X. Peng. “Internally Oxidized Nb_3Sn Strands with Fine Grain Size and High Critical Current Density”. *Advanced Materials* 27., no.8 (Feb. 1, 2015), pp. 1346–1350.

BIOGRAPHICAL SKETCH

Christopher B. Segal was born and raised in south Florida. He received his BS degree in Physics and Applied and Computational Mathematics from Florida State University in 2010. He received his Ph.D. in 2018 in Mechanical Engineering from Florida State University. Christopher Segal's Ph.D. studies were conducted at the Applied Superconductivity Center at the National High Magnetic Field Laboratory, focusing on characterization of superconducting Nb_3Sn wires for future particle accelerators. His current research interests include superconducting magnet technology and material characterization by advanced imaging and analysis techniques.